

DIGITAL ACCESS TO SCHOLARSHIP AT HARVARD
DASH.HARVARD.EDU

HARVARD LIBRARY


Structural imaging and electro-optical control of two-dimensional semiconductors

Citation

Sushko, Andrey. 2022. Structural imaging and electro-optical control of two-dimensional semiconductors. Doctoral dissertation, Harvard University Graduate School of Arts and Sciences.

Link

https://nrs.harvard.edu/URN-3:HUL.INSTREPOS:37373731

Terms of use

This article was downloaded from Harvard University's DASH repository, and is made available under the terms and conditions applicable to Other Posted Material (LAA), as set forth at
https://harvardwiki.atlassian.net/wiki/external/NGY5NDE4ZjgzNTc5NDQzMGIzZWZhMGFlOWI2M2EwYTg

Accessibility

https://accessibility.huit.harvard.edu/digital-accessibility-policy

Share Your Story

The Harvard community has made this article openly available.
Please share how this access benefits you. Submit a story

HARVARD UNIVERSITY
Graduate School of Arts and Sciences



DISSERTATION ACCEPTANCE CERTIFICATE

The undersigned, appointed by the

Department of Physics

have examined a dissertation entitled

Structural imaging and electro-optical control of two-dimensional semiconductors

presented by Andrey Sushko

candidate for the degree of Doctor of Philosophy and hereby certify that it is worthy of acceptance.

Signature _____

Typed name: Professor Mikhail Lukin, Chair

Signature _____

Typed name: Professor Philip Kim

Signature _____

Typed name: Professor Norman Yao

Date: September 7, 2022

Structural imaging and electro-optical control of two-dimensional semiconductors

a dissertation presented
by
Andrey Sushko
to
The Department of Physics

in partial fulfillment of the requirements
for the degree of
Doctor of Philosophy
in the subject of
Physics

Harvard University
Cambridge, Massachusetts
September 2022

©2022 – Andrey Sushko
all rights reserved.

Thesis advisor: Professor Mikhail D. Lukin Andrey Sushko

Structural imaging and electro-optical control of two-dimensional semiconductors

Abstract

Monolayer transition metal dichalcogenides (TMDs) have attracted great interest due to their unique optical and electronic properties. As gapped, semiconducting counterparts to graphene, they display particularly strong light-matter interactions through tightly bound electron-hole pairs (excitons). Atomically-thick layers of distinct materials can further be combined into layered van der Waals (vdW) heterostructures to engineer materials with far more diverse properties than their constituent parts. Beyond just their composition, the relative alignment and resulting atomic stacking order of the layers in a vdW heterostructure can give rise to exotic effects that are entirely absent at different lattice orientations. For instance, periodic variation of local atomic registry due to a small angle or lattice-constant mismatch, known as a moiré pattern, has given rise to superconductivity in twisted bilayer graphene and exotic exciton states in TMD heterobilayers.

In this dissertation, I explore monolayer and bilayer TMD structures with properties that show promise for the realization of controlled quantum devices. We identity and examine an optically induced current perpendicular to the plane of a TMD monolayer

encapsulated in hexagonal boron nitride (hBN). Contrasted with the conventional picture of hBN as an insulating dielectric, these results point to both limitations and opportunities for the control of charge in TMD devices. Next, I present a new scanning electron microscopy (SEM) technique that makes it possible to nondestructively image the local stacking order in complete vdW devices, and apply it to correlate the local moiré periodicity with optical properties. These results provide important new tools and insights for the study of moiré heterostructures and the engineering of controllable quantum systems in TMDs.

Contents

Title . . . i
Copyright . . . ii
Abstract . . . iii
Table of Contents . . . v
Dedication . . . vii
Acknowledgments . . . viii
Citations to previously published work . . . xii

0 Introduction 1
0.1 Background . . . 1
0.2 Overview of this thesis . . . 3

1 Exploring gate-defined quantum confinement in TMDs 5
1.1 Introduction . . . 5
1.2 Electrostatic confinement . . . 8
1.3 Challenges towards QD realization . . . 12

2 Photocurrent in hBN heterostructures 17
2.1 Introduction . . . 18
2.2 Photocurrents in encapsulated TMDs . . . 20
2.3 Physics of photocurrents . . . 27
2.4 Photocurrent and upconversion . . . 34
2.5 Contactless hole injection and gate-dragging effects . . . 38
2.6 Conclusion . . . 41

3 SEM Imaging 2D heterostructures 42
3.1 Introduction . . . 42
3.2 SEM Imaging basics . . . 44
3.3 Channeling Modulated Secondary Electron Imaging . . . 47
3.4 Imaging encapsulated structures . . . 54
3.5 Computational model of SEM signal . . . 57
3.6 Alternate imaging modes and applications . . . 60
3.7 Correlating imaged moiré patterns with optical measurements . . . 70
3.8 Properties of the reconstructed superlattice . . . 75
3.9 Conclusion . . . 79

4 Conclusion 82

Appendix A Supporting Material for Chapter 1 84
A.1 Experimental Methods . . . 84

Appendix B Supporting Material for Chapter 2 **86**
B.1 Experimental Methods 86
B.2 Device structures 87
B.3 DFT Methods 88
B.4 Kinetic Model and Doping-dependent QE fits 90
B.5 Dissociation Doping Power Dependence 95
B.6 Photocurrent spatial uniformity 98
B.7 Resonant excitation efficiency comparison 99
B.8 $MoSe_2$ contact verification 100

Appendix C Supporting Material for Chapter 3 **104**
C.1 Signal corrections and hBN background subtraction 104
C.2 Computation modelling of SEM signal 105
C.3 Comparison of PL and absorption spectroscopy 109
C.4 Lateral exciton motion model 109
C.5 Experimental Methods 111

References **122**

To my parents and Andreea

Acknowledgments

The work in this dissertation was only possible thanks to an exceptional group of people. Giving proper thanks to everyone would be challenging enough considering that the size of the Lukin lab is conventionally estimated to lie somewhere between "large" and "uncountable", but is vastly harder still in light of the vibrant and delocalized 2D materials community at Harvard, spanning multiple groups with a level of collaboration that would be impressive within a single lab.

I am deeply grateful to Prof. Misha Lukin for his consistent support and remarkable research insights on essentially any topic. When I started working in the group on gate defined quantum dots, I don't think either of us expected to end up publishing a manuscript on SEM imaging a few years down the line. Nevertheless, Misha's insight and enthusiasm to pursue interesting questions greatly improved the breadth and significance of that effort. Prior to joining the group, I recall Misha saying that he likes to work with students as colleagues with the independence to pursue their own interests. The direct benefits of that approach are obvious, but it's only in retrospect that I see the extent to which this freedom created an environment in which one also learns to measure and weigh their own interests. Thanks to the environment Misha cultivated, I find myself now in a position of not only having had academic freedom but having learned much better how to make use of it. I am also very thankful to Prof. Philip Kim for all of his input into my work over the years and for his consistently positive attitude no matter how well or poorly that work was progressing, and to Prof. Eugene Demler for helping

us work through some of our most confounding observations. Though his presence on my committee is very recent, I must also extend my immense gratitude to Prof. Norman Yao for going to great lengths on incredibly short notice to support me in finishing my PhD.

From the start of my PhD, I was fortunate enough to work closely with Kristiaan De Greve, and did so through the majority of the projects in this dissertation. I can't thank him enough for being an exceptional mentor, colleague, and friend over that time, and throughout the rest of my PhD. Aside from being a near inexhaustible font of knowledge on matters of physics and near everything else, his judgement on how to navigate everything from fabrication to publication has been invaluable. A huge thanks also to Ke Wang and Luis Jauregui for teaching me much about 2D materials fabrication and measurement during my first years at Harvard.

Though there are far more people than I can reasonably mention, I can't help but do my best to acknowledge the many remarkable experimentalists, past and present, with whom I have had the pleasure to collaborate on anything from one-off measurements and device fabrication steps to entire research projects. These include Trond Andresen, Giovanni Scuri, Andy Joe, Eric Peterson, Sasha Zibrov, Xiaoling Liu, Hyobin Yoo, Kateryna Pistunova, You Zhou, Ryan Gelly, Jiho Sung, Andrés Mier Valdivia, Javier Sanchez-Yamagishi, and Bo Dwyer. I have been lucky to collaborate with many outstanding theorists, both at Harvard and around the world, and can't thank them enough for all of the insight they have brought to the table while looking over oftentimes deeply confusing

observations. I'd especially like to call out the help of Dominik Wild, Falko Pientka, Richard Schmidt, Madeleine Phillips, Sasha Efros, and C. Steve Hellberg. A special thanks also to Prof. Bernhard Urbaszek for taking an interest in and helping greatly with the interpretation of the work in Chapter 2 of this dissertation.

Throughout this work, I was supported by two excellent fellowships in the Fannie and John Hertz Foundation Fellowship and the PD Soros Fellowship of new Americans. I am honored to have been selected and very grateful for all their support. A special mention must be reserved for the Hertz fellowship community which, between official events and informal gatherings has been one of the many highlights of my time at Harvard. I'm also grateful to Iris Cong, Hengyun Zhou, and many others for being exceptional co-TFs and assistants for Misha's AMO class

Huge thanks also goes out to the Harvard Physics department and the countless people who make it all run, including Jacob Barandes, Lisa Cacciabaudo, Samantha Dakoulas, Clare Ploucha, Silke Exner, and countless others. Also, to Stan Cotreau for running the machine shop, everyone at Harvard CNS for making it possible to fabricate every single device reported on in this work, and Jim MacArthur for helping us with some very specific and challenging electronics and being an invaluable resource throughout.

Finally, I am eternally grateful to my parents for instilling in me from a very young age the idea that every aspect of the world is understandable if you ask the right questions, and for supporting me throughout this journey. Most importantly, I want to thank Andreea for being my partner and closest friend, and for her exceptional ability to

make the most of highly varied times - her personality makes every day better and her character makes me better every day. This thesis is dedicated to her.

Citations to previously published work

Parts of this dissertation cover research reported in the following articles:

Chapter 1 contains material published as:

Wang, K., De Greve, K., Jauregui, L.A., Sushko, A., High, A., Zhou, Y., Scuri, G., Taniguchi, T., Watanabe, K., Lukin, M.D. and Park, H., 2018. Electrical control of charged carriers and excitons in atomically thin materials. Nature nanotechnology, 13(2), pp.128-132.

Chapter 2 and appendix B contain material published as

Sushko, A., De Greve, K., Phillips, M., Urbaszek, B., Joe, A.Y., Watanabe, K., Taniguchi, T., Efros, A.L., Hellberg, C.S., Park, H. and Kim, P., 2021. Asymmetric photoelectric effect: Auger-assisted hot hole photocurrents in transition metal dichalcogenides. Nanophotonics, 10(1), pp.105-113.

Chapter 3 and Appendix C contain material published as

Andersen, T.I.*, Scuri, G.*, Sushko, A.*, De Greve, K.*, Sung, J., Zhou, Y., Wild, D.S., Gelly, R.J., Heo, H., Bérubé, D. and Joe, A.Y., 2021. Excitons in a reconstructed moiré potential in twisted WSe2/WSe2 homobilayers. Nature Materials, 20(4), pp.480-487.

0

Introduction

0.1 Background

The field of two-dimensional materials has grown rapidly since its inception with the discovery of graphene in 2004[60]. Structurally, these materials are distinguished by covalent in-plane bonds and weak van der Waals coupling between layers, which allows monolayers to be exfoliated from a bulk crystal, or grown on a suitable substrate, while remaining chemically stable. Aside from this structural commonality, however, a wide range of 2D materials have been discovered, with a rich variety of unique mechanical,

electronic, optical, and magnetic properties. Furthermore, these properties are highly tunable, as a direct consequence of the two dimensional nature of these materials presenting a surface without an underlying 'bulk'. As such, any modification of the surface environment constitutes a change to the properties of the entire material. The versatility of 2D materials is further enhanced by the ability to assemble layers of different materials into a 'stacked' heterostructure. Since the interaction between adjacent layers modifies the band structure of each, devices can be constructed to exhibit properties entirely absent from their constituent parts. A notable example of this discovered recently is the emergence of superconductivity in graphene when two or more layers are stacked with a very specific small misalignment between the lattice vectors of the layers[8,9,63]. This dissertation will focus on a particular class of 2D materials known as transition metal dichalcogenides (TMDs). TMDs consist of a hexagonal lattice in which half of the sites are occupied but a transition metal, such as molybdenum or tungsten, and the other half by a pair of chalcogen atoms like sulphur or selenium. Many of the TMD monolayers are direct bandgap semiconductors which host tightly bound electron-hole pairs (excitons) when illuminated at or above the exiton energy. The high efficiency of optical excitation and emission along with the strong binding of TMD excitons makes these materials an exciting platform for crafting controlled light-matter interactions, as we will explore in the following chapters.

0.2 Overview of this thesis

This work covers a range of experiments on TMD heterostructures, with the broad aim of exploring these materials as a platform for the implementation of quantum technologies. In Chapter 1, I report on efforts to realize an electrostatically-defined quantum dot device in monolayer $MoSe_2$. We show signatures of charge localization but do not reach the point of implementing a controlled qubit. Effects that complicate the creation of a controlled dot are discussed. Chapter 2 covers one such effect that was discovered during the pursuit of a quantum dot device. Specifically, we identify a mechanism by which holes from a TMD monolayer can be injected into the hexagonal boron nitride (hBN) encapsulation layer through optical excitation. Given the standard use of hBN is as a clean encapsulation layer for 2D devices and as a dielectric layer for electrostatic gating, we find the injection of charge into a layer of hBN placed between a TMD and gate to give rise to a sustained photocurrent. The out-of-plane current is a striking deviation from the conventional model of encapsulated 2D devices and, as such, presents both challenges and opportunities for charge control in these materials. We establish the consistency of this effect across many devices and multiple TMD materials, determine it to have a linear power dependence consistent with a single-exciton mediated process, and develop a model for the underlying mechanism through band structure and kinetic analysis. In Chapter 3, I present the discovery of a novel scanning electron microscopy imaging technique with the ability to resolve structural properties of 2 dimensional

materials. We find that through manipulation of the sample orientation relative to a focused primary electron beam, the emission of low energy secondary electrons is modulated in a manner that yields information on the lattice properties of the material. Crucially, the generation of secondary electrons is sufficiently efficient that the stacking order can be resolved even for bilayers of low atomic number, such as graphene. The higher yield from heavier elements, meanwhile, makes it possible to identify the stacking order of TMDs through tens of nanometers of hBN encapsulation. As such, we find the technique to be compatible with fully functional contacted and gated devices, allowing for direct correlation of structural properties with optical response. We leverage this capability to explore a twisted bilayer device and find it to host distinct species of excitons the ratios of which are modulated by the periodicity of structural domains in the bilayer.

1

Exploring gate-defined quantum confinement in TMDs

1.1 Introduction

Gate defined quantum dots are a promising platform for the development of controlled quantum electronic devices due to their high tunability and potential for scaling using standard semiconductor lithography processes. In such systems, a dot is

defined by tuning the potential of a set of local and global gate electrodes relative to that of a 2D electron gas in order to accumulate charge in a given region or deplete charge surrounding a given region, giving rise to an isolated quantum well with electrostatically tunable dimensions, depth, and occupation. Adjacent dots can be controllably coupled together by varying the electrostatic potential barrier between them to adjust the tunnel coupling strength, though only for physically adjacent quantum wells. The limitation of nearest-neighbour interactions poses significant challenges to the implementation and scaling of gate defined dots. While ostensibly zero-dimensional, the requirement to route out control electrodes for each dot means that each dot is defined by a 1 dimensional system, and thus standard 2D manufacturing techniques only allow for the realisation of 1 dimensional chain or ring structures, limiting the possible interconnectivity. Further limitations are noted with initialization and readout times on the order of milliseconds[78], though alternative techniques exist to accelerate initialization and readout into the microsecond range[5] thereby improving achievable fidelity.

Optically active defect-defined dots, in contrast, permit rapid control and effective coupling but suffer from significant challenges from nondeterministic physical placement and inconsistent optical properties that require complex magnetic tuning for each individual dot in order to align the relevant energy levels for a coupled multi-dot system[22]. A key component of strained-growth quantum dots is type-1 band alignment (Fig. 1.1a), in which both electrons and holes are confined in the dot region. Gate defined, dots, meanwhile, intrinsically only create unipolar confinement. This means

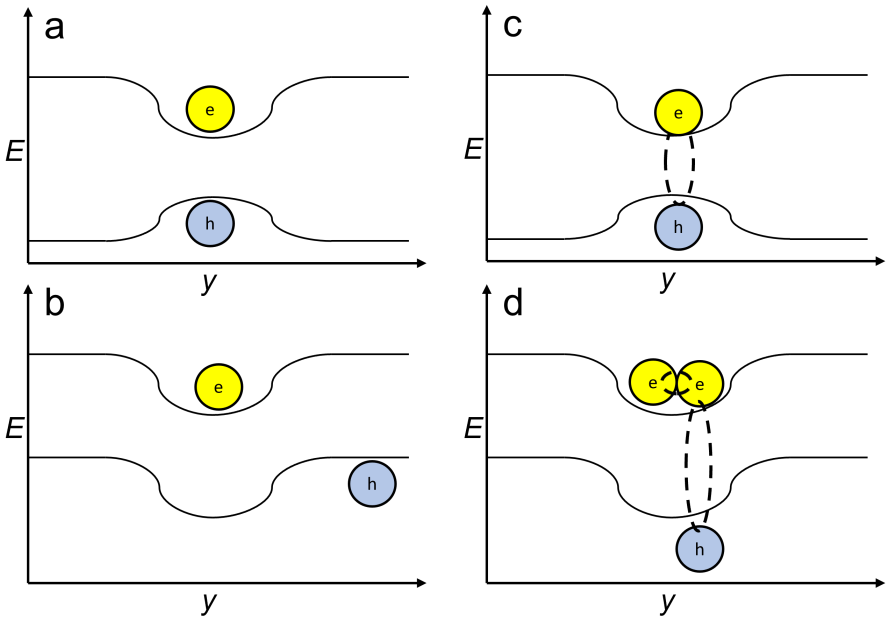


Figure 1.1: Band structure of quantum dots. **a**) Type-1 band structure that is achieved in strain-growth quantum dots confines both polarities of carrier in contrast to unipolar gate-defined dots (**b**) in which one polarity is anti-trapped. **c**) neutral excitons can be readily trapped in a type-1 band structure but dissociate in a gate defined dot if the binding energy is weaker than the trap potential. Disregarding field-gradient effects, a tightly bound neutral exciton is not confined in a gate-defined dot, however a charged exciton (trion) is trapped (**d**)

that while excitons readily remain bound in a type-1 dot potential, a neutral exciton in a gate-defined dot is not intrinsically trapped. To make matters worse, if the dot potential is deeper than the exciton binding energy, the charges will dissociate preventing recombination and thus optical out-coupling from the dot (Fig. 1.1b).

Transition metal dichalcogenide (TMD) 2D materials exhibit high excitonic binding energies, in the range of a few hundred meV, making it feasible to achieve electrostatic confinement of excitons without dissociation. Thus the overarching promise of gate-

defined quantum dots with TMD materials is to combine deterministic lithographically defined placement and comparatively easy electrostatic control with optical access to permit manipulation at a timescale much faster than the coherence time of the system. Although no quantum control over a TMD quantum dot is demonstrated in this effort, we validate several key components while also uncovering phenomena that present both challenges and opportunities for future work.

1.2 Electrostatic confinement

A series of devices were manufactured to study the feasibility of electrostatic trion confinement. The structure of one such device is shown in Fig. 1.2. A series of parallel local gates are deposited with channels of thickness from 50 nm to 150 nm between them. Each channel was designed with a a set of small cutouts to define the dot regions. In the intended operating mode, as the potential of the local gates is tuned in tandem from accumulation to depletion of carriers, the 2D electron gas becomes first confined to nanowires defined by the gaps between adjacent gates, and ultimately, once the fringe field of the electrodes depletes the nanowire region, to the isolated quantum dots defined along the wire.

We observe this constriction of carriers through the channel in transport measurements outlined in Fig. 1.3. For a range of global back-gate voltages, there exists a threshold local gate voltage V_g below which conduction through the channel is pinched off, while

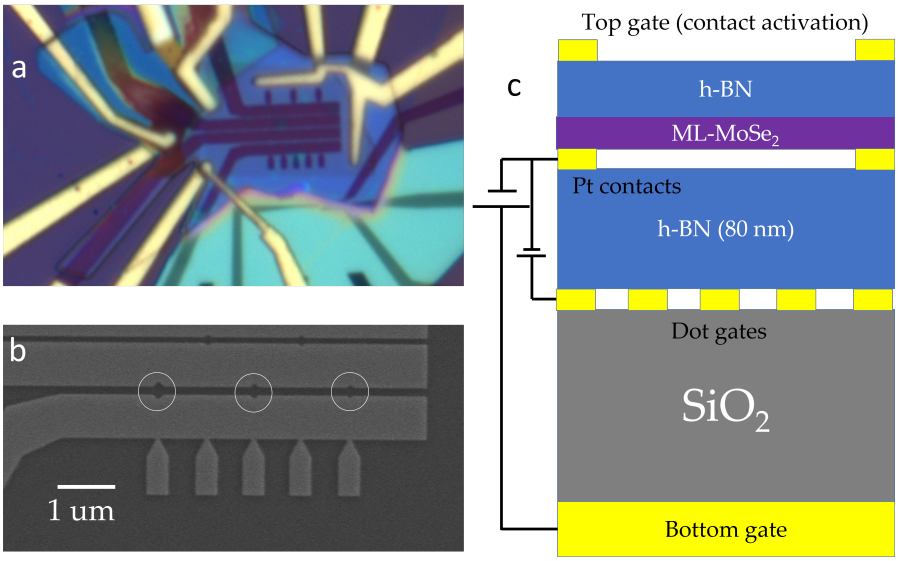


Figure 1.2: QD device structure. a) Optical microscope image of the device structure, showing 4 local gate electrodes underneath the stacked 2D heterostructure and contact electrodes around the perimeter, as laid out in the cross-section schematic (**c**). **b**) SEM image of the underlying gates showing varying width channels between the electrodes, with notches to define the quantum dot regions.

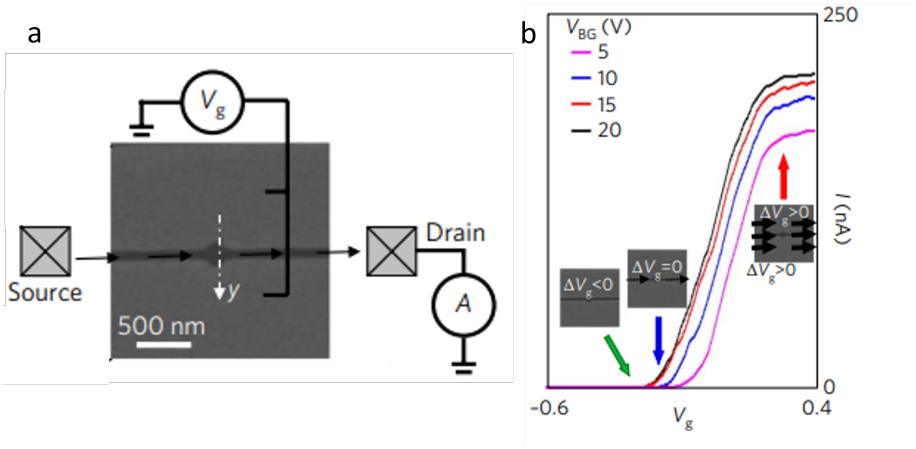


Figure 1.3: Transport characterization. a) SEM image of the dot and channel region between two gates the voltage of which (V_g) is tuned in tandem relative to the global bottom gate (V_{BG}). We define $\Delta V_g = 0$ as the potential near pinch-off at which conduction occurs only through the channel. For $\Delta V_g > 0.5$ we enter an accumulation regime where charge can freely flow across the entire gated area, while tuning to $\Delta V_g < 0.2$ leads to total depletion of carriers and thereby cuts off current.

for increasing V_g conduction rises and eventually plateaus in the regime where the local gates accumulate charge and allow for conduction across the entire width of the gated region.

Optical characterisation of the $MoSe_2$ was performed using photoluminescence measurements with off-resonant 660 nm excitation. PL spectra taken above a local gate electrode while tuned to charge neutrality show almost total suppression of the trion peak and an exciton peak full width half maximum of 0.7nm indicating primarily radiative broadening (Fig. 1.4a). PL spectra from an ungated region of the device, meanwhile, exhibit similar linewidths but appreciably higher charged exciton luminescence, suggesting the presence of some residual charge in the substrate that is screened by the local gate

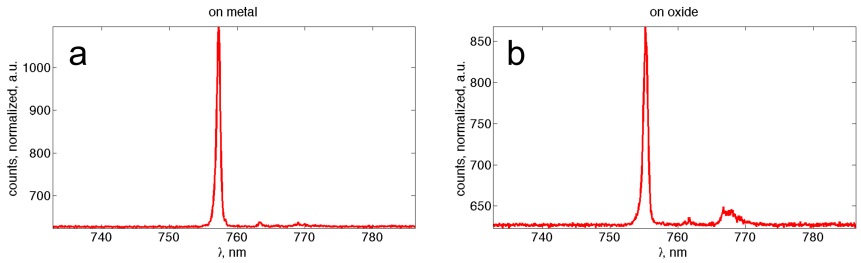


Figure 1.4: Photoluminescence characterization. PL spectra taken at 660 nm excitation for a region of $MoSe_2$ directly over a metal local local gate (**a**) and off gate over the SiO_2 substrate (**b**) taken in the charge-neutral regime. The sharp exciton peak in both cases points to good material quality with primarily radiatively limited linewidth. A broad, multi-peak trion signature in **b** suggests incomplete depletion of charge in the $MoSe_2$ stacked directly above the oxide substrate, potentially due to charge defects or trapped charges at the interface between the oxide and heterostructure.

electrodes (Fig. 1.4b).

Trion spatial distribution is mapped via PL filtered to the trion peak. Configuring the global back gate to accumulate electrons while depleting with the local gates results in the distribution shown in figure 1.5. Notably, while the 100 nm and 150 nm nanowires exhibit trion PL along their full length, the emission in the upper 50 nm nanowire is restricted to the lithographically defined dot regions, and depleted elsewhere by the fringing fields of the local electrodes.

Looking closer at....

To probe for signatures of confinement, we consider the emission spectra from the dot region as a function of local gate voltage (Fig. 1.7). When the region around the dot is is depleted of carriers we note the emergence of a sharp peak. Lifetime measurements for PL filtered around said peak are shown as a function of local gate voltage. When tuning

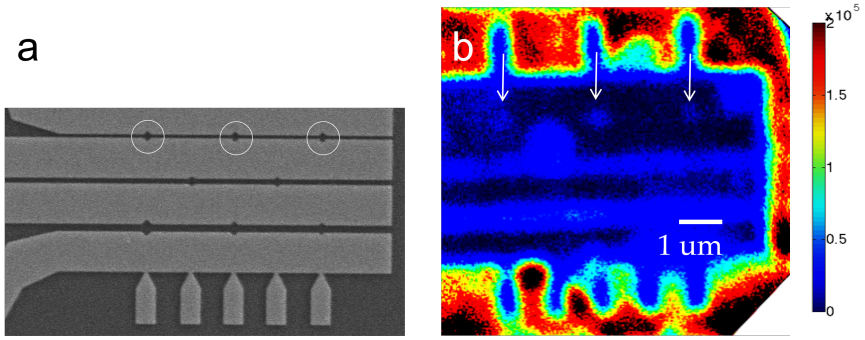


Figure 1.5: PL mapping trion localization. **a**) SEM image highlighting 3 lithographically defined quantum wells in the gap between two local gates. **b**) Photoluminescence map of the device filtered for only the trion emission peak, with local gated tuned to the confinement regime. Note that while the wider channels show emission along their full length, the narrowest top channel appears fully depleted of charge, with emission occurring only from the patterned dot regions.

from hole accumulation at negative gate voltage towards neutrality, the observed lifetime increases. This behaviour is consistent with consistent with increasing confinement as the excitonic momentum distribution broadens with increasing spatial localization, reducing the overlap with the light cone and thereby increasing lifetime as

$$\tau \propto \frac{1}{a^2}$$

for excitonic coherence length a[4].

1.3 Challenges towards QD realization

While the above experiments demonstrate charged exciton localization through electrostatic control, we must distinguish between the goal of electrostatically defined quantum

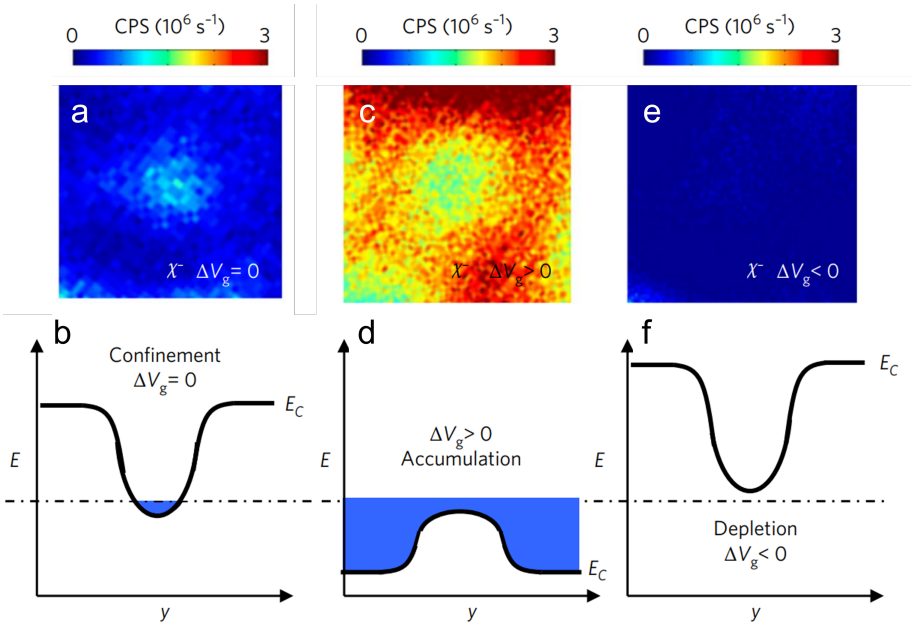


Figure 1.6: Gate-confined trions. Photoluminescence imagining filtered for trion emission in the vicinity of one of the dot regions shown in Fig. 1.5. In the confinement region, emission is concentrated in the dot area (**a**) as charge from the surrounding region is depleted by the local gates (**b**). Turning into the accumulation regime (**d**) leads to emission from the entire gated region (**c**), while depleting all carriers (**f**) corresponds to a lack of trion PL (**e**).

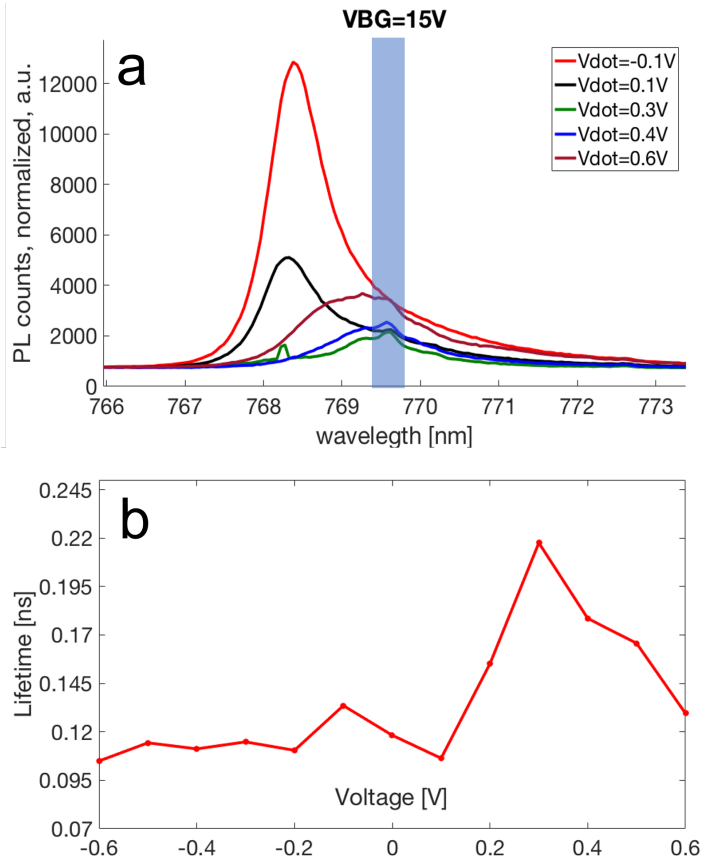


Figure 1.7: Trion confinement and lifetime. **a**) PL spectra from the quantum dot region as a function of local gate potential shows the emergence of a sharp peak in the trion spectrum when tuned to the confinement regime. **b**) filtering the PL emission over the range highlighted in blue in **a** shows the lifetime of the feature peaks in confinement, consistent with tighter spatial localization

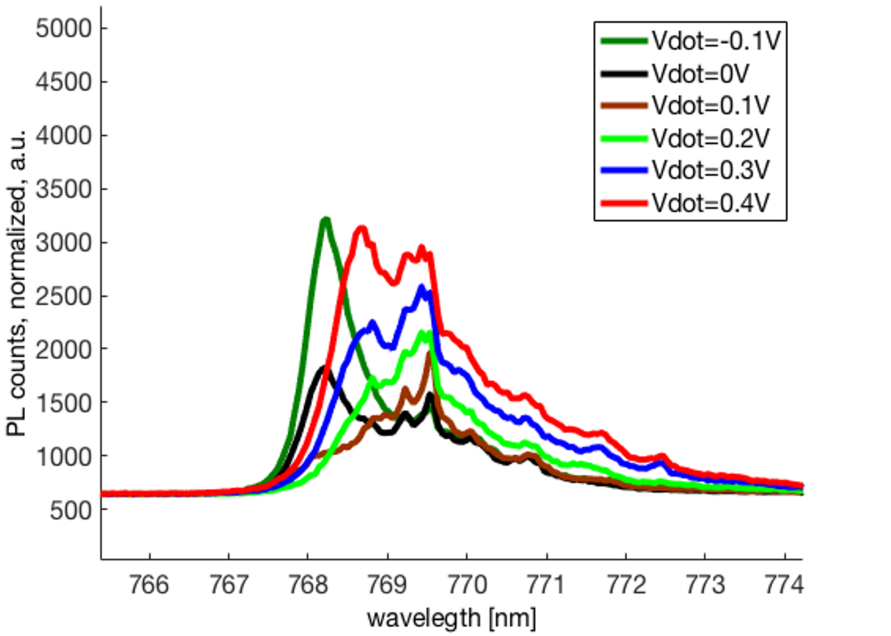


Figure 1.8: Dirty trion spectra in confinement. PL spectra from a different dot region on the device showing a large number of sharp emission features, potentially attributable to a range of charge defects or strain in the monolayer.

dots and the possibility of electrostatically activated dots. This concern is evident in a set of spectra taken from a dot on the same device and shown in Fig. 1.8. When tuning towards depletion of free carriers, a large number of peaks are visible in the trion emission with no readily explainable structure.

It is expected from Fig. 1.4b that the oxide substrate contains some residual charges, which would not be screened by local gates in the vicinity of the dot region. When free carriers are depleted, such trapped charges may present as confinement but without

the potential for meaningful electrostatic control of dot occupation. Defects introduced during the stacking and lithography process can also serve as local charge traps that are filled or depleted at some indeterminate local gate field. Furthermore, strain introduced by the thickness of the local gate electrodes has been established as a method of modifying the TMD band structure and generating localized quantum emitters[62]. This combination of factors makes it challenging to claim that gating plays a direct role in the generation of confined trions. Instead, it may simply display defect- and strain-driven confined states through the depletion of most free carriers.

Another major challenge to effective utilisation of electrostatically defined dots is doping control. In the above monolayer $MoSe_2$ device contacts exhibited some Schottky barrier effects due to imperfect band alignment between the TMD and Pt, making precise control over the TMD potential challenging. Further complications (and opportunities) ares from the discovery of photoexcited current out of the plane of the TMD, through the hBN encapsulation layers, as will be discussed in the following chapter.

2

Photocurrent in hBN heterostructures

Transition metal dichalcogenide (TMD) semiconductor heterostructures are actively explored as a new platform for quantum optoelectronic systems. Most state of the art devices make use of insulating hexagonal boron nitride (hBN) that acts as a wide-bandgap dielectric encapsulating layer that also provides an atomically smooth and clean interface that is paramount for proper device operation. We report the observation of large, through-hBN photocurrents that are generated upon optical excitation of hBN encapsulated $MoSe_2$ and WSe_2 monolayer devices. We attribute these effects to Auger

recombination in the TMDs, in combination with an asymmetric band offset between the TMD and the hBN. We present experimental investigation of these effects and compare our observations with detailed, ab-initio modeling. Our observations have important implications for the design of optoelectronic devices based on encapsulated TMD devices. In systems where precise charge-state control is desired, the out-of-plane current path presents both a challenge and an opportunity for optical doping control. Since the current directly depends on Auger recombination, it can act as a local, direct probe of both the efficiency of the Auger process as well as its dependence on the local density of states in integrated devices.

2.1 Introduction

Transition metal dichalcogenides (TMDs)[54] have recently attracted significant interest for their optoelectronic properties[51], which are dominated by strongly bound excitons. As van der Waals (vdW) 2D materials, TMDs can be incorporated into complex, high cleanliness vdW heterostructures tailored to a myriad of possible applications[26]. In particular, such systems can be used to isolate and manipulate electronic and excitonic excitations which allows the creation of engineered, controlled quantum systems[3,70]. In general, such heterostructures rely on hexagonal boron-nitride (hBN)[21] as an atomically-clean dielectric encapsulation layer to separate the active materials from each other, surrounding electrostatic gates, and the environment[91]. Typically, these hBN layers

are treated as an inert buffer whose wide 6 eV bandgap[12] allows it to serve as both a physical and electronic barrier between different parts of the heterostructure device. Deviations from this simplified picture are mostly considered in the context of trapped charge defects or dielectric breakdown.

In this Article, we describe an experimental observation of a novel optoelectronic effect that challenges this simple physical picture of perfectly insulating hBN encapsulation. Specifically, we report the robust observation of a reversible, photoinduced current that appears across the thick, dielectric hBN layer. The current is observed in dozens of devices with varying geometries and hBN thicknesses, consistent with other recent reports[46,17]. We report on a systematic doping, wavelength, electric field and thickness dependent study of this effect in two different TMD materials, which allows us to unambiguously point to Auger recombination as the central mechanism involved. Our evidence is multifold. Firstly, we observe photocurrents over a wide range of hBN thicknesses (3nm - 90nm in our devices) and, secondly, when deconvolved from optical doping (Figs. B.3-B.5), it is spatially uniform throughout all devices – as verified via spatially scanning the excitation beam and by verification using split gate devices. Such uniformity and thickness independence make alternative explanations such as dielectric breakdown or tunneling via in-gap defect states in the hBN unlikely.

On the other hand, our systematic doping- field- and wavelength dependence studies, corroborated by theoretical modeling of relevant barrier heights in the two material systems, allow us to extract a Fowler-Nordheim tunneling picture that is activated by

an Auger process involving holes and excitons, which differs from previous pictures[46,28] yet has some similarities with hot-carrier effects as previously reported in graphene-hBN heterostructures[25,49,81]. Crucially, this picture explains the substantial differences in photocurrent efficiency between the two materials directly from computed band alignments, without postulating significant material-dependent variation in the efficiency of Auger excitation. This process adds an important element to the physics of two-dimensional TMD devices by introducing an optically controlled transport path outside the material. Potentially, it can be leveraged to locally sink unipolar currents from an optically-defined "contact" that can be arbitrarily swept over a device structure. In addition, we show that the variation in current generation efficiency can provide insight into the dynamics, transitions, and relaxation pathways of states within the TMD.

2.2 Photocurrents in encapsulated TMDs

Fig. 2.1a shows the schematic of a typical device structure, consisting in this case of a $MoSe_2$ monolayer encapsulated in hBN over a metal gate electrode. Upon off-resonant optical excitation at 660 nm, a substantial current is measured at the bottom gate, sourced from the $MoSe_2$ via its electrical contact. This photocurrent is substantial in magnitude - up to 6 nA for an excitation power of 15 uW - and appears only in the hole doped regime, as inferred from photoluminescence (PL) emission (Fig. 2.1b).

We first investigate the effect in detail using a dual-gated device structure in which

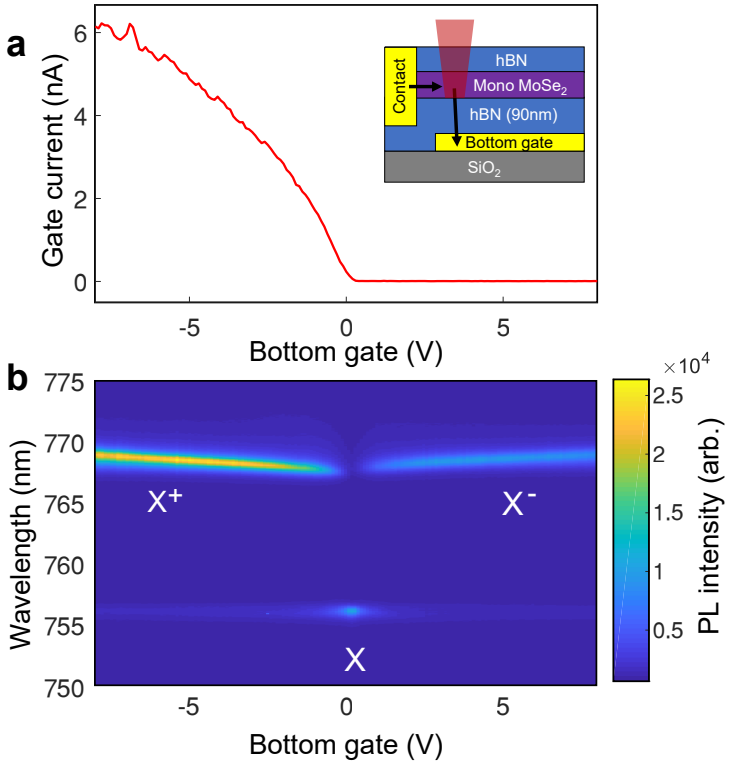


Figure 2.1: Consistent cross-hBN photocurrent a) Gate-voltage dependence of through-hBN photocurrent for the inset device structure (device A) under 15 μW, 660 nm optical excitation. This behaviour is spatially uniform and is reproduced in a series of devices of varying hBN thickness. **b**) Photoluminescent emission from the same device showing presence of photocurrent in the hole doped regime.

the TMD is grounded through a side contact and the field to the top and bottom gates can be independently varied (Fig. 2.2a). The goal of such a structure is to be able to decouple the *doping* conditions from the *electric field*, and deduce the dependence of the effect on either of them independently. Fig. 2.2b outlines the general band alignment of the TMD/hBN/gate electrode system along with the direction of the observed current. Plotting external quantum efficiency (EQE) curves as a function of bottom gate for a $MoSe_2$ device with no top gate (Fig. 2.2c), we first observe linear optical power dependence across 3 orders of magnitude, consistent with a single-photon excitation process. Here, EQE is given as the number of carriers injected into the gate per photon incident on the device structure. EQE is notably lower for the dual gate $MoSe_2$ device (Fig. 2.2d) due to absorption of incoming photons in the metal top gate. Figs. 2.2d,e show the top gate current as a function of both gates for $MoSe_2$ and WSe_2, respectively. Cuts along the labelled lines are presented and analyzed in Fig. 2.5. By fixing the potential difference between the TMD and the gate into which current flow is being measured, while varying the potential at the other, we can examine the doping dependence of the photocurrent process at fixed field. At a field of 0.15 V/nm (lines (1) in Figs. 2.2d,e) both $MoSe_2$ and WSe_2 exhibit rapid onset of current upon hole doping, and subsequent saturation with increasing carrier density. Similarly, by incrementing the potential on one gate, in opposition to the other, by a ratio proportional to their relative capacitance, one can maintain constant doping of the sample while varying the field (lines (2) in Figs. 2.2d,e), thereby yielding the pure field dependence, independent of

doping effects. While the doping dependences of $MoSe_2$ and WSe_2 appear very similar, the two materials exhibit a qualitative difference in electric field dependence, with the $MoSe_2$ current switching on rapidly at negative field while the WSe_2 current remains negligible until reaching a field of around 0.1 V/nm. Furthermore, even at high field, the external quantum efficiency of the photocurrent in WSe_2 is an order of magnitude lower than what is observed in $MoSe_2$, a distinction which persists under resonant excitation (see Fig. B.7). The decrease in top gate photocurrent at decreasing bottom gate voltage is attributed to competition between the two gates.

This competition effect becomes evident in Fig. 2.3, when expanding on the dual-gate current dependence data from Fig. 2.2, showing the currents to the top gate, bottom gate, and their sum independently. The behaviour of the bottom gate is completely analogous to the top. The total current, however, highlights that the decrease in current observed when both gates are negative can be attributed to a limited supply of hot holes tunneling in two competing directions thus reducing the current to either gate while maintaining the total.

Fig. 2.4a shows a spatial map of the photocurrent generated by scanning a diffraction limited excitation spot (see Fig. 2.4b for the sample geometry). A graphite back gate extends under part of a $MoSe_2$ flake, vertically separated from the graphite by 3 nm hBN. This geometry produces a lateral potential step when the gate potential is adjusted relative to the TMD, as schematically shown in Fig. 2.4c. Tuning to the hole side results in enhanced photocurrent generation along the edges of the gate. We attribute

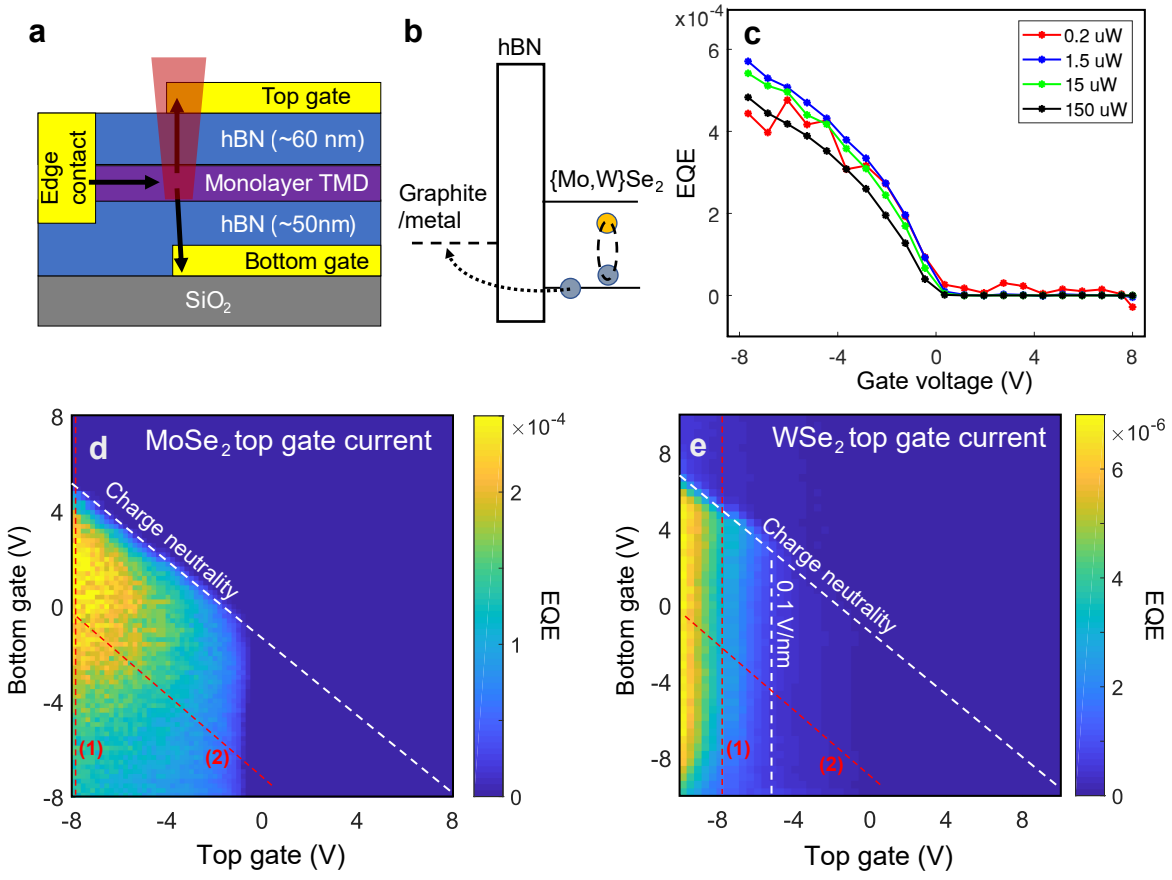


Figure 2.2: Power, field, and doping dependence in $MoSe_2$ and WSe_2 **a**) Schematic of the dual-gated, hBN encapsulated TMD structure designed to enable independent control of doping and electric field between the TMD and metal gates (device B). **b**) Band structure schematic for half of the device in (a) illustrating the hole-side photocurrent into one of the top/bottom electrodes when the TMD is hole-doped and electric field oriented towards the electrode. **c**) Quantum efficiency curves for a single-gated configuration (device A) show linear dependence on optical power. Here, EQE is the ratio of carriers through the hBN to photons incident on the heterostructure. Dependence of total current on gate conditions for $MoSe_2$ (**d**) and WSe_2 (**e**) shows qualitatively distinct characteristics. While both systems require hole doping, WSe_2 also exhibits minimal current below a field of 0.1V/nm and much lower overall quantum efficiency relative to $MoSe_2$.

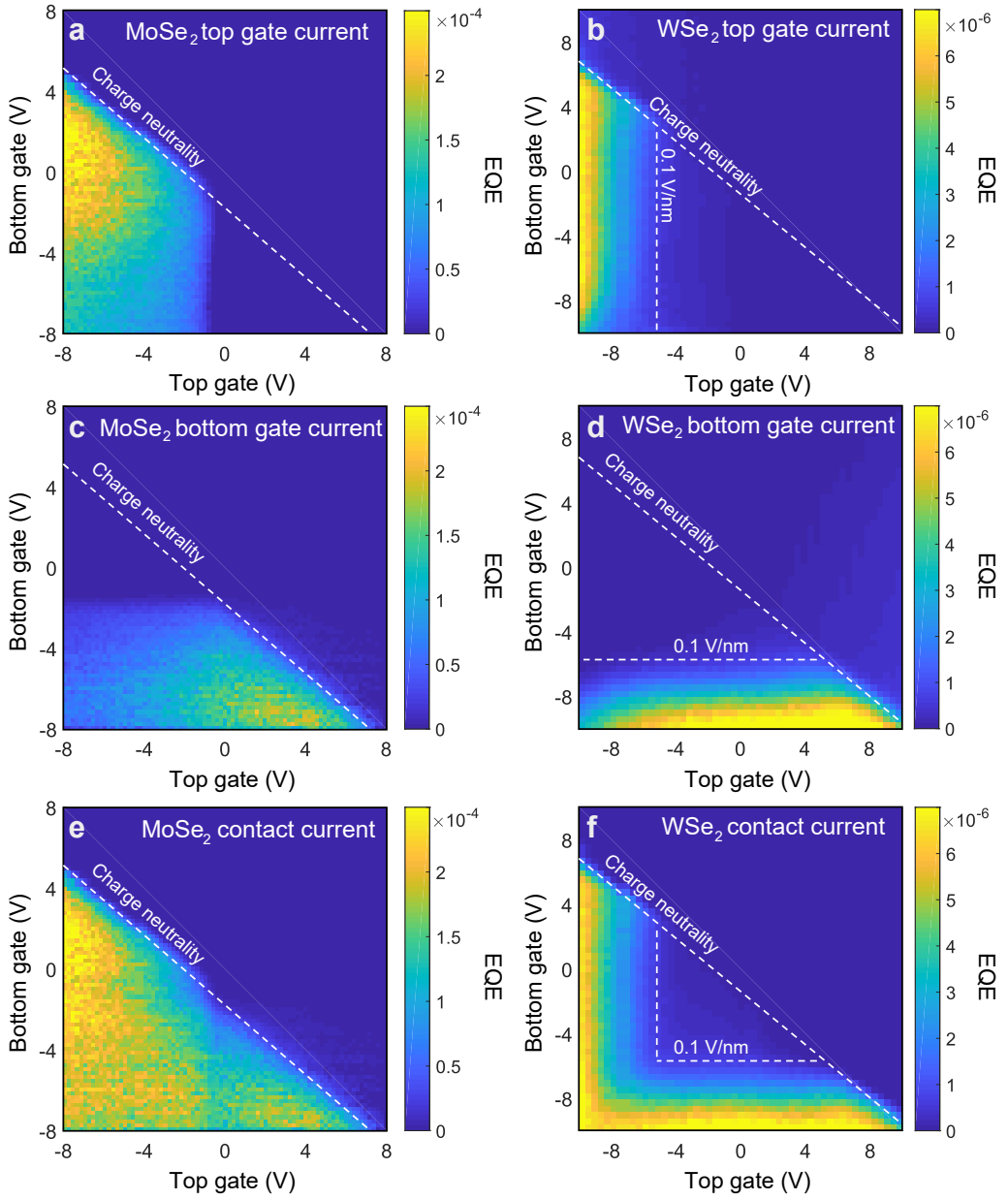


Figure 2.3: Dual-gate photocurrent measurement a,b) Top gate currents for $MoSe_2$ and WSe_2 reproduced from Fig. 2.2, shown alongside the bottom gate currents (**c,d**) and contact currents (computed here as the sum of the two gate currents) (**e,f**). We note that current only occurs under both hole doping and field that draws holes towards the relevant gate. In the case of WSe_2, the required field is significantly larger resulting in minimal current for the region of field with magnitude below 0.1 V/nm marked in (**f**). The reduction in individual top and bottom gate current when both gates are negative does not correspond to a reduction in the total photocurrent, indicating that the two gates compete for available hot holes.

this effect to details of the hole-doping mechanism for $MoSe_2$. While the Cr/Au edge contacts are transparent to electrons, they are inefficient at injecting holes into the monolayer. The presence of an in-plane potential step, however, provides an alternative doping mechanism via exciton dissociation upon optical excitation. Indeed, dissociation is energetically favorable for a sufficiently sharp step as long as the in-plane step exceeds the binding energy of the exciton [$E_b \sim 200$ meV[16]] as shown in Fig. 2.4c. This process is similar to the well known, junction-induced exciton dissociation process in organic photodetectors and solar cells, and is common to all semiconductors with tightly bound excitons[56]. The dissociated electron, subsequently, is able to leave via the contact resulting in a net hole photodoping process. As the photocurrent is a sensitive function of the doping in view of the above observations, for sufficient optical power, the steady-state photocurrent will be limited by the rate at which holes can be replenished – which is governed by this very edge-gate photodoping process. This becomes more evident at increasing optical power levels, when other doping mechanisms become comparatively negligible – we refer to Figs. B.3-B.5 for further details and dual beam, power dependent measurements confirming this picture. In addition, the doping of the sample can also be inferred from photoluminescence (PL) emission. As shown in Fig. 2.4d, placing a strong excitation laser at the gate edge while collecting PL from the center results in onset of trion emission whenever the gate potential is greater than E_b from charge neutrality (located at 0.27 V in this device). In contrast, in the absence of edge illumination, the device never accumulates holes or emits any hole-trions (Fig. 2.4e). Interestingly, the

onset of electron doping is unaffected as efficient charge injection can still occur via the contacts, independently of any photodoping effects.

While the former clearly illustrates the role of doping in the process, it does not yet elucidate by which mechanism holes are able to escape the TMD and penetrate or bypass the hBN barrier. For an interface between bulk crystals, a calculation of the band offset along with information about the momentum in the direction perpendicular to the interface would provide the necessary electronic information to understand the transport across the junction. However, for an interface between a monolayer and a bulk crystal, the notion of perpendicular momentum in the monolayer is meaningless in view of the absence of periodicity in this direction. Instead, the relevant picture is one where the entire system is considered as one interface between the monolayer and the bulk. By calculating the properties of this interface, we can then obtain the relevant transport behavior. While the exact values depend on details of the layer interface such as the orientation of the layers, interfacial reconstruction and the exact hBN layer thickness, the trends are clear and explain the observed behavior well - especially, the notable difference between $MoSe_2$ and WSe_2.

2.3 Physics of photocurrents

To capture the interface physics and explain the observed photocurrents, we start by using first principles methods to compute the density of states (DOS) of a bilayer system

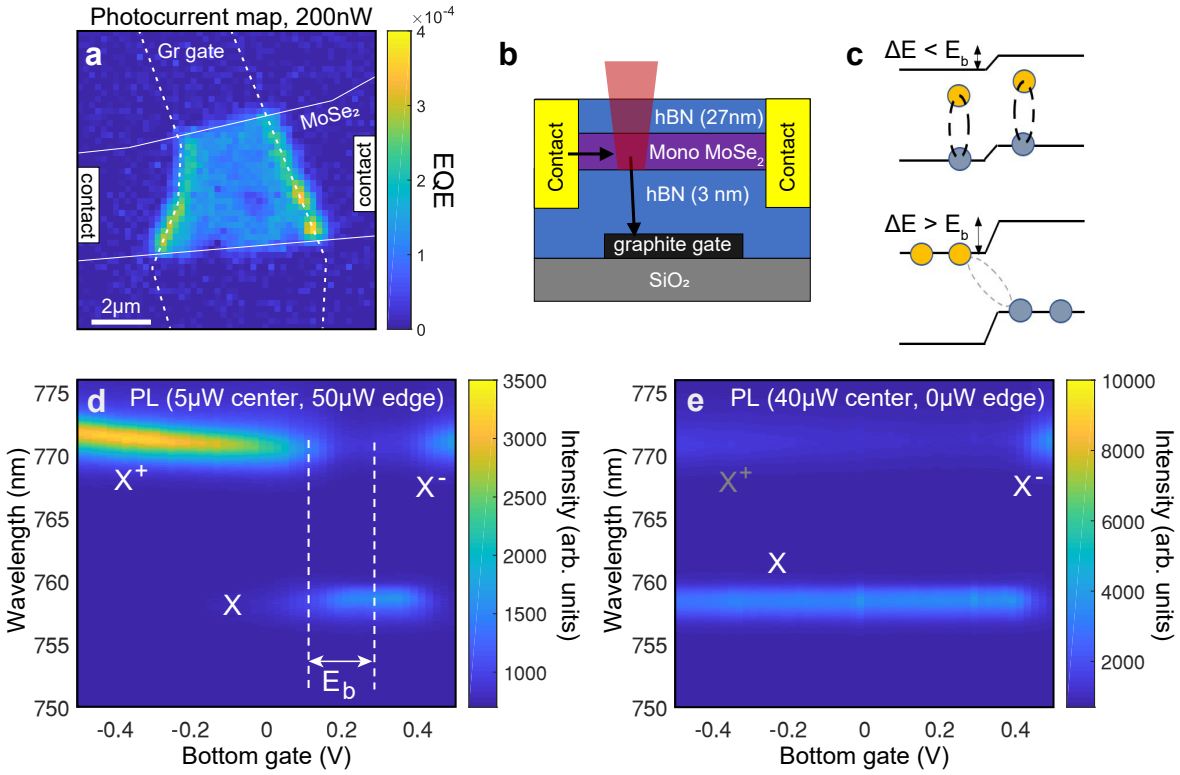


Figure 2.4: Photodoping via exciton dissociation at lateral potential steps a) Spatial photocurrent map of an $MoSe_2$ device (device C) with a local graphite back gate, schematic in (b), for off-resonant excitation at 660nm. Enhanced current is seen when the excitation laser is located near an edge of the gated region, corresponding to a lateral potential step. **c**) Schematic of exciton dissociation at a potential step, when the step height exceeds binding energy. Due to the limited ability of Cr/Au edge contacts to inject holes into $MoSe_2$, a hole photocurrent is maintained through neutral-exciton dissociation followed by an electron current into the contacts and a hole current into the gated region. **d,e**) PL spectra taken from the center of the gated region with and without 660nm excitation at the gate edge, respectively. The onset of hole doping once the potential step exceeds E_b and lack of trion oscillator strength without edge excitation indicates that photodoping is the primary mechanism for hole-doping the $MoSe_2$ structure.

that consists of one monolayer of TMD and one monolayer of hBN, after which we color each state according to its layer hybridization (Fig. 2.5a,b). The cyan states are unhybridized; i.e. the state is localized either entirely in the hBN layer or entirely in the TMD layer. The pure cyan states near the band gap in Fig. 2.5a,b should thus be understood as TMD states, as the TMD band gap is much smaller than the hBN band gap. Since the layers form an interface and interact, we now also need to consider hybridization between them, which leads to delocalization across the interface. For example, the magenta states have equal weight in the TMD and hBN layer. The colors in between pure cyan and magenta indicate a state with some weight in each layer, with ratios given according to the scale bar.

To relate these density of states plots to the transmission of charge carriers from the TMD to hBN, we note that hybridized states (denoted by any color other than pure cyan) are effectively delocalized across the interface and therefore represent a pathway for a charge carrier to move between the TMD and the hBN layers. Somewhat similar to the band offset picture in bulk heterojunctions, the distance in energy from the TMD band edge (the cyan states near the gap) to the first hybridized (non-cyan) states can now be considered the effective band offset. In agreement with other studies of $MoSe_2$/hBN systems, the valence band offset is much smaller than the conduction band offset, indicating that holes can much more readily travel from the TMD to the hBN than electrons[46,17].

These DOS plots elucidate qualitatively why the photocurrent in the $MoSe_2$ system

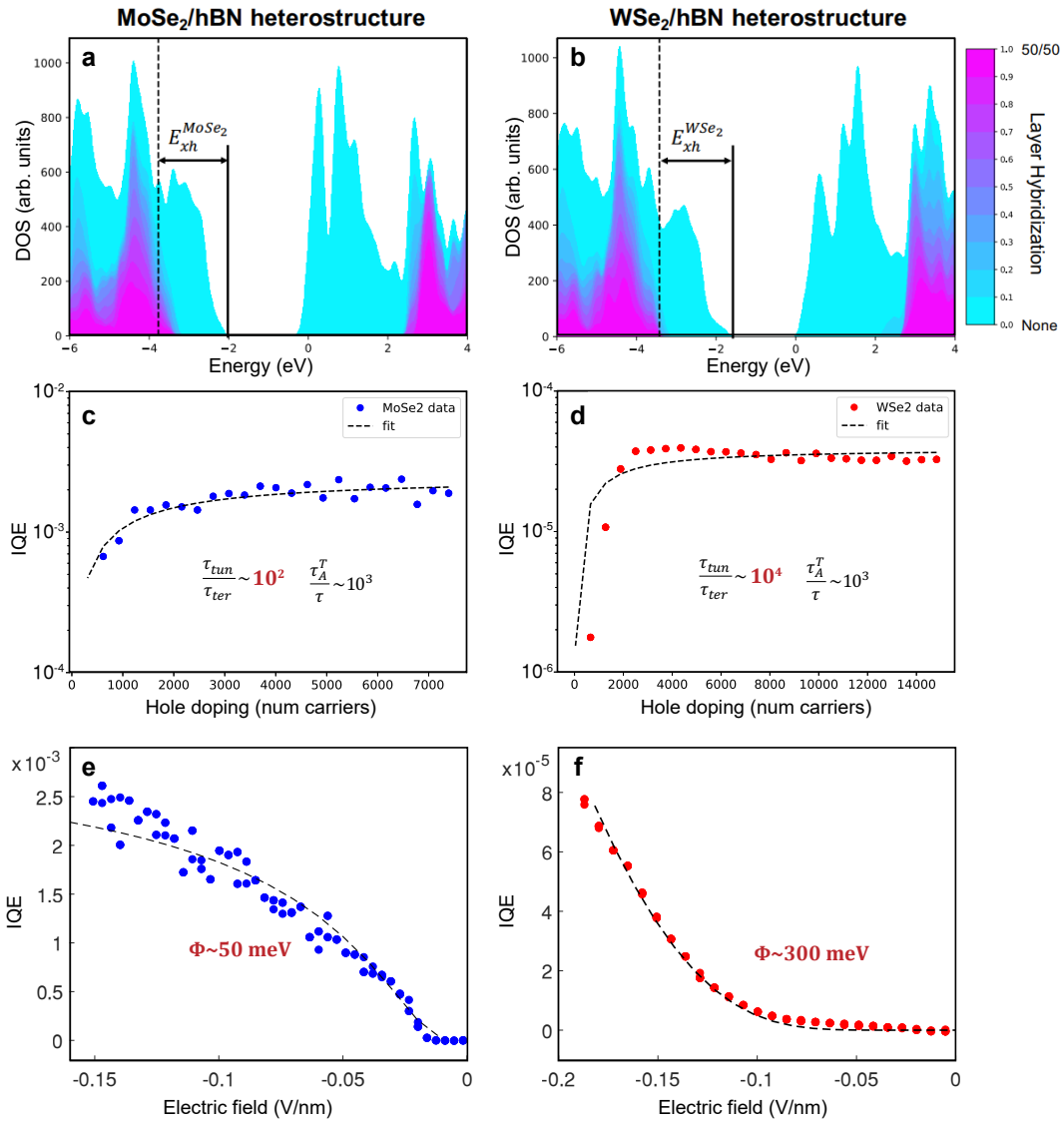


Figure 2.5: Band structure calculations and kinetics Density functional theory (DFT) calculations of hybridization between TMD and hBN states for $MoSe_2$ (**a**), and WSe_2 (**b**) : indicate a valence band offset between TMD states and layer-hybridized states on the order of the exciton energy, E_{xh}. **c, d**) Dual-gate doping dependence of photocurrent from device B fitted to extract hot hole generation rate and relative rates of tunneling and thermalization using a kinetic model. While both materials show a comparable hot hole generation, the lower IQE in WSe_2 is explained by substantially slower tunneling relative to thermalization. IQE is obtained from the EQE data in Fig. 2, after compensating for absorptivity of the TMD and photon losses in the top gate. Fitting the field-dependence of photocurrent to a Fowler-Nordheim tunneling process gives effective barriers, Φ, of 50 meV in $MoSe_2$ (**e**) and 300 meV in WSe_2 (**f**)

is larger than the photocurrent in the WSe_2 system. They also indicate effective band offsets on the order of the excitonic energy (∼1.6 - 1.7 eV.[74,20], see Fig. 2.5a, b). Since our experiments take place at cryogenic temperatures (6 K), such energies are orders of magnitude higher than the thermal energy in our system. The only process capable of providing such energies is Auger recombination, where the energy of an exciton is transfered non-radiatively to a resident carrier - in our case, a hole. In the presence of free holes, the exciton can undergo Auger recombination, during which the exciton annihilation energy is completely transferred to the hole. The hole can then scatter with a phonon in a very fast broadening process, which allows it to access hybridized states away from the K point. Consistent with the data in Fig. 2.2c, the probability of the Auger process at low excitation intensity is linear in optical power because it requires just one exciton, in contrast to the commonly studied exciton-exciton Auger recombination, which has a quadratic dependence on excitation intensity. Due to the larger conduction band offsets between the TMD and hBN, hot electrons are unable to transfer into the hBN before thermalizing - in line with the observed electron-hole asymmetry in our experiments. In addition, Auger recombination shifts a hole to an energy with a high density of hybridized states in $MoSe_2$, while the same process in WSe_2 leaves the hole at an energy with a much lower density of hybridized states, as indicated by the dashed lines in Figs. 2.5a,b. Thus, Auger recombination is much more likely to result in a hole transmitted to the hBN in the $MoSe_2$ system than in the WSe_2 system. This trend should persist regardless of the exact details of the junction such

as the exact hBN thickness. For instance, for the sake of computational efficiency we model a monolayer of hBN instead of the many different film thicknesses of hBN used in the experiments (see DFT Methods for details). Including many layers of hBN should systematically lower the valence band maximum of the hBN in each system[87], which may introduce an additional tunneling barrier the hole must overcome. Yet, a hole in the $MoSe_2$ system would still encounter a smaller tunnel barrier than a hole in the WSe_2 system.

We examine the underlying Auger mechanism in greater detail by deriving the dependence of photocurrent quantum efficiency on doping from a simple kinetic model. In this model, Auger excited holes can either tunnel through an effective barrier (the aforementioned barrier minus the hot hole energy), or thermalize. By properly accounting for charge replenishment and competing (non-Auger) exciton decay paths we can obtain approximate values for the rates of Auger recombination, hot hole thermalization and tunneling under detailed balance conditions - we refer to Appendix B for details. We can use this model in combination with the deconvolved field- and doping dependence in our devices to extract relevant values. For example, fitting our model to the doping-dependence at fixed field allows us to extract approximate values for the relative times of hot-hole tunneling to thermalization (τ_{tun}/τ_{ter}) and Auger recombination relative to all exciton decay paths (τ_A^T/τ) for each system (Fig. 2.5c,d; Appendix B for details). We find a comparable τ_A^T/τ of 10^3 for both systems. However, the relative thermalization rate (compared to tunneling) in WSe_2 (10^4) significantly exceeds that of $MoSe_2$ (10^2).

This again reflects the higher effective tunnel barrier for WSe_2 as suggested by DFT. For the tunneling process itself, we consider the field dependence of the photocurrent and model it as a Fowler-Nordheim tunneling process (Fig. 2.5e,f). The model reproduces the observed data very well, and allows us to extract effective (net) barrier heights for hot hole tunneling of 50 meV for $MoSe_2$ and 300 meV for WSe_2, consistent with the relative difference seen in DFT calculations.

We next consider the wavelength dependence of the photocurrent under resonant excitation, which clearly confirms the essential role of excitons, consistent with our Auger picture. Fig. 2.6a shows the variation in gate current from the $MoSe_2$ device in Fig. 2.4. We ensure reliable hole doping by photodoping through a strong (50 µW) above-band laser. This value exceeds that of the other rates in our system, and ensures barrier limiting (as opposed to charge-replenishment limited) behavior. When subsequently sweeping a variable wavelength laser (5 µW) we observe a pronounced set of resonances. Comparing those against the photoluminescence emission spectrum (Fig. 2.5b) we observe photocurrent emission coinciding with the exciton and hole-trion resonances - as expected from the perspective of an Auger picture involving excitons and holes. The substantial photocurrent from the neutral exciton in the hole-doped regime, despite low population in PL, suggests an interesting interplay between the hole-exciton scattering mechanisms that create hole-trions (also referred to as attractive polarons[75]) and Auger processes. These observations imply that photocurrent may provide an interesting probe of exciton dynamics, and could be used to shed light on varying decay mechanisms

in TMDs as well as novel thermalization physics - as already suggested by our kinetic model.

2.4 Photocurrent and upconversion

Finally, we consider similarities between the photocurrent mechanism and a previously documented Auger exciton upconversion process[28]. When a TMD was excited on resonance with the lowest energy 1s exciton, PL emission was observed at higher energy (Rydberg) states[16], including the 2s exciton and B exciton from a higher conduction band. In[28], this phenomenon was attributed to exciton-exciton annihilation, a related Auger process in which one exciton non-radiatively transfers its energy to another, hot exciton. We indeed observe this phenomenon in our $MoSe_2$ devices (Fig. 2.6c), allowing us to examine the relationship between these processes. In reflectance measurements (Fig. 2.6d) we observe that the B exciton state exists in both the neutral and the hole-doped regime. However, in PL, which measures population, we observe a rapid suppression of the B exciton upconverted emission with hole doping (Fig. 2.6c), while observing the presence of a pronounced photocurrent in this regime. These observations suggest a competition between the hole-Auger process and the upconversion process: the exciton-exciton Auger process necessary to create the hot excitons that ultimately relax into the B state appears to compete with the hole-exciton Auger process. From a microscopic perspective, these observations are consistent with the relative densities of

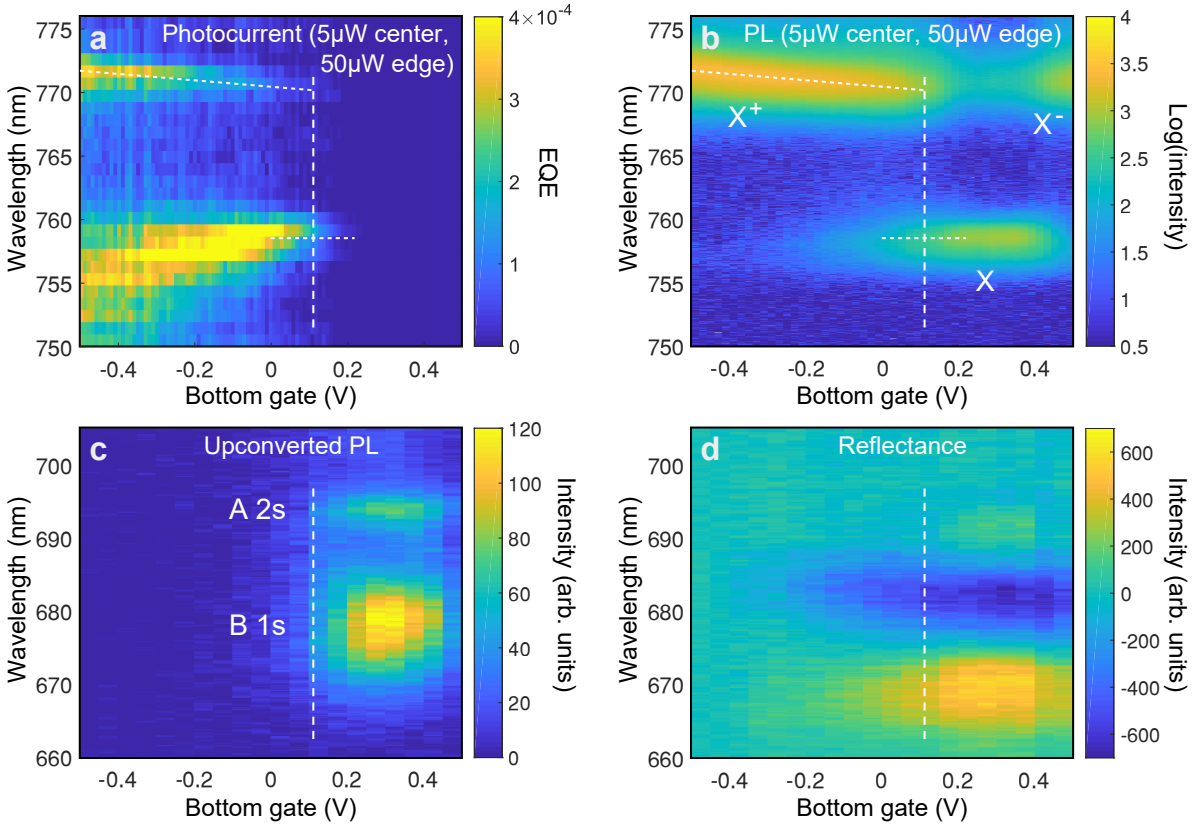


Figure 2.6: Photocurrent under resonant excitation and competition with exciton upconversion a) $MoSe_2$ (device C) photocurrent differential for 50 μW off-resonant gate-edge excitation and 5 μW variable-wavelength center excitation shows current following the exciton and trion resonances seen in PL in (**b**). **c**) Upconverted photoluminescence spectra taken at 759 nm excitation, documented in literature to arise from Auger excitation of the 1s A exciton, yielding emission of higher Rydberg states, along with the B exciton. **d**) Reflectance spectra indicating that the B exciton state persists in the hole-doped regime. The onset of hole-doping, however, corresponds to a loss of photoluminescence from the B exciton state and a corresponding onset of photocurrent, suggesting a competition between exciton-exciton Auger and exciton-hole Auger, with the latter dominating in the doped regime.

holes and excitons in our system. To first order, from a gate capacitance model, we expect a hole density of $\sim 7 \times 10^{12}\text{cm}^{-2}\text{V}^{-1}$ which exceeds the approximate exciton density of $\sim 10^{10}\text{cm}^{-2}$ at only a few mV past the onset of hole doping. Assuming somewhat similar exciton-hole and exciton-exciton Auger recombination rates would then indeed suggest a significant suppression of upconversion upon doping due to simple competition between the two processes. More detailed analyses, with independently calibrated carrier and exciton densities, could therefore be used in combination with photocurrent and upconversion measurements to bound the ratio between these respective rates more tightly.

In Fig. 2.7a, we consider upconverted PL from resonant excitation of a different $MoSe_2$ device with considerably higher hBN thickness (90 nm rather than 3 nm). As in Fig. 2.6, reflectance data (Fig. 2.7b) indicates the lower energy s2 Rydberg state of the A exciton is suppressed by hole doping, but the B exciton persists in the doped regime. Upconverted PL emission, meanwhile, drops off rapidly with hole or electron doping. Photocurrent onset (Fig. 2.7c) corresponds similarly to the dropoff in upconverted PL. In these data, we also clearly see symmetric behaviour on the electron side in PL and reflectance, suggesting competition with hot electron generation. Due to the comparatively higher barrier, however, these electrons are not able to tunnel through the hBN leading to asymmetry in the photocurrent data.

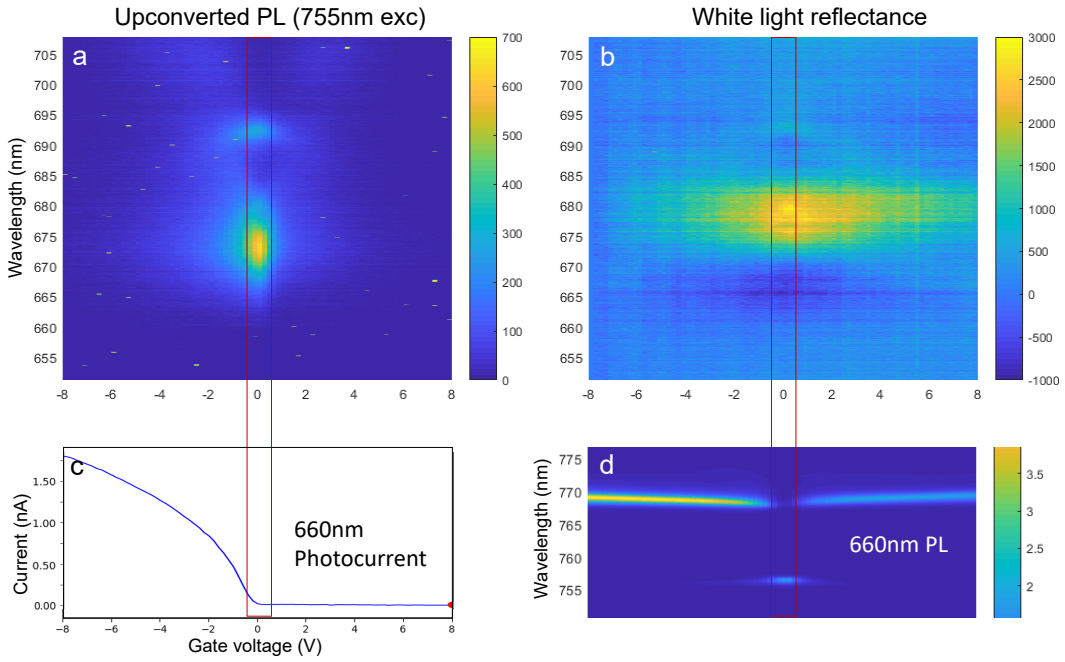


Figure 2.7: Photocurrent competition with exciton upconversion Analogous data to Fig. 2.6, demonstrated on a $MoSe_2$ device with 90 nm thick hBN rather than 3 nm. Despite the substantial difference in thickness, the devices exhibit equivalent physics as would be expected for the proposed Auger model.

2.5 Contactless hole injection and gate-dragging effects

In contrast to the other devices in this study, where optical excitation was performed in a region with a conductive local gate opposite the TMD, we consider here a phenomenon that occurs when an hBN-encapsulated TMD structure is placed directly over an Si/SiO_2 wafer bottom gate. In this structure, gating through the combined 285 nm SiO_2/50 nm hBN can achieve doping control similarly to locally gated structures. Hot holes, however, can only cross the hBN layer and are stopped by the oxide leading to no measurable photocurrent. We do, however, observe an indication of the process via hysteretic doping behaviour of the TMD as the Si bottom gate is varied. When swept from an electron doped regime at positive gate voltage towards negative voltage, PL measurements indicate a transition through charge neutrality and towards mild hole doping but do not indicate any greater doping for increasingly negative gate voltage. Reversing the sweep towards positive, however, quickly brings the device through to electron doping much earlier than would be expected from the downward sweep. An example of this effect is provided in Fig. 2.8. Furthermore, after repeated sweeps to increasingly negative voltage, the transition towards electron doping on the upward sweep and away from electron doping on the subsequent down sweep will also shift down to a voltage slightly above that at which the previous sweep turned around. This "ratcheting" behaviour and inability to significantly hole dope is consistent with photocurrent across the hBN establishing a layer of positive charge at the hBN-SiO_2 interface, screening the bottom

gate thus preventing further doping. Due to the lack of electrical contact to this interface, the positive charge persists upon increased bottom gate voltage, substantially shifting the condition for charge neutrality. This charging was observed to dissipate over the course of multiple hours, gradually restoring the initial charge neutrality conditions for the device.

This effect is significant in the context of Chapter 1, as it contributed to the challenges of gate control of the quantum dot device. Though the mechanism was not understood at the time of those experiments, gate-dragging was observed with the global back-gate, making it very difficult to establish a consistent dot potential. With an understanding of the mechanism, however, the hysteretic effect can be eliminated by placing a conductive gate directly adjacent to the encapsulating hBN layer such that, even in the presence of photocurrent, charge accumulation is prevented. An understanding of photocurrent and dissociation doping, however, also opens up a range of opportunities for quantum dot device structures and control. For instance, an isolated dot region without any in-plane channels for charge injection could be doped through dissociation of excitons along the edge of the confining potential, provided said potential is sufficiently steep and the well sufficiently deep. A potential well with confined holes could also be optically discharged by lowering the confining potential enough that exciton dissociation is prevented, while still allowing for photocurrent to a gate underneath the dot region to deplete holes from the well. In a material like WSe_2 the presence of a threshold field below which no significant photocurrent is observed means that field strength could be used to transition

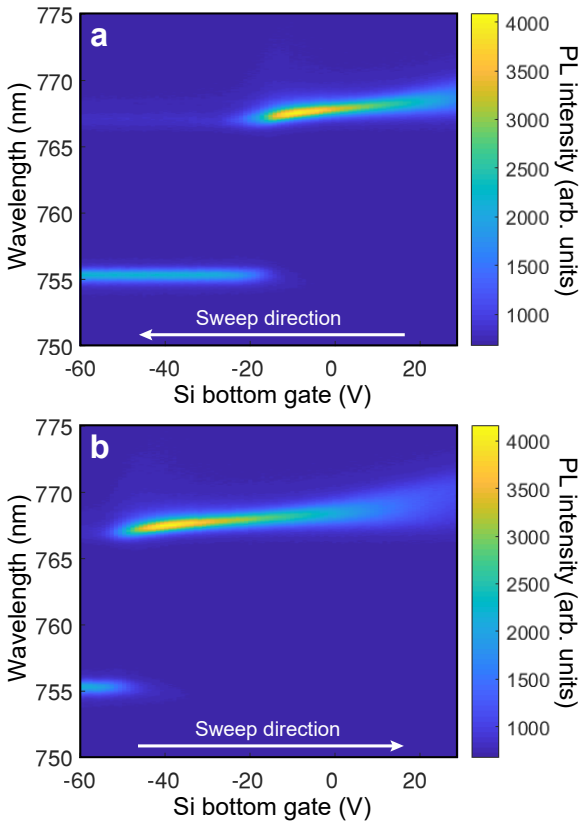


Figure 2.8: Contactless charge injection and gate dragging PL spectra under 660 nm excitation for an encapsulated $MoSe_2$ device separated from a Si bottom gate by a 285 nm oxide dielectric. Upon a downward sweep in gate voltage (**a**) the TMD passes through the undoped regime but is only able to weakly hole dope, with no changes to PL emission for arbitrarily negative gate voltage. When the sweep is subsequently reversed, however, a rapid transition to electron doping is seen. This behaviour is consistent with an accumulation of trapped charges at the hBN-oxide interface, built up by photoexcitation of holes during the downward sweep and locked in place due to the lack of direct electrical contact to charge traps at this interface between two insulators.

between loading and optical control over a dot region, with minimal unwanted charge transfer during the latter mode of operation.

2.6 Conclusion

In conclusion, we have shown that photoexcitation of excitons in hBN-encapsulated TMDs can give rise to a form of 'photoelectric effect' for holes that results in a net and substantial current across the nominal hBN dielectric barrier. We attribute this effect due to Auger-generated hot holes being swept through the barrier by the electric field in a tunneling process, which we substantiate by careful field, doping, wavelength and power dependencies. We further support our claims with detailed, ab initio calculations that match well with our observations of a systematically higher effective hole tunnel barrier for WSe_2 as compared to $MoSe_2$. In addition to shedding light on the intrinsic Auger effects in TMDs, which are important to evaluate their device performance as photodetectors and other optoelectronic devices, our studies also demonstrate the spectroscopic potential of photocurrent studies, and provide a novel probe to study non-radiative effects such as carrier thermalization in 2D semiconductors. Intriguingly, if further studies confirm a certain degree of coherence in the photoelectric effect, our findings may open the door for on-chip, integrated probing of the local density of states – in a way similar to advanced spectroscopic techniques such as ARPES, but with greatly reduced complexity and with nanoscale resolution.

3

SEM Imaging 2D heterostructures

3.1 Introduction

The optical and electronic properties of van der Waals (vdW) heterostructures[21,26,61] depend strongly on the atomic stacking order of the constituent layers. This is exemplified by periodic variation of the local atomic registry, known as moiré patterns, giving rise to superconductivity and ferromagnetism in twisted bilayer graphene[8,9,73] and novel exciton states in transition metal dichalcogenides (TMD) heterobilayers[82,72,33,1].

However, the presence of the nanometer-scale moiré superlattices is typically deduced indirectly, because conventional imaging techniques, such as transmission electron microscopy (TEM)[32,93], require special sample preparation that is incompatible with most optical and transport measurements. Here, we demonstrate a method that uses a secondary electron microscope to directly image the local stacking order in fully hexagonal boron nitride (hBN) encapsulated, gated vdW heterostructure devices on standard Si-substrates. Using this method, we demonstrate imaging of reconstructed moiré patterns in stacked TMDs, ABC/ABA stacking order in graphene multilayers[52], and AB/BA boundaries in bilayer graphene[83,55,38]. Furthermore, we show that the technique is non-destructive, thus opening the possibility of directly correlating local stacking order with optical and electronic properties, crucial to the development of vdW heterostructure devices with precisely controlled functionality. Our technique could enable rapid, high-resolution determination of the morphology of CVD grown vdW structures allowing for the optimization of large area devices, as required for the deployment of vdW materials as a commercially viable device platform.

Characterising stacking orders, stacking defects and moiré superlattices is essential to a complete understanding of and control over 2D material systems. Studies of effects such as Mott insulator and superconducting states in ABC-stacked trilayer graphene[14,15], and topologically protected states along the AB/BA boundaries in bilayer graphene[55,38,92,77] require spatially-resolved determination of the stacking order. Moreover, in twisted vdW structures, imaging of the moiré pattern is essential for understanding how optical and

electronic properties depend on moiré periodicity[8,9,80,89], as well as effects of superlattice inhomogeneity and lattice reconstruction. In fact, the layers can twist and reconstruct during fabrication, often causing the moiré superlattice to vary spatially and differ from the target stacking angle, greatly complicating interpretation of experiments. For instance, it was recently shown that interactions between the lattices in a bilayer graphene structure caused spatially varying reconstruction patterns that differed significantly from the conventional moiré picture of a smoothly-varying potential[93].

3.2 SEM Imaging basics

Scanning electron microscopy is a versatile set of techniques for high-resolution imaging. In comparison to optical imaging, the significantly higher momentum of accelerated electrons results in a probe beam that is many orders of magnitude smaller in wavelength. Indeed, for a beam of 1 keV electrons we can readily compute

$$\lambda = \frac{h}{p} = 39pm$$

The practical resolution, however, is limited by the quality of the electron focusing and the interaction volume between the probe beam and the sample. In practice, the resolution is therefore tends to vary from a few nm to hundreds of nanometers, depending on the excitation beam energy and detection mode.

The interaction of the incoming electron beam with the sample can give rise to a

wide range of detectable effects, ranging from electron backscatter, to x-ray emission and current injection into the sample. Consequently, there exist a very wide range of detection modes under the umbrella of SEM imaging[19]. We focus in the following on two modes: secondary electron emission - the mode leveraged for the 2D material imaging technique laid out in this work, and electron backscattering - an established technique for characterizing material structure.

Figure 3.1 shows a cartoon representation of these two scattering modes, with secondary electrons coming from the interaction of the primary beam with electrons in the sample, while backscattered electrons come from an elastic interaction between primary electrons and the nucleus. For a crystalline solid, the locations of the nuclei from which electrons can backscatter will have a periodic structure which makes it possible to observe diffraction effects in the angular distribution of backscattered electrons. By collecting backscattered electrons on an angle-resolved detector such as a phosphor screen imaged by a digital camera it is therefore possible to directly interrogate the crystal structure of the sample, in a technique known as Electron Backscatter Diffraction (EBSD)[68]. Similarly, structure can be interrogated by measuring the total backscatter intensity while varying the angle of the incident primary beam, since the rate of backscattering will depend on the beam angle relative to the Bragg condition for the lattice[36]. This approach is named Electron Channeling Contract Imaging (ECCI), in reference to the open "channels" through which the primary beam can pass with low backscattering when orthogonal to a crystal plane. Furthermore, crystal defects or dislocations can be spatially resolved by scanning the

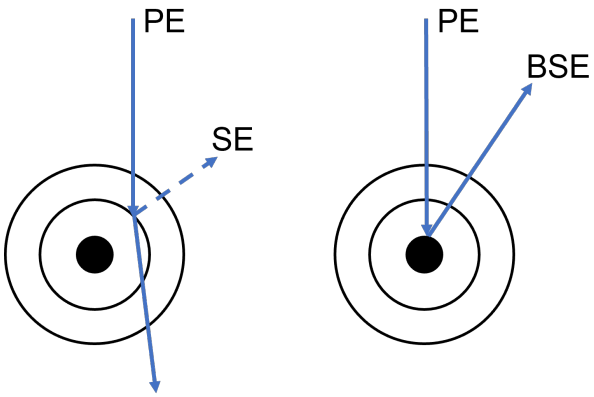


Figure 3.1: Two SEM interaction modes Cartoon of two scattering modes of the primary electron beam with a sample. Left, the generation of low energy secondary electrons via interaction of the primary with a sample electron. Right, the elastic backscattering of a primary electron by a sample nucleus.

primary beam at a fixed angle over the sample while observing backscatter intensity. When the primary beam is angled such that it "channels" deep into the sample with low backscatter, any local disruption to the crystalline pattern will increase the rate of backscatter leading to a detectable signature.

These backscattering techniques, however, suffer from the limitation that, due to the small scattering cross section of the atomic nucleus, the overall rate of signal accumulation is slow, in the range of tens of minutes to hours[13]. For bulk crystal samples, this drawback is balanced by the large quantity of crystallographic information that can be obtained from a single image. When examining few-layer 2D material structures, however, the available interaction volume is minuscule compared to the hundreds of nanometers to microns of depth that the primary beam interrogates[37].

Secondary electron imaging, is, in many ways, the opposite of of backscattering techniques. Secondary electrons are low energy but generated in large quantities as the energetic primary beam scatters off and ejects electrons from the sample. Collection is performed on an Everhart-Thornley detector which can be biased to attract and accumulate emitted secondary electrons independently of position and emission angle. This makes it a very effective technique for high resolution spatial imaging with a resolution primarily determined by the focus of the primary beam and the secondary electron escape depth, as illustrated in Figure 3.2. The escape depth λ depends on the material[71] and secondary electron energy distribution, with the latter being affected by the energy of the primary beam[35]. From this high level description it would seem that secondary electron imaging is best suited to spatial rather than crystallographic information, as the secondary electrons do not carry any information on the structure of the lattice from which they originated. In this chapter we find, however, that the concept of channeling of the primary beam can still be applied in secondary electron imaging to extract structural information from atomically thin layers.

3.3 Channeling Modulated Secondary Electron Imaging

Due to the aforementioned limitations of traditional SEM-based crystallographic imaging techniques, direct imaging of 2D material lattice structure is typically achieved with TEM[32,93], which requires placing the samples on thin (50 nm) TEM grids – incompatible

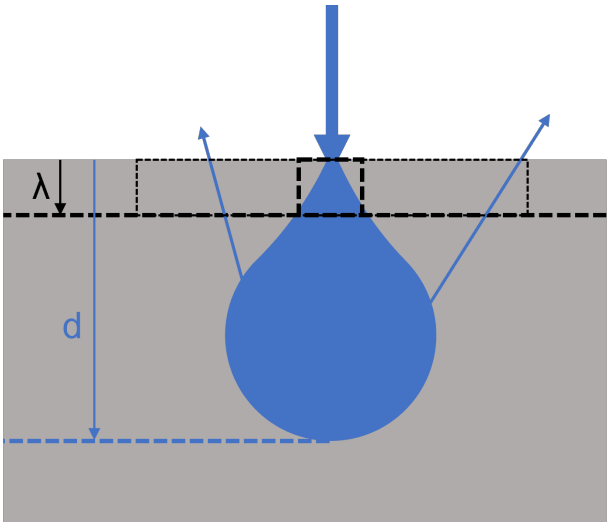


Figure 3.2: Secondary electron emission Schematic of the interaction volume between the primary electron beam and the sample (blue). The interaction depth depends on the material and beam energy but is usually in the range of 1 um. Secondary electrons are generated throughout the interaction volume but, due to their considerably lower energy, have an escape depth λ on the order of a few nm. Escaping secondary electrons from any location in the sample are collected on a single detector so the resolution is determined primarily by the focus of the primary beam and secondary escape depth, as highlighted by the bold dashed box. Backscattered electrons also generate secondary electrons so the image is also reduced slightly by the associated emission from the light dashed box.

with most device fabrication techniques. In the case of post-measurement TEM imaging, the 2D heterostructures must be separated from the contacts, picked up and transferred onto the TEM grid. Apart from being technically challenging, this procedure likely distorts the lattice alignment. Moiré patterns have also been imaged using atomic force microscopy (AFM)[88] and scanning tunneling spectroscopy (STS)[39], but this requires direct contact with the active area of the heterostructure, thus preventing the use of hBN encapsulation and top gates. While scanning electron microscopy (SEM) techniques do not generally suffer from these limitations, conventional SEM techniques used for crystallographic imaging, such as angle-resolved electron backscatter diffraction (EBSD)[68] and electron channeling contrast imaging (ECCI)[18] rely on detection of backscattered primary electrons, which is not efficient enough to probe mono- or bilayer materials. In recent studies of conventional, covalently bonded semiconductors, it was pointed out that the channeling of primary electrons through a lattice also affects the generation of secondary electrons[2] allowing for direct imaging of the surface lattice ordering of SiC.

Our approach, illustrated in Fig. 3.3a, involves the use of an SEM with a generic, yet highly sensitive Everhart-Thornley (E-T) secondary electron detector[24]. The device under study is positioned at an angle with respect to the incoming electron beam - the energy of which is varied between 0.5 keV and 15 keV. The SEM signal comes from the generation of secondary electrons at different depths, the extent of which depends on the ability of the primary beam to channel through the stack. In order to understand how the technique, which we here refer to as "channeling modulated secondary electron

imaging", resolves atomic stacking order, we first consider a simple system consisting of naturally occurring AB/BA stacking orders in graphene.

Figures 3.3b-c show images of a bilayer graphene flake on a SiO_2-on-Si substrate, acquired with optical microscopy and SEM, respectively. While the former is homogeneous, confirming that the flake has uniform thickness, SEM imaging at a 24° tilt angle uncovers two types of distinct domains. As the stage is rotated azimuthally, the number of secondary electrons collected from these domains exhibits 120°-periodic oscillations, with a 60° phase shift between the two domain types (Fig. 3.3d). We attribute the observed domains to different levels of electron channeling at a given azimuthal angle through naturally occurring regions of AB- and BA-stacked graphene[83,55,38,92]. Such channeling arises at particular polar and azimuthal angles, when the incoming electrons are oriented parallel to the open cavities or "channels" within the atomic lattice, allowing them to travel through the material with minimal scattering. In particular, channeling conditions are optimised every 120° (Fig. 3.3d, inset), and the 60° relative angle between AB and BA domains causes the observed phase difference. Since graphene has a lower atomic number, Z, than the substrate, it generates fewer secondary electrons (Fig. 3.3c, inset)[35]. Thus, for graphene on oxide substrates, the secondary yield maxima occur when channeling is maximised.

Turning to a thicker (approx. 6 layer) graphene flake, which also exhibits domains in SEM imaging that are not observable optically (Figs. 3.4a-b), we find a more complex azimuthal dependence (Fig. 3.4c). While one domain type (red) is 60°-periodic in

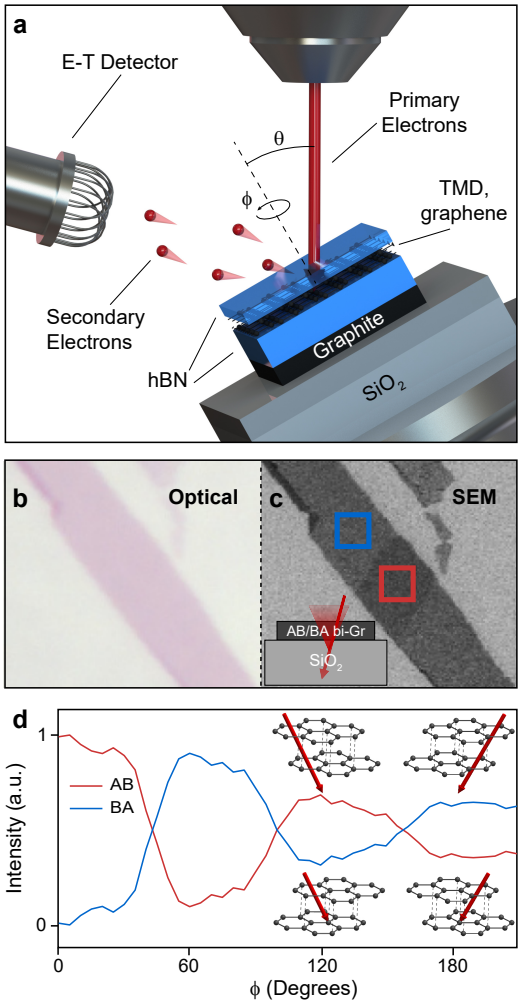


Figure 3.3: SEM based imaging of vdW heterostructures: operating principle and simple example a) Schematic of operating principle: an accelerated electron beam is focused onto the device, which is placed at a non-zero polar angle (θ) and can also be rotated azimuthally (ϕ). Channeling of the incident electrons through the van der Waals stack and subsequent secondary electron generation depend on the effective scattering cross-section at the given incidence angle. Collecting the secondary electrons on a sensitive Everhart-Thornley (E-T) detector thus allows for imaging the local stacking order. **b**) Optical image of a naturally occurring bilayer graphene flake, showing homogeneous thickness. **c**) SEM image of the same flake as in (**b**) ($\theta = 24°$, $\phi = 5°$), revealing areas of different contrast. **d**) Dependence of SEM secondary yield on azimuthal angle for locations marked by boxes in (**b**) (normalised to the mean). The two regions display $120°$ symmetry and $180°$ phase offset, consistent with AB and BA domains: every $120°$, channeling is maximised for one domain type, and minimised for the other (inset schematics). Contrast decays at increasing angle due to gradual charging of the substrate over time.

azimuth angle, the other (blue) exhibits a period of 120°, reflecting a lower inherent symmetry. In particular, the two curves have nearly equal amplitude at 60° but the domain represented in blue exhibits significantly stronger signal at 0° and 120°, suggesting a greater degree of channeling at these angles. To highlight the lower symmetry regions, we present in Fig. 3.4d a spatial map of the ratio between the signals at 0° and 60° as a function of position - clearly pronouncing the middle section of the flake. We find that this more complex pattern is due to ABA- and ABC-stacking orders[52], as can be independently verified with Raman spectroscopy[59] through the position of the Raman 2D peak (Fig. 3.4e). Indeed, consistent with our observations, the two domain types are expected to have similar scattering cross sections at certain rotation angles (Fig. 3.4c, left inset), while at other angles, the ABC domain allows for "complete channeling" (Fig. 3.4c, right inset), giving rise to enhanced SEM signal every 120°.

The graphene domain imaging demonstrated above is applicable to twisted van der Waals heterostructures. Figure 3.5a shows an SEM image of an hBN-encapsulated, dual-gated, twisted bilayer of WSe_2 (Fig. 3.5a, inset) henceforth referred to as device D1. In the SEM image, clear triangular lattice reconstructions are visible, with domain sizes ranging from ∼50 nm to ∼300 nm. These results indicate that the relative twist angle is strongly position dependent, and that interactions between the respective lattices are strong enough to dominate over the in-plane stiffness of the respective layers. The end result is that the two WSe_2 layers lock locally into energetically favourable AB or BA stacking configurations - similar to what was previously observed in twisted bilayer

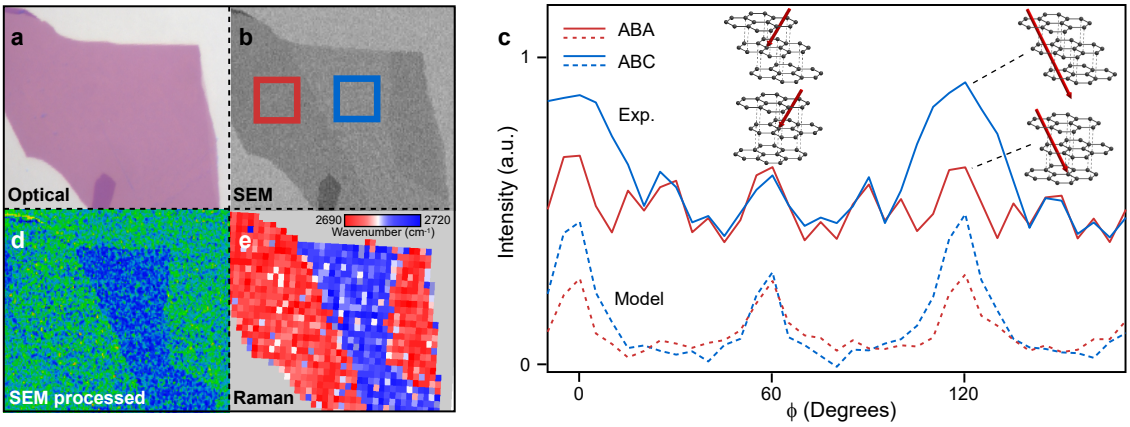


Figure 3.4: Channeling contrast based SEM imaging of multilayer graphene a-b) Optical and SEM images of a natural few-layer graphene flake, again highlighting structural contrast that is not visible optically. **c**) Azimuthal angle dependence, showing qualitatively different behaviour in the two boxed regions in (**b**), consistent with ABC and ABA stacking: while ABC stacking exhibits fully open channels every $120°$, ABA stacking shows only partially open channels every $60°$. **d**) Difference between two SEM images with a $60°$ offset in azimuthal angle. As expected from (**c**), this selectively reveals ABC domains. **e**) Spatial map of Raman 2D-peak position, confirming the ABC/ABA stacking order in the different domains.

graphene through TEM imaging[93]. Critically, our imaging technique is compatible with optoelectronic device operation, retaining narrow ∼3 nm linewidths, and electrostatic gate tunability after over 6 hrs of SEM imaging at energies up to 15 keV (see SI). These observations indicate that the device maintains excellent optical properties after SEM imaging, and thus demonstrate the powerful potential of the present technique: namely, spatially correlating optical spectra with directly imaged local lattice configuration.

3.4 Imaging encapsulated structures

A key feature of our technique is the ability to image 2D materials fully encapsulated in hBN, which is known to enhance both optical and electronic properties[21]. In Fig. 3.6, we explore the dependence of the SEM contrast on hBN thickness, by imaging a heterostructure composed of a stepped WSe_2 flake under a perpendicularly stepped hBN flake. An optical image of the sample and the hBN thickness profile (acquired with AFM) are shown in Fig. 3.6a. As with general secondary electron techniques, the depth to which we can image is determined not by the total penetration of the primary beam (typically on the order of microns) but rather by the ability of secondary electrons to escape the material. Increasing the acceleration voltage increases the energy of the secondary electrons[35], corresponding to a greater imaging depth, as illustrated in Fig. 3.6b. At primary energies below 1.5 keV (left) the secondary electrons are only collected from the top layers of hBN, with no WSe_2 signal through hBN thicker than ∼

10 nm. At an energy of 3 keV (right) the imaging depth exceeds the thickness of the heterostructure, revealing the complete thickness variation in the hBN and underlying WSe_2. Increased imaging depth, however, reduces individual layer contrast, as can be seen in the mono-, bi- and tri-layer WSe_2 steps along the right edge of the image. Nevertheless, at a reasonable acceleration voltage, monolayer steps in the TMD are clearly visible through more than 27 nm of hBN.

To determine the visibility of different stacking orders through increasingly thick hBN encapsulation, we focus on the azimuthal angle dependence from natural AA'-stacked WSe_2. The azimuthal dependence of the bilayer and trilayer SEM signal for different hBN thicknesses and the corresponding contrast (root-mean-square amplitude) are displayed in Figs. 3.6c,d and e, respectively. Due to the crystalline nature of the top hBN, the raw secondary yield of the bilayer is convolved with channeling effects in the hBN. Yet, we can conveniently correct for this convolution by dividing the raw yield by the secondary yield from an adjacent region of equal hBN thickness but without underlying TMD. We observe that contrast indeed decreases with hBN thickness, but nevertheless persists through to 27 nm. Our ability to resolve signals at large depth is mainly limited by uncertainty in this background deconvolution, as the amplitude of the channeling effect in thick hBN significantly exceeds that of the bilayer. Spatially resolvable contrast, for instance, between AB/BA domains in a bilayer, can of course be imaged directly without such compensation. Since 27 nm thick top-layer hBN is sufficient for most device applications, it appears that our technique is applicable to a wide range of encapsulated

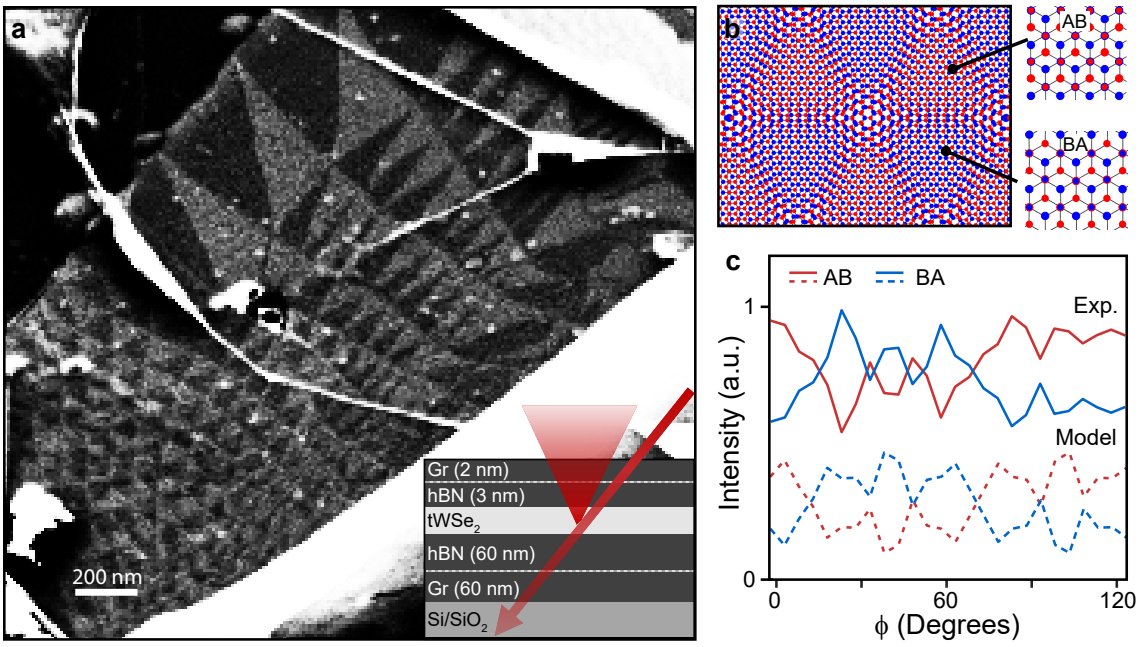


Figure 3.5: Imaging of fully hBN-encapsulated twisted vdW heterostructure a) Representative images of the contrast that appears in a twisted bilayer WSe_2 device. Due to the interaction between the respective layers, a spatially varying reconstruction pattern develops, determined by strain and the local mismatch angle (see text for details). Inset: Device schematic. **b**) Schematic illustration of a twisted bilayer in the strained reconstruction regime. For small misalignment angles, the interlayer interactions locally lock the lattice into domains of AB and BA stacking with strain accumulated at layer boundaries. For a given polar angle, the two stacking orders facilitate optimal channeling conditions at different azimuth angles, giving rise to a contrast image. **c**) Azimuthal angle dependence of the signal from AB and BA domains (solid red and blue curves, respectively), along with predictions based on the model presented in the main text.

vdW heterostructures.

Critically, our technique is compatible with optoelectronic device operation, as shown in gate-dependent photoluminescence measurements (Fig. 3.7) of a hBN-encapsulated monolayer WSe_2 device that was imaged with SEM for several hours. We observe clear exciton emission from both bright (X_0) and dark (X_D) exciton states, with very effective gate-tunability, manifested by the appearance of red-shifted charged excitons (X^+ and X^-) in the p- and n- doped regimes. The intrinsic regime occurs for gate voltages near 0 V (-3.5 V$< V_G <$0.5 V) at a hBN dielectric thickness of 30 nm, indicating that the sample is only minorly doped after imaging. Moreover, the device exhibits very narrow ($\sim$3 nm) linewidths after imaging, allowing for observing even the small ($\sim$2 nm) splitting of inter- and intravalley trions due to exchange interactions. These observations indicate that the device maintains excellent optical properties and effective gate tunability after SEM imaging.

3.5 Computational model of SEM signal

Our observations can be understood from a simple, semi-classical model of channeling physics. By representing the 3D configuration of atoms within the material, and assigning a soft radially-dependent electron transmission probability[57] to each, we compute the mean transmission for a series of parallel electron beams at a given polar and azimuthal angle (for details, see Appendix C). For a TMD bilayer encapsulated in lighter elements

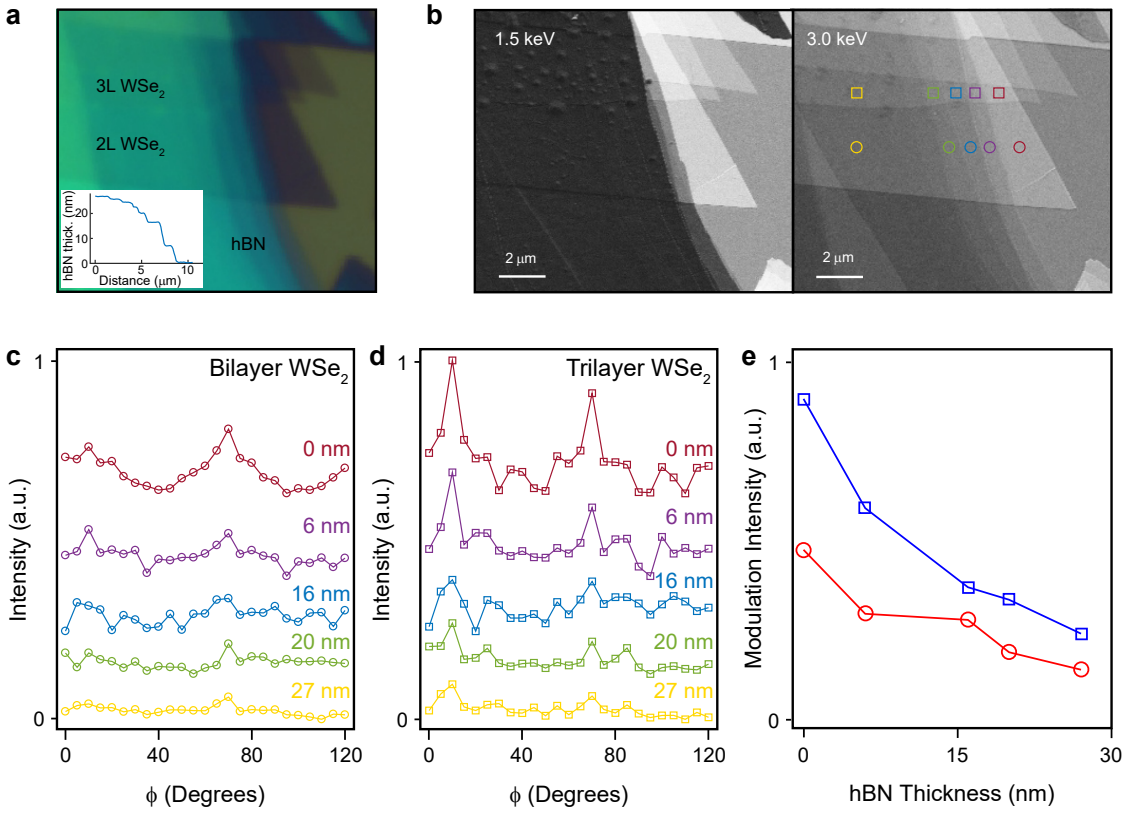


Figure 3.6: Depth dependence of SEM contrast a) Optical image of a naturally stepped WSe_2 flake stacked underneath a stepped hBN flake. Inset: AFM of stepped hBN thickness. **b**) SEM images of the sample in (**a**) at 1.5 keV (left) and 3 keV (right) primary acceleration voltage. Tuning the primary voltage alters the secondary electron energy spectrum, allowing for greater escape depth at higher acceleration voltage. For 1.5 keV, the escape depth is ∼10 nm, restricting collected secondary signal to the hBN. At 3 keV, the depth exceeds 30 nm, revealing the underlying stepped WSe_2 structure. **c-d**) Azimuthal angle dependence of secondary yield from bilayer (**c**) and trilayer (**d**) WSe_2 under varying thickness of hBN. The curves are normalised by dividing by the yield of bare silicon oxide underneath an equal thickness of hBN. **e**) RMS amplitude of the modulation signal for bi- and tri-layer WSe_2 (red and blue squares, respectively) as a function of encapsulating layer thickness. Our data indicate that domain contrast in bilayer TMDs is resolvable even through 20 nm of hBN.

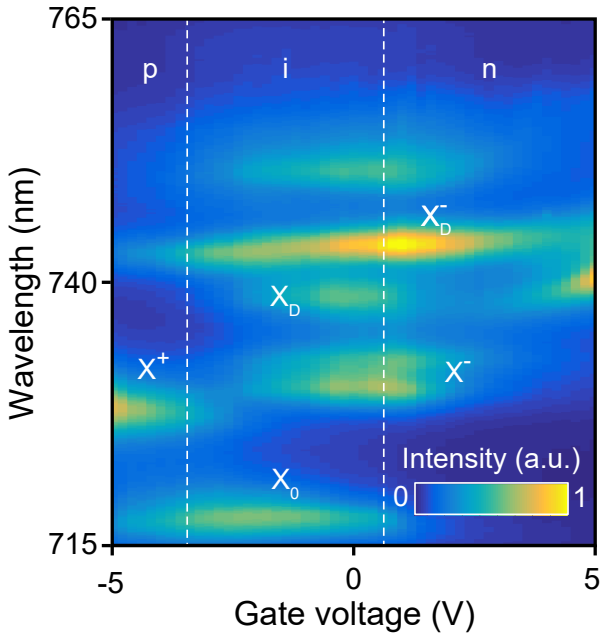


Figure 3.7: Compatibility of SEM technique with optoelectronic measurements Gate-dependent photoluminescence spectra from hBN-encapsulated monolayer WSe_2, showing strong emission from both bright (X_0) and dark (X_D) excitons, with narrow linewidths ($\sim$ 3 nm) and effective gate tunability. The latter is indicated by the appearance of charged excitons (X^+ and X^-).

with lower secondary yield (such as the device in Fig. 3.5) contrast mainly results from the difference in direct secondary generation in the bilayer. Hence, it is sufficient to model the secondary emission as proportional to the scattering probability in the bilayer in order to reconstruct an azimuthal dependence that closely resembles the experimental data (Fig. 3.5c). In this instance, a more complex azimuthal dependence than in Fig. 3.3d arises due to the 3-dimensional structure of WSe_2 along with a shallower, 40° polar angle. An important difference between TMDs and few-layer graphene (Figs. 3.3,3.4), is that the latter has a lower secondary yield than the SiO_2 substrate and therefore produces a "negative" signal, in the sense that enhanced channeling through the top layer and into the substrate increases overall detected secondary yield. In this scenario, we model the yield as proportional to the transmission probability and accurately recover the dominant features of ABA/ABC stacked few-layer graphene (Fig. 3.4c). Higher order features in between the dominant peaks are highly dependent on the particular scattering parameters used, as well as secondary emission from the graphite itself and are therefore not well represented in this simplified model.

3.6 Alternate imaging modes and applications

Below, we note a range of alternative settings under which the above imaging principles can obtain useful structural information.

3.6.1 Polar angle variation

The azimuthal angle dependence for graphene in Figs. 3.3 and 3.4 is collected at a polar angle of $\theta = 24°$ which approximately corresponds to a displacement of one carbon-carbon bond length per layer. For ABC stacking, this is the steepest angle at which maximal channeling can occur as it corresponds exactly to the inter-layer stacking offset. Owing to the symmetry of the lattice, however, equivalent behaviour (with a 60° phase shift in ϕ) is obtained for a displacement of two bond-lengths per layer, corresponding to $\theta \sim 41°$. This is demonstrated in Fig. 3.8, where we image the same graphene flake as in Fig. 3.4 at these two polar angles ($\theta = 24°, 41°$), using two different azimuthal angles ($\phi = 0°, 60°$). Under both polar angles, a high degree of channelling in ABC graphene is observed for one of the values of ϕ and not for the other. However, while the ABC region appears at $\phi = 60°$ for $\theta = 24°$, it appears for $\phi = 0°$ for $\theta = 41°$.

3.6.2 Monolayer TMD signal

Due to the three dimensional atomic structure of TMD layers, it is possible to measure the secondary yield modulation with azimuthal angle of a monolayer when imaging at a sufficiently shallow polar angle. Fig. 3.9a-c show SEM imaging, schematic and the azimuthal dependence for a WSe_2 monolayer on an SiO_2 substrate for a polar angle of 40°. These data indicate that SEM can be used to extract the lattice orientation of an exfoliated monolayer flake - information that is valuable for the assembly of twisted

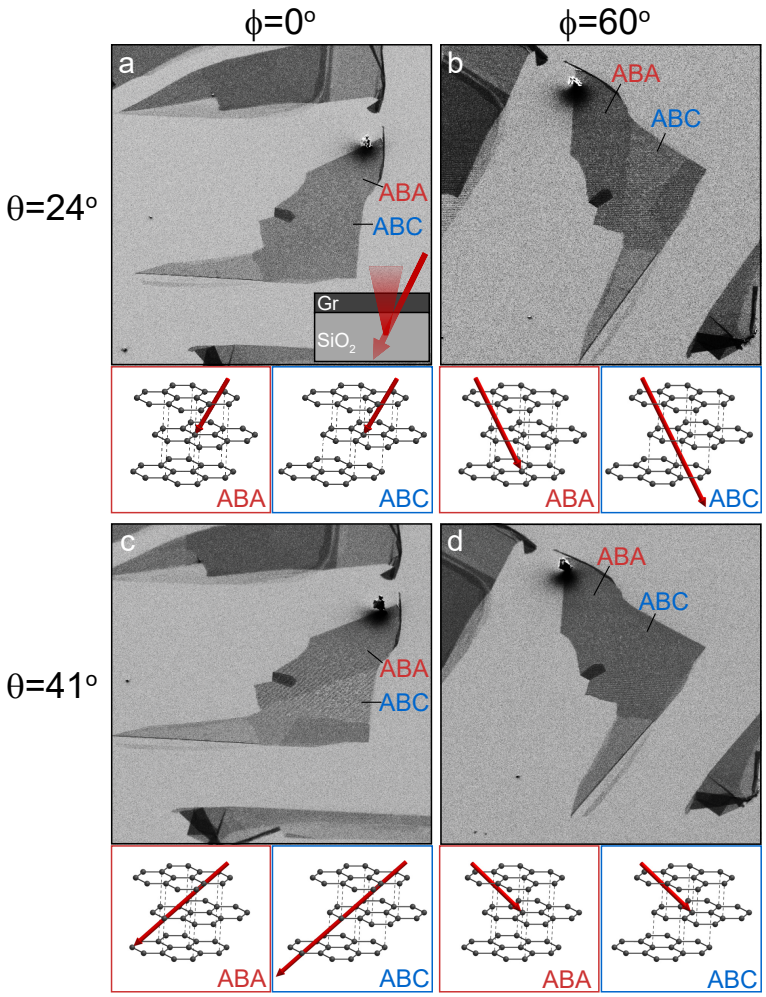


Figure 3.8: Polar angle variation. a-d) SEM images of few-layer graphene containing ABA- and ABC-stacked regions, at different polar ($\theta = 24°, 41°$) and azimuthal ($\phi = 0°, 60°$) angles. Schematics show channeling paths for ABA (red) and ABC (blue) stacking order at the different angle combinations. Since $\theta = 24(41)°$ corresponds to a shift of one (two) carbon-carbon bond lengths per layer, both polar angles enable complete channeling in the ABC region (causing bright SEM signal), but at different azimuthal angles.

heterobilayer devices.

3.6.3 Monolayer on bulk TMD signal

The ability to interrogate surface structure has the potential to elucidate more complex stacking orders, such as determining the relative rotation between a monolayer placed atop a bulk substrate. Fig. 3.10a shows an SEM image of a monolayer $MoSe_2$ flake stacked at a random angle on a thick multilayer $MoSe_2$ substrate (schematic in Fig. 3.10b). While the azimuthal rotation signal of the bulk (Fig. 3.10c) is relatively symmetric, the signal from the monolayer region displays a more complex pattern due to the partial channels between the monolayer and bulk. Taking the difference signal (Fig. 3.10d) reveals an asymmetric but roughly 60°-periodic structure. Further analysis may be able to use such a signal to determine the precise angular mismatch between the two layers.

3.6.4 Applications to CVD-grown materials

An interesting application of SEM imaging is rapid identification of layer stacking in CVD-grown 2D materials. We consider the ability to resolve a series of common stacking orders via the same computational methods used for WSe_2 AB/BA but applied to AA', AB, and 15° misaligned moiré bilayers. A clear contrast between different stacking orders was found for a polar angle of 24°, with AA' dominated by a 60°-periodic signal, compared to a large 120°-periodic component for AB. Computations for 15° moiré stacking were performed in a similar manner but averaging transmission over the full

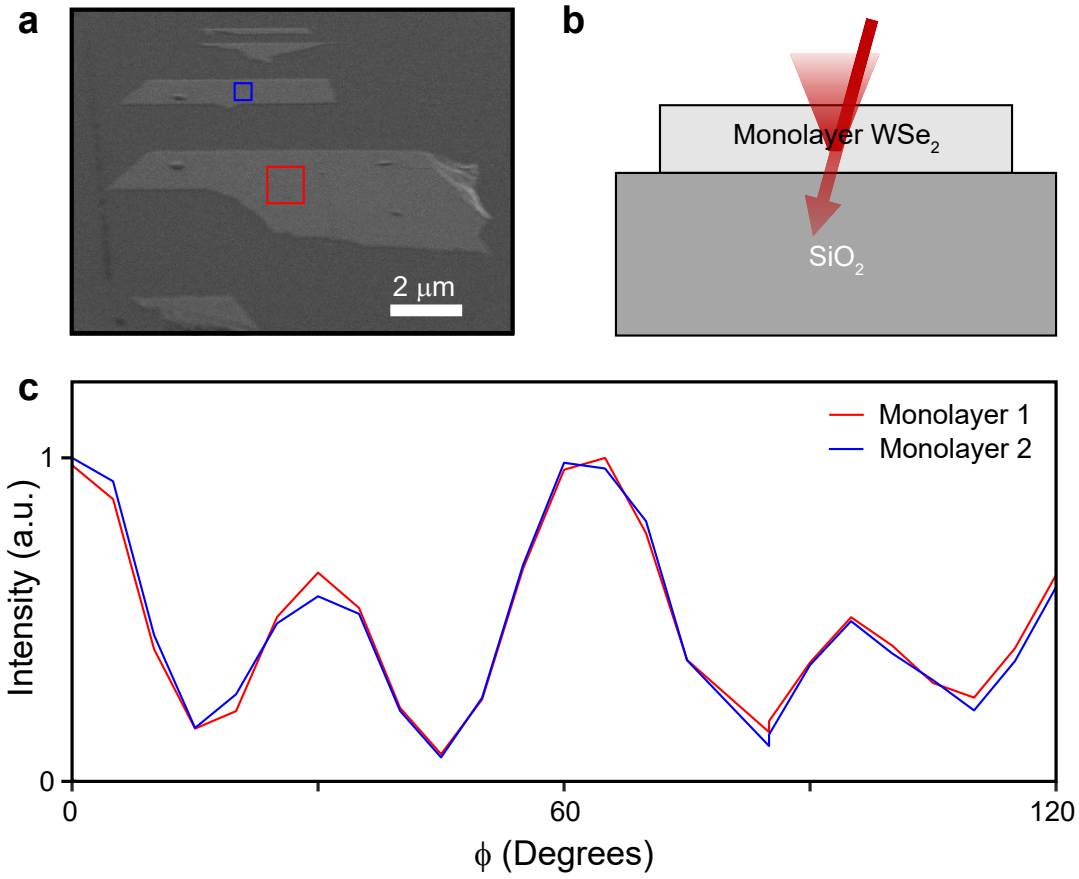


Figure 3.9: Imaging of monolayer TMD a) SEM image of monolayer WSe_2 flakes on SiO_2 substrate, using acceleration voltage of 1 keV and $\theta = 40°$. **b)** Schematic of secondary emission in this system, showing stronger secondary signal from the TMD, due to its higher atomic mass. **c)** Azimuthal dependence of SEM signal from two separate monolayer WSe_2 flakes, indicated by boxes in (**a**). Due to the 3D structure of TMDs, amplitude modulation can be observed even from monolayers.

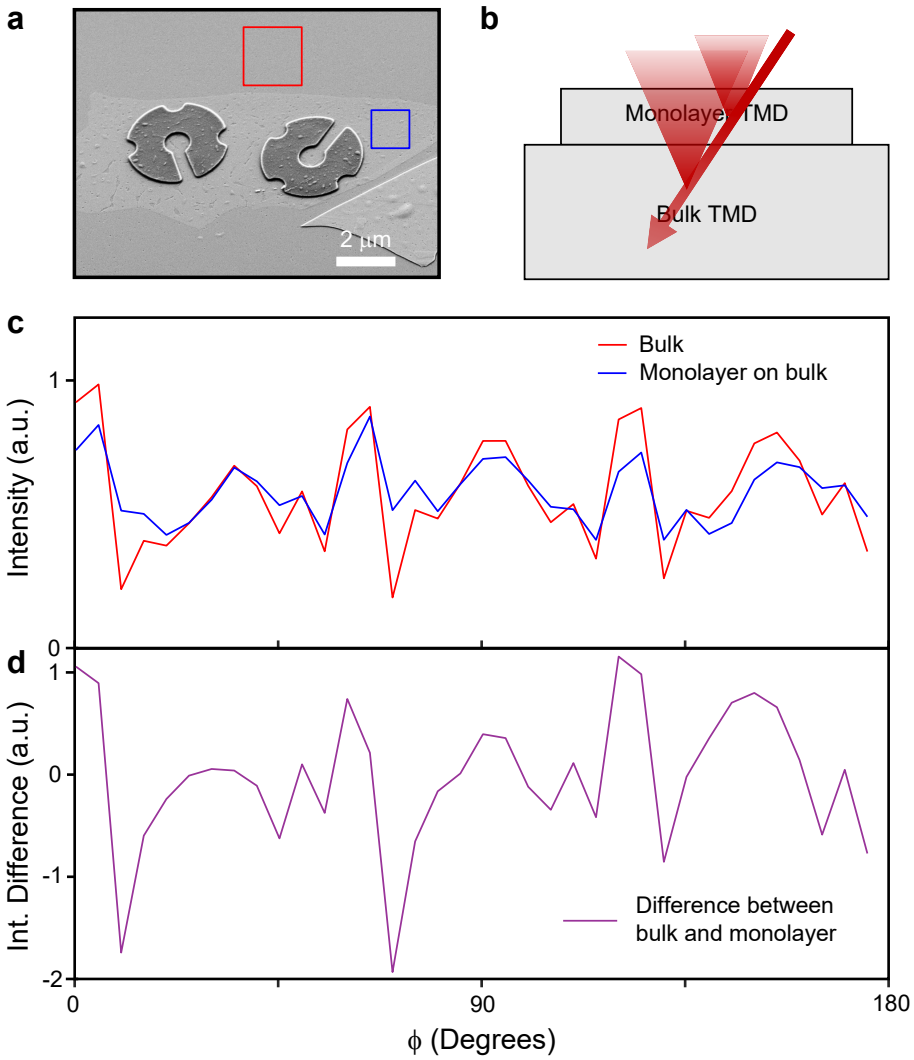


Figure 3.10: Imaging TMD monolayer on bulk **a**) SEM image of monolayer $MoSe_2$ placed on top of a thick $MoSe_2$ flake. **b**) Schematic of secondary generation from both the monolayer and bulk flake. **c**) Azimuthal dependence of SEM signal from monolayer on bulk (blue) and only the bulk (red), collected from the boxed regions in (**a**). The more complex structure of the former is due to the partial channels of the combined system. **d**) Difference between the two curves in (**c**).

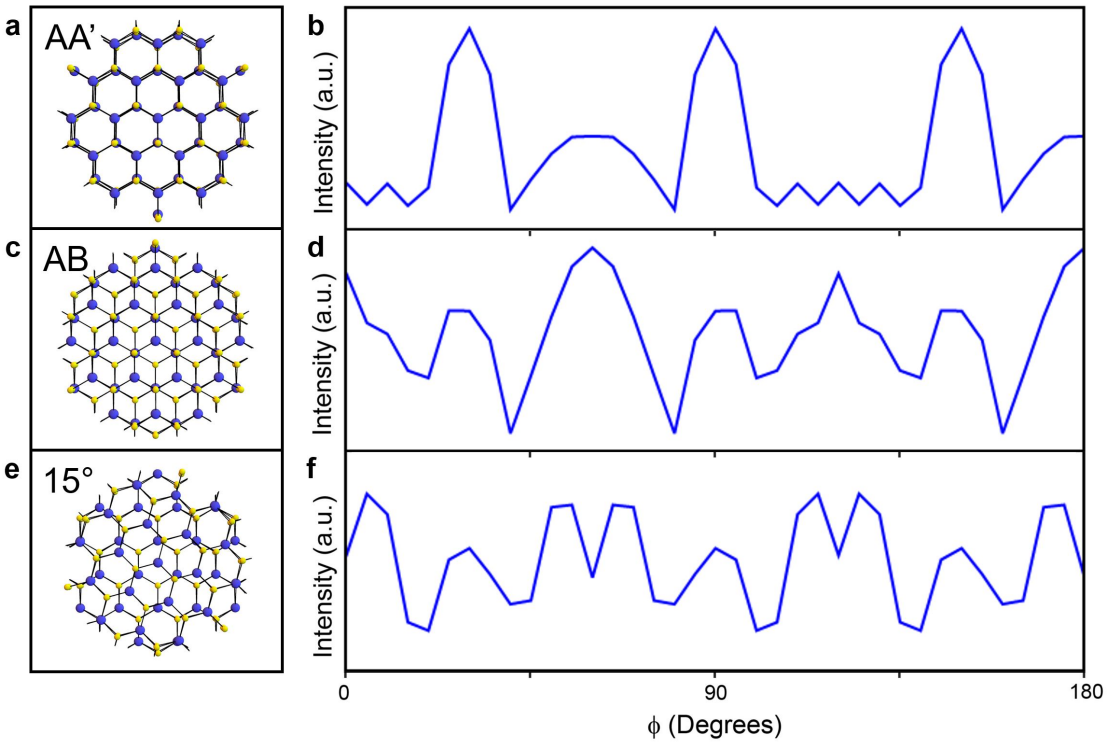


Figure 3.11: Modelling signal from TMD bilayer stackings Schematics of three of the stacking orders that can be found in CVD-grown TMD bilayers (**a,c,e**), with corresponding computed azimuthal dependence (**b,d,f**). Computational modelling is performed for WSe_2 at $\theta = 24°$.

superlattice cell rather than the monolayer lattice.

3.6.5 Surface structure in thick materials

Finally, we note a method to resolve surface-level structure by probing the material with a low energy beam (500 eV). Due to the rapid loss of secondary yield with increasing depth, the stacking orientation of the top two layers of bulk graphite can be readily measured, allowing for analysis of low-Z materials even over arbitrarily thick low-Z

substrate, such as bilayer graphene over thick hBN. To demonstrate the ability to differentiate stacking orders of graphene on top of materials with similar secondary yield (graphene, hBN), we image thick, stepped graphite flakes (Fig. 3.12a-c). By using a relatively small acceleration voltage (500 eV), the flake is sufficiently thick that the secondary yield depends on the stacking order of the surface layers, rather than the total thickness. In particular, the SEM signal depends on whether the top two layers are AB- or BA-stacked, and therefore alternates across steps of monotonically changing thickness (Fig. 3.12a). Similar to in Fig. 3.3d the two stacking orders exhibit 120° contrast oscillations with a 60° offset.

Similar measurements were conducted in a stepped multilayer $MoSe_2$ flake underneath a 10 nm layer of gold (Fig. 3.12d-f). Again, the SEM contrast depends on the stacking order of the top two layers, and thus alternates with the parity of the number of layers (Fig. 3.12d). In this case, the angular dependence (Fig. 3.12f) is more complex than in graphene, due to the 3D nature of the $MoSe_2$ layers, and also because the polar angle used here (30°) is not commensurate with the dominant channels in $MoSe_2$ so does not allow for maximal channeling

The stacking method by which vdW heterostructures can be assembled[21,26,61] allows for control and tuning of the stacking order in generic devices, where it can now be used as a versatile control knob. However, in most recent studies of exotic phases in twisted bilayers, the presence of the moiré superlattice was not directly imaged, but rather inferred indirectly, either from far-field optical and transport measurements

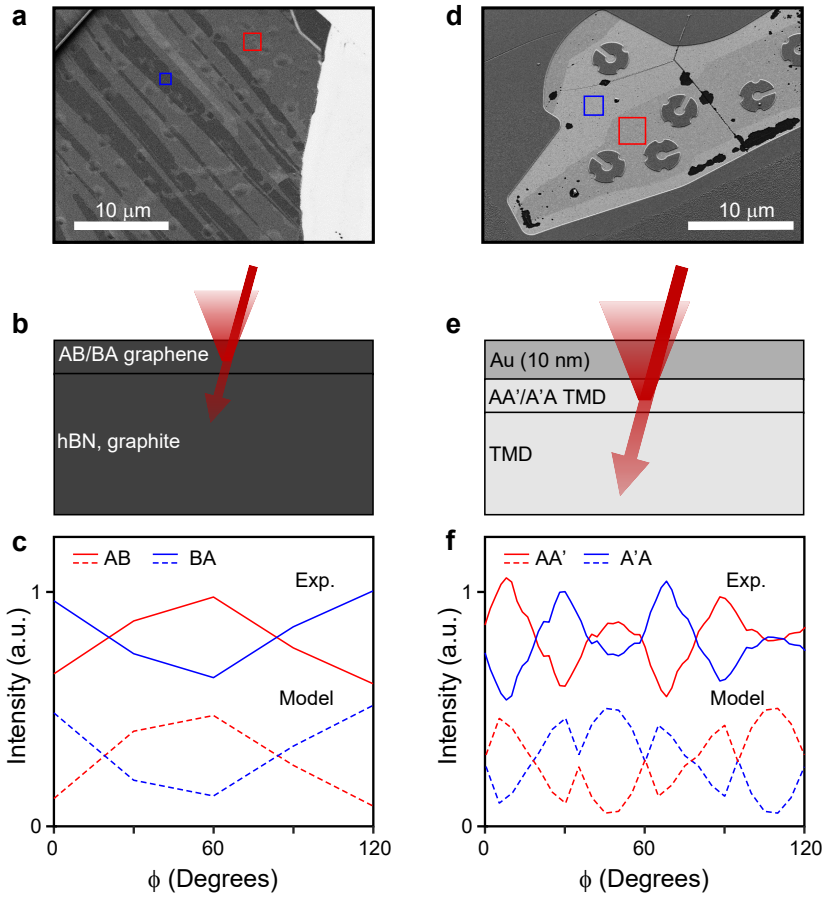


Figure 3.12: Imaging of stepped graphite and $MoSe_2$ a) SEM image of stepped graphite flake using acceleration voltage of 500 eV and $\theta = 24°$. Alternating contrast is observed as the top two layers change between AB and BA stacking across the steps. **b)** Schematic of secondary generation, highlighting the sensitivity to the stacking order of the top few layers, which enables imaging of AB/BA domains on top of thick low-Z materials such as graphite or hBN. **c)** Azimuthal angle dependence of SEM signal in regions with AB (red) and BA (blue) surface stacking (solid lines). Dashed lines show predictions of model presented in main text. **d-f)** Same as **(a-c)**, but in stepped $MoSe_2$ underneath 10 nm Au. The more complex azimuthal dependence (**f**) is due to the 3D nature of the $MoSe_2$ layers, and also because the polar angle used here (30°) does not allow for maximal channeling.

or from transmission electron microscopy (TEM) of other samples. Our observations demonstrate that channeling modulated secondary electron imaging can be used to directly image the atomic stacking orders of vdW heterostructures, including bilayer and multilayer graphene, and twisted bilayer TMDs. In all cases studied, simple computational modelling qualitatively predicts imaging contrast, enabling the systematic application of this technique to other materials and device structures. Compatible with complete, encapsulated and gated devices on standard substrates, our technique allows for direct correlation of atomic stacking order with optical and transport properties, as explored in the following section. Structural imaging demonstrated in this work can also become an important tool in the pursuit of large-area synthesis of high quality 2D materials through techniques such as chemical vapor deposition (CVD). The synthesis of bilayer TMDs, for instance, results in domains of differing stacking order, including 15° and 30° misaligned moiré[53]. The ability to directly resolve AB, BA, and AA' stacking orders from azimuthal periodicity and phase in SEM, along with the possibility of identifying smaller angles (Figs. 3.10,3.11) promises to provide structural information on as-grown samples without dedicated preparation for TEM, significantly accelerating the rate of process development for material synthesis. For these reasons, channeling modulated secondary electron imaging can be indispensable for 2D materials synthesis along with the further development of novel electronic and optical devices, including exotic emitter arrays, solid state quantum simulation platforms[66,79], and new quantum optical systems[3].

3.7 Correlating imaged moiré patterns with optical measurements

Because the SEM-based imaging technique is compatible with fully functional devices, we can now explore correlations between the moiré wavelength observed in SEM and the local optoelectronic properties. In particular, a second twisted WSe_2 device (D2) with analogous structure to D1 in Fig. 3.5 enables us to explore excitonic properties in the structural transition from the reconstructed to non-reconstructed regime. After co-aligning the SEM image with a map of photoluminescence (PL) intensity, we collect gate-dependent PL spectra from both sides of the device (boxed crosses in Fig. 3.13a), in locations where $\lambda_m < 10$ nm and $\lambda_m = 25 \pm 10$ nm (Figs. 3.13b and c, respectively). Due to the diffraction limited spot size and the aforementioned inhomogeneity, we note that each optical measurement probes a finite range of domain sizes, as indicated by the uncertainty range in λ_m.

In both spots, we observe two sets of emission features: the peaks near 1.5 eV are attributed to momentum indirect interlayer excitons based on their energy[69,84], whereas the higher energy peaks near 1.7 eV are attributed to K-valley momentum direct intralayer excitons, consistent with previous studies[84,70,23] and absorption measurements (Appendix C). While only one intralayer exciton peak (peak I) is observed on the left side of the device (Fig. 3.13b, $\lambda_m < 10$ nm), an additional higher energy peak (peak II) emerges in the right part (Fig. 3.13c, $\lambda_m = 25 \pm 10$ nm). Their splitting is 36 meV in the p-doped regime, where the two peaks are most pronounced, and decreases to 16 meV

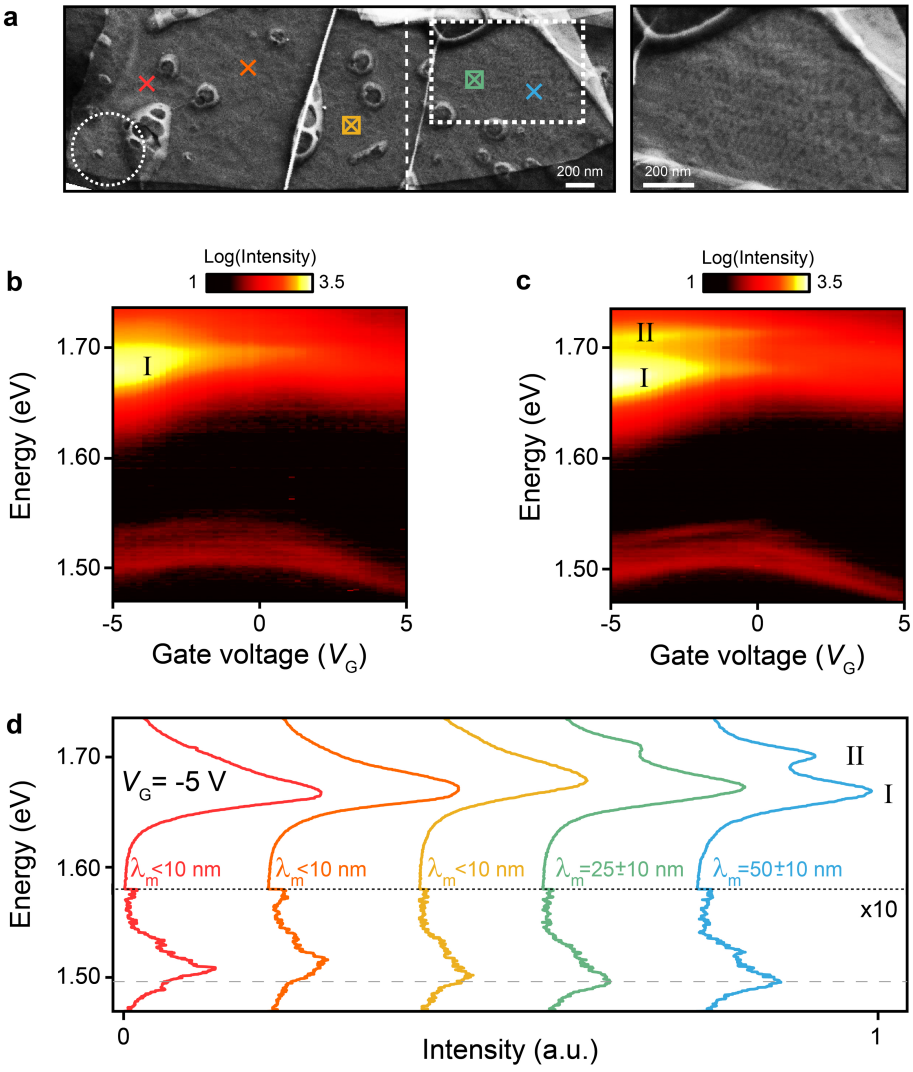


Figure 3.13: Correlating local superlattice structure and optical properties. **a**) Left: SEM image ($\theta = 40°$) of device D2, displaying reconstructed moiré pattern. λ_m increases from ¡10 nm to 60 nm from left to right. The moiré pattern is not visible left of the vertical dashed line. Dashed circle indicates optical beam spot size, crosses indicate beam spot centers. Right: Zoom-in of area indicated by dotted lines. **b**,**c**) Gate-dependent PL spectra collected from locations with $\lambda_m < 10$ nm (**b**) and $\lambda_m = 25 \pm 10$ nm (**c**), indicated by boxed crosses in (**a**). While the left region only exhibits one intralayer peak in the p-doped regime, the right (larger λ_m) region exhibits two peaks. **d**) Raw PL spectra collected from the locations marked with crosses in (**a**), at $V_G = -5$ V. The spectra are offset for clarity and the intensity is multiplied by 10 below 1.58 eV. The higher energy (type II) exciton peak emerges with increasing λ_m, and the interlayer exciton emission is blue-shifted for $\lambda_m < 10$ nm.

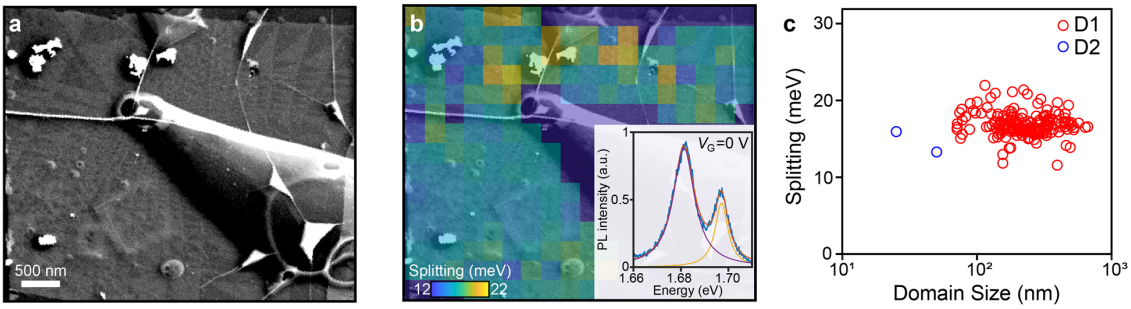


Figure 3.14: SEM correlation of PL peak splitting. a) Zoomed-out SEM image of D1 showing large (70-670 nm) reconstructed moiré domains in the entire twisted bilayer region. ($\theta = 40°$). **b**) Map of extracted exciton peak splitting overlaid with the SEM image from (**a**). Inset: Example PL spectrum (blue) with double Lorentzian fit. **c**) Correlation of SEM and PL shows that the peak splitting is independent of domain size over a 30-fold range. Red: device D1, blue: device D2.

in the intrinsic regime. Besides their resonance energies, the doping dependence of peak I and II is also distinct: with increasing hole doping, peak I broadens and intensifies strongly, while peak II is much less affected.

Inspecting more locations (crosses in Fig. 3.13a) at VG=-5 V, we find that a single dominant intralayer peak appears in all spots investigated on the left side of the device ($\lambda_m < 10$ nm), and that the higher energy peak only emerges with the larger λ_m in the right region (Fig. 3.13d), where the reconstructed moiré domains are observed. We also find that the interlayer exciton peak is blue-shifted in the left (small λ_m) region. This is not expected to be due to interlayer contamination, but rather the weaker interlayer coupling in the small-domain regime[69,84,44,48], which is also expected to cause less lattice reconstruction[86,11].

Previous studies of non-reconstructed moiré patterns in twisted heterobilayers[82,33,89,85],

as well as recent theoretical predictions for twisted homobilayer WSe_2[6], have considered exciton multiplets that arise from the moiré-induced mixing of exciton Bloch states $k = 0$ and $k = k_m$ (where k_m is a moiré wavevector), due to band folding and miniband formation. In that case, the splitting between the states, $E(k_m) - E(0) \sim \lambda_m^{-2}$, is strongly dependent on domain size[33,89,85,6]. In order to investigate whether this is the case for the two exciton states observed here, we turn to the smaller angle device D1, which has both larger moiré domains and a greater variation in their size (Fig. 3.14a). Importantly, this device exhibits the same two-peak structure as device D2 (Fig. 3.14b, inset), with a very similar splitting in both the p-doped (36 meV) and intrinsic (16 meV) regimes. By spatially correlating the PL signal with SEM imaging (Fig. 3.14b), we find that the splitting is independent of domain size over a 30-fold range (25-670 nm, Fig. 3.14c), in stark contrast to previous observations in TMD heterostructures[82,33]. Device D1 also exhibits more pronounced features in the n-doped regime, which shows very different behavior from the p-doped regime. While peak I red-shifts much more than peak II at the onset of the p-doped regime ($E_h^I = 20$ meV, $E_h^{II} \sim 0$ meV), peak II exhibits a larger red-shift in the n-doped regime ($E_e^{II} = 16$ meV, $E_e^I = 11$ meV; green arrows in Fig. 3.15a), thus reducing the splitting to only 10 meV.

In order to further explore the origin of the two exciton peaks, we conduct polarization-resolved photoluminescence spectroscopy. By illuminating with linearly polarized light, we excite a superposition of K and K' valley excitons (excited by the superposition of σ^+ and σ^- photons), and subsequently measure the quantum coherence between

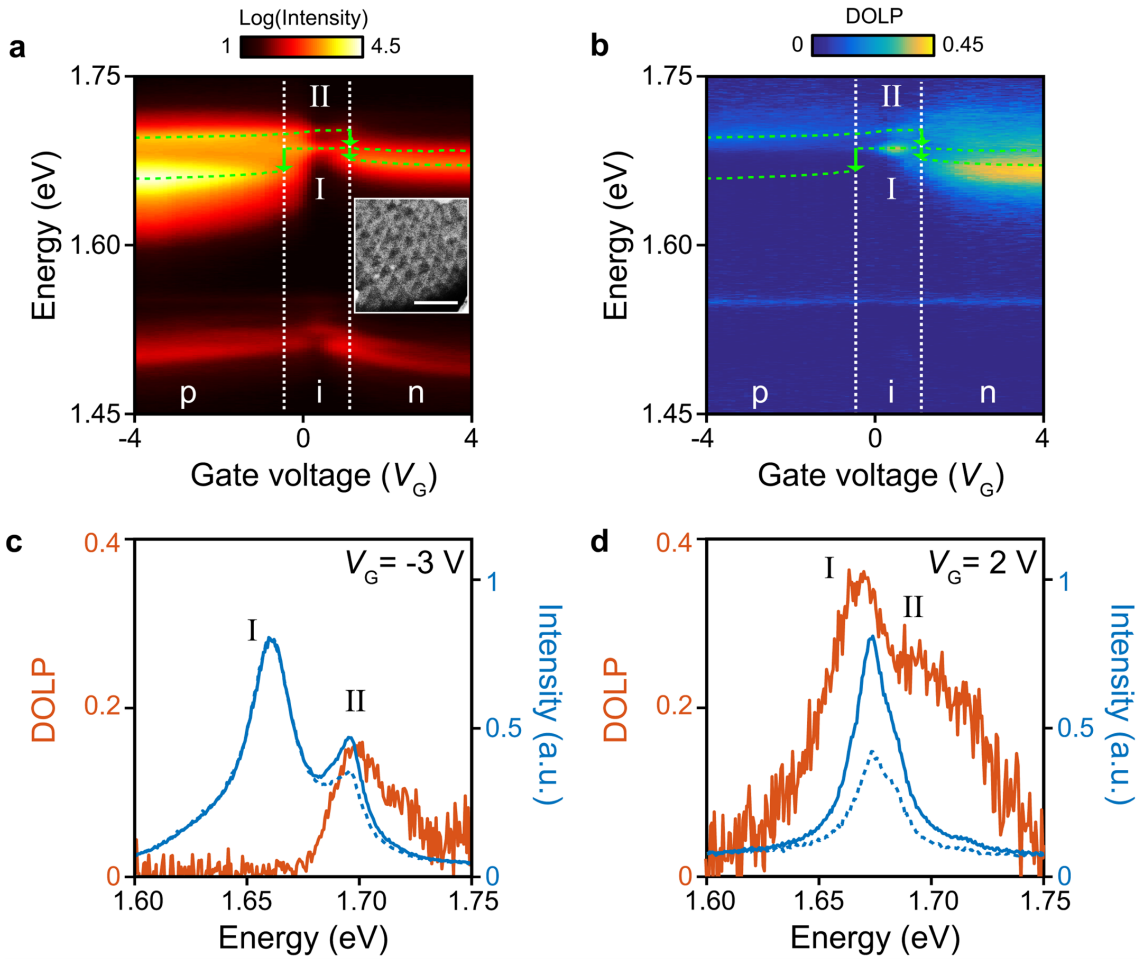


Figure 3.15: Valley coherence of the two exciton species. a) Gate-dependent PL spectra from device D1. Green dashed lines show fitted peak positions. Inset: SEM image of measured spot ($\theta = 40°$). Scale bar: 200 nm. **b**) Gate-dependent DOLP, showing that type I excitons have nearly zero DOLP in the p-doped regime. **c**,**d**) Co- and cross-polarized PL (blue solid and dashed curves), and corresponding DOLP (orange) at $V_G = -3$ V (**c**) and $V_G = 2$ V (**d**).

these valley states by comparing the parallel and perpendicular emission components[34]. Importantly, we note that this measurement is very distinct from circularly polarized PL measurements[10], which probe the valley depolarization rate, not the quantum coherence[34,29]. Defining the degree of linear polarization, $DOLP = (I_{\parallel} - I_{\perp})/(I_{\parallel} + I_{\perp}), where I_{(\parallel(\perp)}$ is the intensity of emission with parallel (perpendicular) polarization, we find that the two exciton species have very distinct coherence properties. The lower-energy (type I) exciton has almost zero DOLP in the p-doped regime, while the higher-energy (type II) exciton exhibits a DOLP of up to 18% (Fig. 3.15b and c). When entering the neutral regime, the DOLP of the type I exciton increases strongly and exceeds that of type II, which exhibits much less change. In the n-doped regime, the DOLP of both exciton types is found to be even higher, reaching 44% (Fig. 3.15b and d).

3.8 Properties of the reconstructed superlattice

We here show that all our observations are consistent with two spatially alternating, individually controllable exciton species in the reconstructed superlattice. Our model is based on the local band structure differences in the observed AB- and BA-stacked domains of t-WSe_2/WSe_2. Since AB and BA domains are vertical mirror images of each other, we refer to the top layer in BA domains and the equivalent bottom layer in AB domains as type I locations (Fig. 3.16a, maroon squares), and the opposite

locations as type II (Fig. 3.16a, orange squares). We conduct density functional theory calculations which show that the global valence band maximum (VBM) at the K-point is $\Delta E_{\mathrm{VB}} = 73$ meV higher in type II locations than in type I locations (Fig. 3.16b). Conversely, the local conduction band minimum at the K-point is $\Delta E_{\mathrm{CB}} = 60$ meV higher in type I locations. These observations in essence reflect the different electronic environment of the respective layers. In addition, and consistent with previous studies, our DFT calculations indicate that the wavefunctions at the K-point are localized in the individual layers (insets, Fig. 3.16b)[10].

These results give rise to two effects that split the energies of type I and type II excitons in the namesake locations. First, the two locations are expected to possess different optical band gaps, causing excitons in type II locations to be higher in energy by $\Delta E_0 = \Delta E_{\mathrm{VB}} - \Delta E_{\mathrm{CB}} = 13$ meV in the intrinsic regime (Fig. 3.16c). This is in very good agreement with our observations for all devices. Importantly, since $\Delta E_0 < \max(\Delta E_{\mathrm{VB}}, \Delta E_{\mathrm{CB}})$, our results suggest a staggered band gap at the domain boundaries. Second, in the doped regimes, the two exciton types are expected to have an additional energy difference because of different interactions[50] with the additional charges (Fig. 3.16d). In particular, our calculations predict that type I locations should be preferentially p-doped due to their higher VBM (Fig. 3.16b)[90,41]. Thus, it is indeed expected that type I excitons can bind strongly to a nearby hole to form charged excitons with reduced energy, while type II excitons only interact weakly with the holes in the other layer, as found in our measurements (Figs. 3.13c, 3.15a). In the n-doped

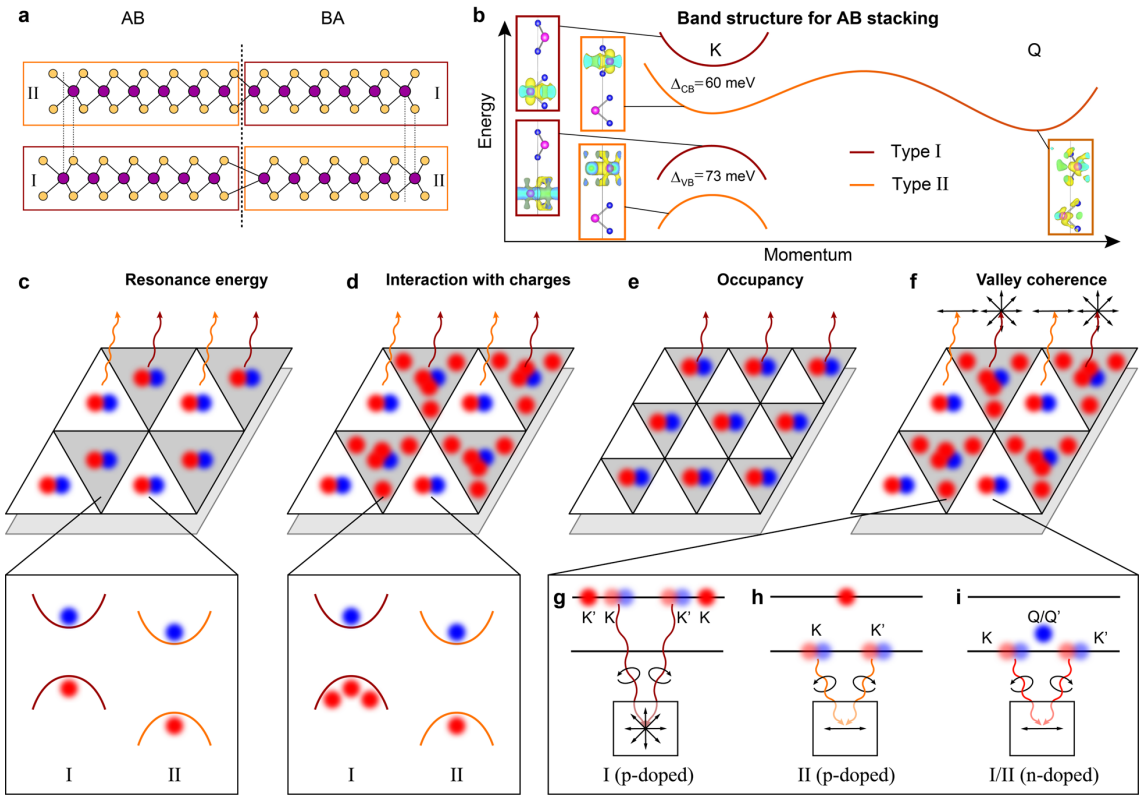


Figure 3.16: Periodic exciton and doping landscape in reconstructed superlattice. **a**) Side view of AB and BA domains. Maroon and orange boxes indicate type I and II locations, respectively. **b**) Band structure schematic and wavefunction distribution at important points in k-space. **c**-**f**) Schematic of alternating properties in the two-dimensional triangular exciton array. For clarity, only excitons in the top layer are shown. **c**) Excitons have higher energies in type II locations due to larger optical band gap. **d**) Type I excitons are preferentially p-doped due to higher VBM. **e**) Only the type I exciton is observed in the small-domain regime due to relaxation of the higher energy exciton. **f**) The two alternating exciton species also have different valley coherence properties. **g**-**i**) Schematics of K/K' exciton recombination. Black horizontal lines indicate top and bottom layer. **g**) Since the resident hole must be in the opposite valley of the type I exciton, it becomes correlated with the photon and breaks coherence. **h**) For the type II exciton, the resident hole is in a different layer and carries no information about the exciton valley, allowing for non-zero DOLP. **i**) DOLP is non-zero for both exciton types in the n-doped regime, because the electron is in a different valley (Q/Q') than the exciton (K/K').

regime, our calculations indicate that the induced carriers are less layer-localized than in the p-doped regime, because the global conduction band minimum is at the Q-point instead of the K-point (Fig. 3.16b)[47,58]. Both exciton species are therefore expected to interact with the electrons, consistent with our observations in Fig. 3.15a. The higher energy (type II) peak is only expected to be observed if the excitons are unable to relax to a lower energy state in a different location type before recombining ($\tau_X \sim 1$ ps, Fig. 3.16e)[3,7]. While interlayer tunneling is symmetry forbidden at the K-point in 3R (AB/BA-stacked) bilayers[90,65], moving laterally to an oppositely stacked domain within the same layer is a faster process[43,7], especially for small domains (Fig. 3.16e). The estimated exciton diffusion length in our system is 10-100 nm (Appendix C), consistent with the observed disappearance of the higher energy peak as the domains decrease from $\lambda_m = 50$ nm to $\lambda_m < 10$ nm. We note that for very small domains, such as in the left side of device D2, additional effects may appear due to reduced effects of lattice reconstruction[82,33,86,93,11]. Finally, our model also explains why the two species have such different coherence properties (Fig. 3.16f). In the case of type I excitons in the p-doped regime, the additional hole is in the same layer as the exciton and must therefore be in the opposite valley due to the Pauli exclusion principle (Fig. 3.16g). Thus, the exciton (X) and hole (h) form an entangled state $|K\rangle_X\ |K'\rangle_h \pm |K'\rangle_X\ |K\rangle_h$. Since $|K\rangle_h$ and $|K'\rangle_X$ are orthogonal, linearly polarized emission is not possible[30], as observed in our experiment. For type II excitons, on the other hand, the additional holes are in the opposite layer compared to the exciton and thus carry no information about its

valley, allowing for higher coherence than that of type I (Fig. 3.16h)[34,30]. In the intrinsic regime, there are no additional holes, and the DOLP of both exciton types is therefore non-zero. Finally, in the n-doped regime, the K-K exciton and resident Q-valley electron are in different valleys. Thus, there is no Pauli exclusion principle at play, allowing for non-zero DOLP regardless of which layer the exciton resides in (Fig. 3.16i).

3.9 Conclusion

We have demonstrated that the SEM-based technique can be used to directly image stacking domains in bi- and few-layer graphene, and importantly, moiré patterns in twisted vdW heterostructures. This versatile technique, which can be applied to a wide range of 2D material based systems, can also become an important tool in the pursuit of large-area synthesis of high quality 2D materials through techniques such as chemical vapor deposition (CVD)[53]. The ability to directly resolve angle-misalignment between subsequently grown layers, as well as AB, BA, and AA' stacking orders, can provide structural information on as-grown samples without dedicated preparation for TEM, thus significantly accelerating the rate of process development for material synthesis. Crucially, we have demonstrated that our technique can be used to correlate local moiré structure with optical properties. Our observations can be understood as resulting from the emergence of two spatially alternating exciton species in the reconstructed moiré superlattice, with distinct gate tunability and valley coherence properties. We note that

although the bilayer system as a whole is expected to exhibit the same optical response in AB and BA domains, the two layers can be treated independently due to strongly suppressed interlayer tunneling in AB/BA domains at the K-point[90]. Furthermore, a modest vertical electric field (~ 0.1 V/nm) can lift the degeneracy in AB/BA optical response in the doped regimes. Our experiments therefore indicate that this system can be an attractive solid-state platform for engineering arrays of emitters, and open the door to new quantum optoelectronic applications[64,90,3,94]. In particular, the large range of attainable moiré wavelengths in homobilayers, combined with electrostatic control of the individual regions, can be used to develop new types of moiré-based metasurfaces[3]. Specifically, we have shown that the splitting between type I and II excitons can be electrostatically tuned from 36 meV in the p-doped regime to 10 meV in the n-doped regime. Moreover, the tunable quantum coherence properties demonstrated in our system can enable controlled, spatially patterned entangled states of light, essential for the development of quantum metasurfaces[3]. One particularly intriguing direction involves realizing one-dimensional localized exciton states, where the electron and hole reside at opposite sides of the sharp moiré domain boundaries in twisted homobilayers. These have been predicted to exhibit large in-plane dipole moments, as well as quantum confinement effects in 10-100 nm sized triangles[45]. Besides featuring triangular domains with ideal band alignment and length scales, our platform provides regular arrays of such systems, which could permit tunable interactions. This may be utilized for engineering strongly correlated states with strong optical response, potentially enabling the realization of

interacting excitons for applications such as quantum nonlinear optics[3].

4

Conclusion

I have heard it said that condensed matter physics is a vast collection of unique cases. While an atom can be isolated and have increasingly minuscule slices of the interactions between its nucleus and electrons teased out, condensed matter systems have so much potential for both exciting and entirely unwanted emergent properties that no two devices made in lab will ever be quite the same. Indeed, that motif carries through much of the work described above. The efforts in chapter 1 were complicated by some entirely mundane defects, but the study of those devices also yielded an observation of a wholly unexpected and unexplained effect, the study of which comprises chapter 2. The SEM

imaging technique outlined in chapter 3, itself an entirely accidental discovery further reinforces that point that 2D material devices often have far more complexity than their designers expect. The variation in twist angle and domain periodicity observed in imaged devices highlights that while the assembly process was configured for a particular angle, the resulting device can deviate significantly for that intent. In the absence of imaging, it would have been tempting to attribute the effects seen under optical measurements to moire band structures, but finding peak position largely independent on domain periodicity made that interpretation untenable. These results inspire methodological caution in interpreting any observations, as with so many possible phenomena at play, the existence of a consistent theoretical picture does not imply the uniqueness or accuracy of that picture. In return, the breadth of possibilities means a mundane attempt to image metal deposition quality can turn into a new imaging technique and help build a stronger understanding of 2D material physics.

A

Supporting Material for Chapter 1

A.1 Experimental Methods

A.1.1 Device fabrication

Flakes of hBN, $MoSe_2$ were first mechanically exfoliated from bulk crystals onto clean Si/SiO_2 wafers (Si substrates with 285 nm thermally grown SiO_2). monolayer $MoSe_2$ were identified optically, while the thickness of hBN flakes was determined with atomic force microscopy. Next, the heterostructures were assembled with the dry-transfer method and deposited onto Si/285 nm SiO_2 wafers with pre-patterened platinum gates

and contacts. Gate and electrical contacts were defined with e-beam lithography and deposited through thermal evaporation.

A.1.2 Measurements

Photoluminescence measurements were conducted in a 4 K cryostat (Montana Instruments), using a custom-built 4f confocal setup with a 0.75 NA objective and a 660 nm Thorlabs diode laser. Galvo mirrors were used to control the co-aligned excitation and collection position on the sample, and electrostatic gating was performed with Keithley sourcemeters. Time resolved measurements were performed with a PicoHarp 300.

B

Supporting Material for Chapter 2

B.1 Experimental Methods

Transport and optical characterisation is performed at 6 K in a closed cycle cryostat with optical access via a free-space confocal system with a 0.75 NA objective. For many experiments, two individually steerable beam paths are used to concurrently excite different regions of the nanofabricated device structures at independently varying intensity and wavelength. A temperature-stabilised CW 660nm laser diode is employed for off-resonant excitation, while wavelength dependent studies are performed with a

tunable CW Ti:sapphire laser source. Unless explicitly stated otherwise, all measurements are performed with contacts to the TMD at 0 V for ease of interpretation of local gate voltage. Heterostructures are assembled from exfoliated flakes using a dry-transfer technique with a PC-PDMS polymer stamp, deposited on Si/285 nm SiO_2 chips, and characterised with AFM to determine layer thicknesses. Twist angle between the hBN and TMD layers is random in all devices. Contacts and metal gates, where present, are patterned using electron-beam lithography followed by thermal evaporation. Numerous devices are employed in this work, with their key structural properties provided in Section B.2.

B.2 Device structures

Below is a table of the properties of all device structures used in this thesis. Photocurrent was also observed in numerous other similar devices that are not discussed due to redundancy.

Device	TMD	Top hBN	Bottom hBN	Contacts	Top gate	Bottom gate
A	$MoSe_2$	55 nm	90 nm	Pt	-	6 nm Au
B	$MoSe_2/WSe_2$	60 nm	50 nm	Pt	6 nm Au	6 nm Au
C	$MoSe_2$	27 nm	3 nm	Cr/Au	-	3 nm graphite
D	WSe_2	50 nm	70 nm	Pt	-	6 nm Au
E	$MoSe_2$	O(50 nm)	O(50 nm)	Pt	-	Si/285 nm SiO_2
F	WSe_2	O(40 nm)	12 nm	Pt	-	3 nm graphite

B.3 DFT Methods

We carry out density functional theory (DFT) calculations in VASP[42] using hybrid functionals (HSE06[31]). For the hBN layer, we use boron potentials with 3 valence electrons and nitrogen potentials with 5 valence electrons. For the transition metal dichalcogenide (TMD) layer, we use metal potentials with 14 valence electrons and selenium potentials with 6 valence electrons. Van der waals forces between layers are accounted for using the DFT-D3 method of Grimme[27]. Individual monolayers were relaxed with a 6x6x1 Γ-centered k-point mesh at a variety of in-plane lattice constants to obtain the following optimized monolayer lattice constants: $a_{hBN} = 2.492\mathring{A}, a_{MoSe_2} = 3.26\mathring{A}, a_{WSe_2} = 3.252\mathring{A}$. We construct bilayers with a supercell consisting of 7 TMD unit cells on top of 12 hBN unit cells, with the hBN strained to match the TMD layer. In the

$MoSe_2$/hBN bilayer, the hBN is compressively strained by 0.09%, and in the WSe_2/hBN bilayer, the hBN is compressively strained by 0.33%. In both systems, the layers are twisted with a 10.89° angle between them. The density of states is computed with spin-orbit coupling on a 12x12x1 Γ-centered k-point mesh. In all cases, the out-of-plane lattice constant is $30\mathring{A}$, resulting in approximately $23\mathring{A}$ of vacuum in each case. To construct the smooth density of states plots in Figure 2.5a, b, each state is given a gaussian profile in energy with standard deviation $\sigma = 0.08$, and we use energy bins of width 10 meV. The hybridization of a given state is determined by extracting the fraction of the wavefunction localized in the TMD layer (x) and plugging it into a parabolic function $h(x) = -4x(x-1)$, where $x \in [0, 1]$. Doping was not accounted for in our first-principles calculations. Because the experiments showed that the exciton and trion energies did not vary significantly with doping, we judged that band renormalization due to doping does not play a major role in the physics of the hBN/TMD interface (though it does affect exciton generation under narrow on-resonant excitation as in Fig B.9). Furthermore, we use the DFT calculations qualitatively rather than quantitatively in this study. All quantitative estimates come from the kinetic model and the Fowler-Nordheim model fitting the experimental data.

The 10.89^o twisted supercell was chosen not because of any significance of this angle, but to minimize strain in the first-principles calculations while still being small enough to avoid excessive computational expense. The relative twist angle between hBN and TMD was not controlled during the experimental fabrication process, so samples likely

exist at a variety of angles, and all exhibit the same photocurrent behavior. This is consistent with our DFT calculations: in addition to the 10.89^o calculations, we also computed the layer-hybridized density of states for hBN/$MoSe_2$ and hBN/WSe_2 bilayers with a relative rotation angle of 19.1^o, and the results are qualitatively the same. There are more hybridized states available to holes excited by a h^+-X^0 Auger process in the $MoSe_2$ system than in the WSe_2 system (See Fig. B.1). There are differences in band energies computed with DFT for the two different angles, but these likely arise from the different amounts of strain in the computation supercells. This strain is introduced to make the computations tractable and likely would not be present to a comparable extent in the real heterostructure.

To see that the strain does not significantly affect band morphology in the bilayers, we show in Fig. B.2 the bands for the 19.1^o bilayers with the hBN strained/TMD unstrained (a,b), and then with the hBN unstrained/TMD strained (c,d). While the band energies are somewhat altered with strain, the band morphologies remain very similar.

B.4 Kinetic Model and Doping-dependent QE fits

To better understand the photocurrent in these systems, we derive an expression for the photocurrent (quantum efficiency) from a set of kinetic equations that describes particles in the TMD layer. We first write the expression for the neutral excitons (n_X) in the TMD:

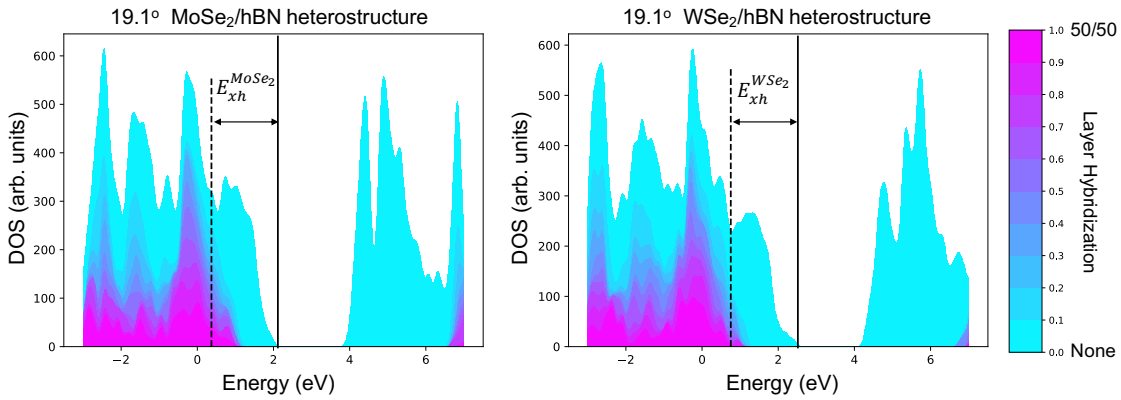


Figure B.1: Hybridized Density of States (DOS) for 19.1^o twisted supercell The 19.1^o twisted supercell contains 4 unit cells of TMD and 7 unit cells of hBN. In these calculations, the TMD is left unstrained and the hBN layer is compressively strained by 1.1% for the $MoSe_2$ system and by 1.4% for the WSe_2 system. All other calculation parameters are the same as those listed for the 10.89^o twisted supercell. In agreement with the experiments, which show that the photocurrent behavior persists across samples with uncontrolled twist angles, the relative differences in DOS between the two systems shown here are qualitatively the same as the differences between the $MoSe_2$ and WSe_2 systems in the 10.89^o supercell.

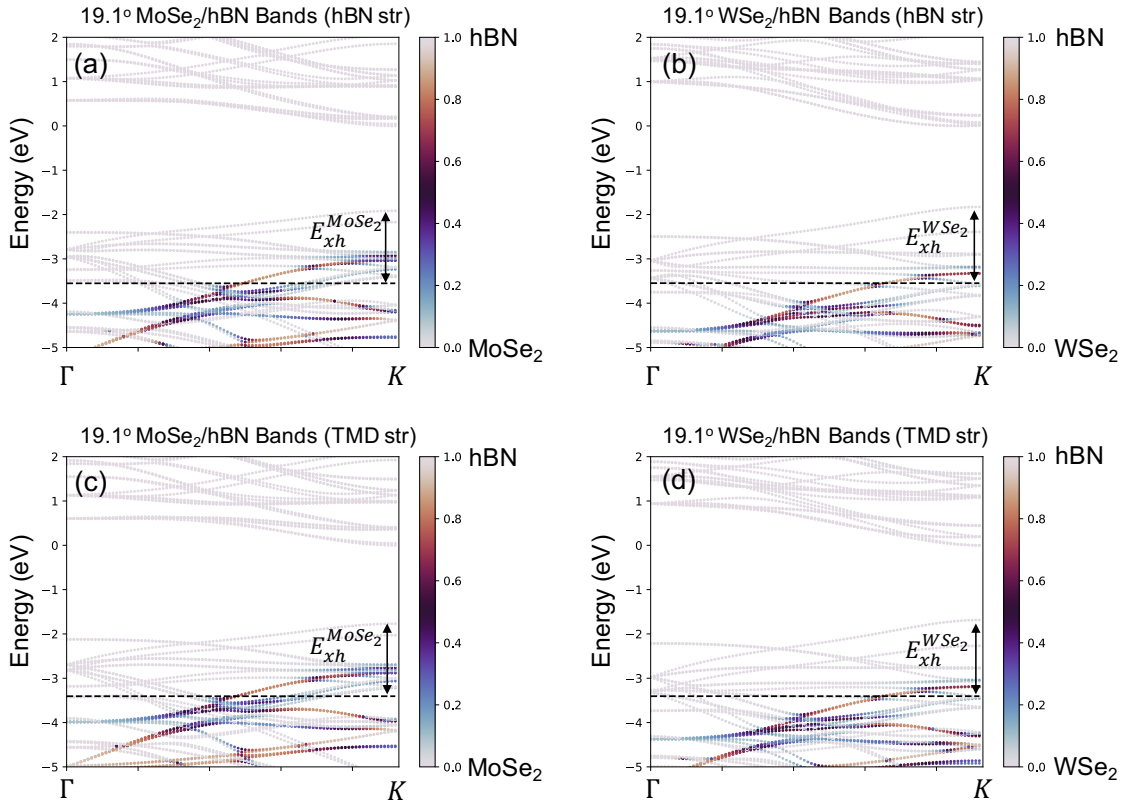


Figure B.2: Effect of strain on band structures for 19.1° twisted supercell Band structures for TMD/hBN bilayers with a 19.1^{o} twist with **a,b**) the hBN layer compressively strained by 1.1% and 1.4%, respectively and **c,d**) the TMD layer under tensile strain of 1.1% and 1.4%, respectively. Although the band energies change noticably with strain, the change in band morphologies with strain is minimal. Dashed lines mark the neutral exciton energy measured from the valence band maximum. Layer-polarized bands are colored light gray, while bands of any other color are layer-hybridized to the degree indicated by the color bar.

$$\frac{\partial n_X}{\partial t} = g_{eh} - \frac{n_X}{\tau} - \frac{1}{\tau_A^B} n_X^2 - h_g \frac{n_X}{\tau_A^T} \tag{B.1}$$

where g_{eh} is the electron-hole generation rate, which is proportional to the laser power. τ^{-1} is a time constant describing the radiative and non-radiative (but not Auger) recombination of excitons: $\tau^{-1} = \tau_r^{-1} + \tau_{nr}^{-1}$. h_g is the number of ground state holes, τ_A^T is the time constant describing Auger recombination of excitons, and τ_A^B is the time constant for exciton-exciton annihilation. Our experiments are carried out in the low-pumping regime, as shown by measurements of current that are linear in laser power (Fig 2.2c), and in this regime, we can ignore the quadratic n_X term. We assume the low-pumping limit in all the equations that follow. If we also work in the steady state limit, we obtain $n_X = g_{eh}\tau_d$, where $1/\tau_d = 1/\tau + h_g/\tau_A^T$.

The equation describing the excited holes, h_e is as follows:

$$\frac{\partial h_e}{\partial t} = h_g \frac{n_X}{\tau_A^T} - \frac{h_e}{\tau_{tun}} - \frac{h_e}{\tau_{ter}} \tag{B.2}$$

where τ_{ter} is the time it takes an excited hole to thermalize, and τ_{tun} is the time it takes an excited hole to tunnel into the hBN. Finally, the expression for the ground state holes in the system is

$$\frac{\partial h_g}{\partial t} = \frac{h_e}{\tau_{ter}} - h_g \frac{n_X}{\tau_A^T} + \frac{h_e}{\tau_{tun}} \tag{B.3}$$

The h_e/τ_{tun} term represents the current of ground state holes flowing into the TMD layer. It exactly balances the expression for excited holes tunneling out of the TMD because we assume we are operating in steady state. If we solve equation B.3 in the steady state, we obtain the expression $h_e = h_g n_X \tau_{ex}/\tau_A^T$, where $1/\tau_{ex} = 1/\tau_{ter} + 1/\tau_{tun}$.

Since we are interested in the photocurrent, we write an expression for the quantum efficiency (QE), which is roughly the current divided by laser power:

$$QE = \frac{h_e}{\tau_{tun} g_{eh}} \tag{B.4}$$

and using our expressions for n_X in the steady state, low-pumping limit and h_e in the steady state limit, we obtain the following expression:

$$QE = \frac{h_g}{(\tau_{tun}/\tau_{ter} + 1)(\tau_A^T/\tau + h_g)} \tag{B.5}$$

This expression for quantum efficiency is dependent only on the hole-doping in the TMD, so we can use it to fit measurements of photocurrent as a function of doping. These fits are shown in Figs. 2.5c,d, along with the extracted approximate values of τ_{tun}/τ_{ter} and τ_A^T/τ for each system. While the expression in Equation B.5 doesn't account for all the features in the QE data, it does capture an important difference between WSe_2 and $MoSe_2$: the ratio τ_A^T/τ is the same order of magnitude in the two systems, but the ratio τ_{tun}/τ_{ter} is two orders of magnitude larger in the WSe_2 system as in the $MoSe_2$ system. Thermalization of excited holes is more efficient than tunneling in both systems, but in

the WSe_2 system, thermalization is *much* more efficient, which is consistent with the larger amounts of photocurrent measured in the $MoSe_2$ system.

B.5 Dissociation Doping Power Dependence

Several other experiments were conducted to evaluate the impact of photodoping in $MoSe_2$ devices. In Fig B.3, we consider the dependence of the spatial map of photocurrent on the power of the confocally scanned excitation laser. We note that at increasing power, appreciable photocurrent is only observed while the gate edges are illuminated, indicating that photodoping is the dominant doping mechanism at high optical power. At very low power (Fig. B.3c) we see roughly uniform current from the entire device area, suggesting that a weak hole doping mechanism exists to replenish holes in the absence of photodoping.

We explore the relative efficiencies of photocurrent and photodoping in Fig. B.4 by considering the dependence of photocurrent and trion PL emission on two laser powers. An excitation spot is placed in the center of the device to generate photocurrent, with the same optical path used to collect PL. A second laser is focused on a gate edge to provide holes via dissociation doping. Varying the power of the two lasers demonstrates comparable process efficiencies. The discrepancy between photocurrent and PL at low excitation spot power is attributed to the fact that the doping laser is also able to partially excite photocurrent from the part of the optical spot that overlaps the gated

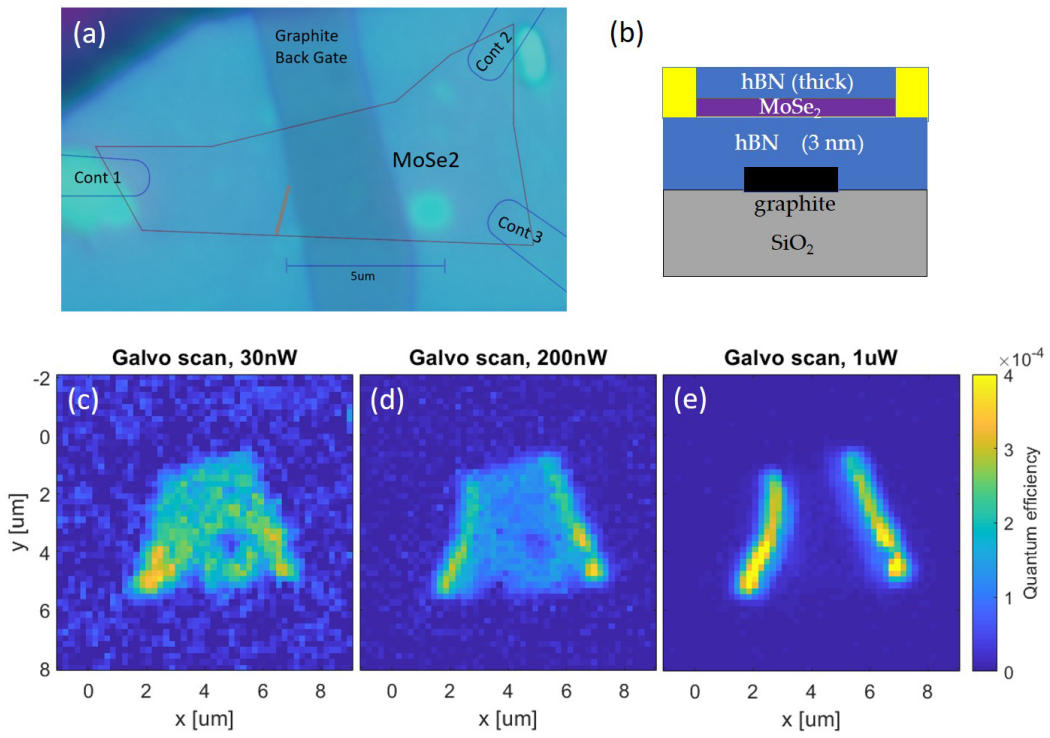


Figure B.3: Spatially resolved dissociation doping via photocurrent a) Annotated microscope image of an encapsulated $MoSe_2$ device with schematic in (**b**). **c,d,e**) Maps of photocurrent under scanning of optical excitation at varying power. Under increasing power, the inability of contacts to source holes restricts photocurrent generation to the edges of the gated region where lateral fields allow for doping via dissociation of excitons.

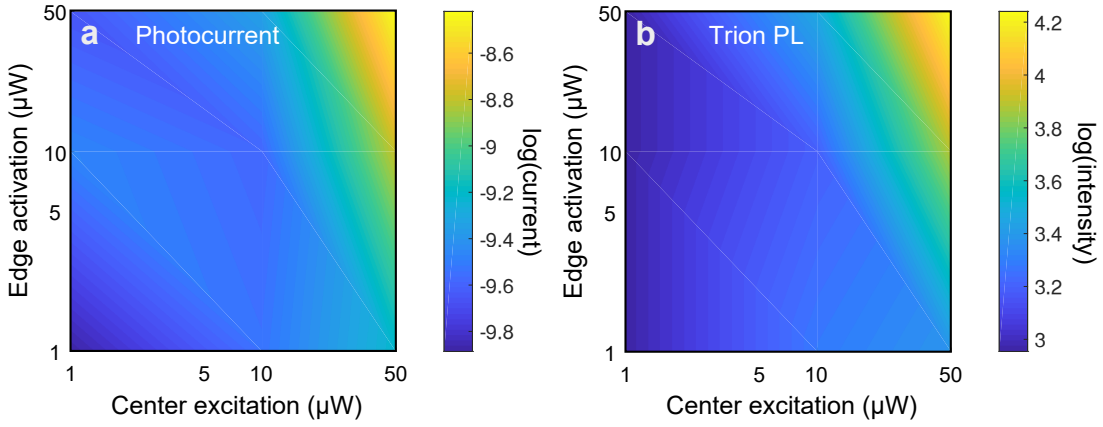


Figure B.4: Dependence on excitation and photodoping power a) Photocurrent and **b**) trion PL as a function of the optical power at a fixed excitation spot in the center of the device in Fig. B.3 and a fixed photodoping spot at a gate edge.

region, while the PL collection occurs only at the center.

Figure B.5 explores a similar effect to Fig. B.3 on a $MoSe_2$ device with 90 nm thick hBN and a thin metal bottom gate outlined in both panels. Scanning a single excitation spot over a local gate biased to -8 V produces edge-dominated photocurrent as in Fig. B.3e due to the need for photodoping. However, placing a considerably stronger fixed laser at the gate edge and scanning a weak excitation laser, gives rise to a uniform photocurrent increase when illuminating the gated region, indicating that an adequate supply of holes is being provided by the edge excitation. It is important to note that the QE numbers consider only the photocurrent difference produced by the scanning laser, after subtracting the substantially higher constant photocurrent due to the edge excitation laser's overlap with the gated area and resulting photocurrent generation.

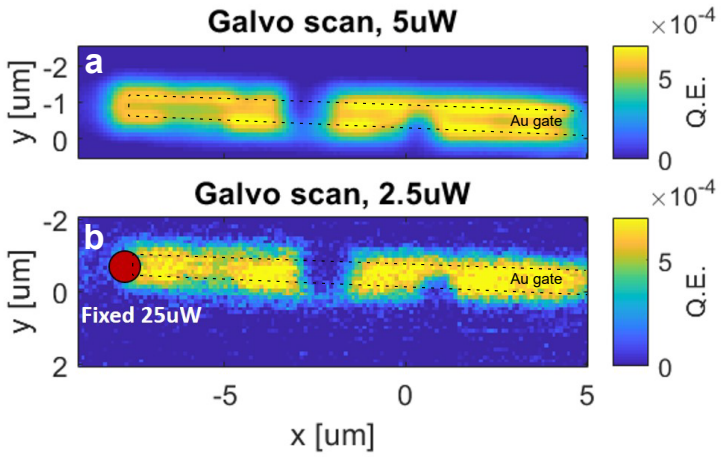


Figure B.5: Spatially resolved dissociation doping via photocurrent Spatial maps of photocurrent under scanned single point 5 μW 660 nm excitation (**a**) and, in (**b**), strong fixed edge excitation (25 μW 660 nm) accompanied by weak scanned excitation (2.5 μW 660 nm). Quantum efficiency figures are computed subtracting away the current due to fixed excitation.

B.6 Photocurrent spatial uniformity

By confocally scanning the excitation laser over a sample, we investigate the spatial uniformity of the photocurrent process. In Fig B.3, we provide a discussion demonstrating the current is spatially uniform over an electrode when sufficient hole-doping is provided to the $MoSe_2$ by dissociation. Similarly, Fig. B.3c shows increasingly uniform current at low excitation power when inefficient hole-doping mechanisms can maintain the doping of the material. In WSe_2, meanwhile, hole-doping can be achieved efficiently via the edge contacts allowing us to examine the spatial distribution in the simplest configuration, using a single scanned excitation laser of arbitrary intensity. The results

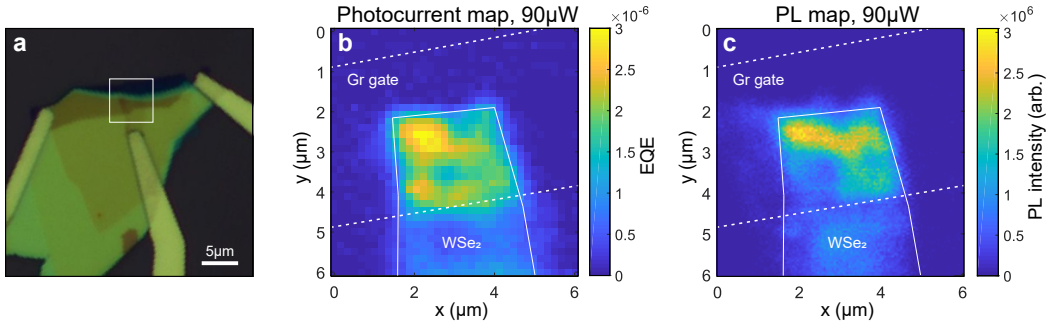


Figure B.6: WSe_2 photocurrent spatial mapping a) Optical image of a WSe_2 monolayer device separated from a graphite bottom gate by 12nm hBN. **b, c**) Photocurrent and PL maps over the device region indicated by the white square in (a), respectively. Photocurrent is present over the WSe_2 region located over the bottom gate, showing greater spatial uniformity than the PL data.

of this experiment are presented in Fig. B.6 for a WSe_2 monolayer separated by 12 nm hBN from a graphite bottom gate (device F). Comparing the map of photocurrent generation (Fig. B.6b), we see a higher degree of uniformity than the PL emission (Fig. B.6c), suggesting that the uniformity in this device is limited by material cleanliness rather than intrinsic properties of the process. Taken together, these varied experiments support the model of a photocurrent process that is intrinsic to the TMD-hBN system and not mediated by particular defects or electric field configuration.

B.7 Resonant excitation efficiency comparison

Due to the expected differences in off-resonant (660 nm) excitation efficiency we consider resonant excitation of both materials in Fig B.7. While the efficiency of WSe_2 is higher under resonant excitation, as might be expected, that difference accounts for only a

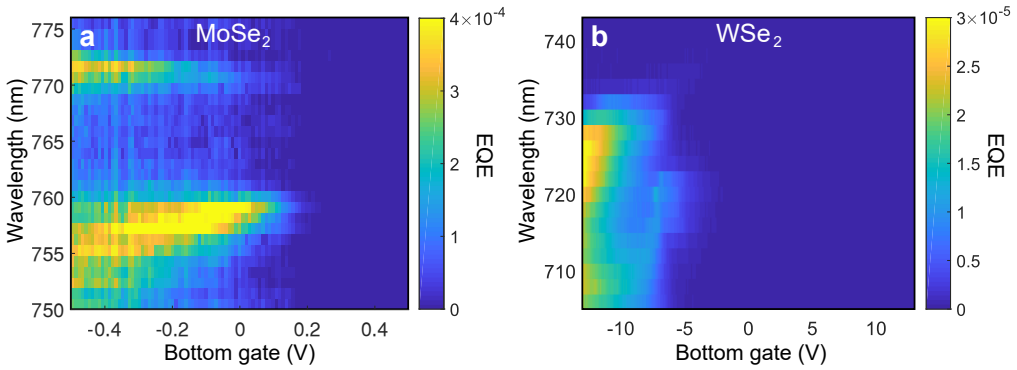


Figure B.7: Photocurrent efficiency under resonant excitation Photocurrent EQE as a function of excitation wavelength and local gate voltage for $MoSe_2$ (**a**) and WSe_2 (**b**) showing that overall efficiency is still substantially lower for WSe_2, as expected from the difference in band alignment relative to neutral exciton energy.

small part of the total disparity between the two materials. As laid out in the main text, we ascribe the remaining difference to the distinct valence band alignments between the TMD and hBN.

B.8 $MoSe_2$ contact verification

To evaluate the performance of edge contacts on an $MoSe_2$ device at the 6 K operating temperature, we consider experiments on device C, which was fabricated with contacts on both sides of a locally bottom-gated region, as shown in Fig. B.8a. To activate the contacts, we excite with a pair of confocal 50 µW 660nm lasers at the interface between the metal and TMD. The excitation occurs far enough from the gated region so as to not induce any significant photocurrent, but allows the contacts to source and

sink a substantial current relatively symmetrically. In Fig. B.8b, we plot the source-drain current between the two contacts while driving one in opposition to the other, for varying values of local gate bias in the center region of the device. These curves are consistent with electron current through the contacts, with a flat band condition at approximately 0.25 V bottom gate voltage. For positive gate bias, the curves are limited by the source-drain voltage difference while for negative bias it presents a barrier to source-drain current. Plotting the current as a 2-dimensional function of contact voltage and gate voltage shows a unity slope to the onset of current - a result that is consistent with n-type carriers. Finally, we observe that the optical excitation applied to the contacts only impacts the current for the contact that sources electrons and is not necessary on the contact that accepts electrons. This behaviour aligns well with photocurrent measurements in which exciton dissociation is able to hole dope part of the device by generating an electron-current into one of the contacts and a corresponding hole current into the gated region. Those accumulated holes can subsequently be photoexcited through the hBN, with the contact resistance not significantly rate limiting for the optical powers used in these studies. This conclusion is reinforced by the linear dependence of the photocurrent processes on optical power, indicating that increasing photocurrent does not substantially alter the electrostatic conditions in the experiments used to examine Auger process efficiency.

Resonant excitation can give further insight on the doping conditions in $MoSe_2$. Due to the shift of the exciton resonance with doping, photocurrent at fixed excitation wavelength

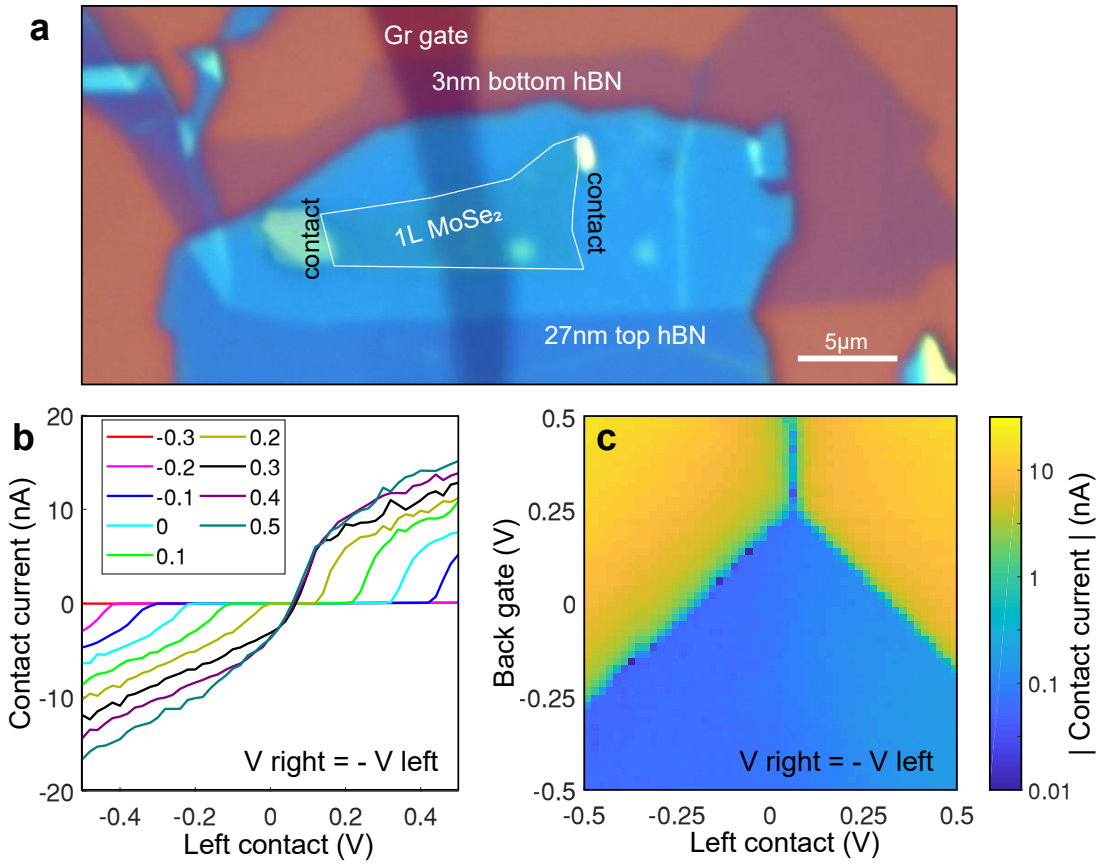


Figure B.8: $MoSe_2$ contact verification a) Optical image of device C ($MoSe_2$ monolayer, 3nm hBN) prior to contact fabrication, highlighting the device structure and location of subsequently fabricated edge contacts to the $MoSe_2$. **b, c**) Current at the left contact when driving the two contacts in opposition to each other while varying the voltage on the graphite bottom gate. Measurements are performed at 6 K. Optical excitation is applied at the contacts, far away from the gated region such that no significant photocurrent to the bottom gate is observed. The data are consistent with an electron current across a pair of junctions generated by the potential step at the gate edges, with flat-band conditions at approximately 0.25 V on the gate. We note the ability of these contacts to source significant electron-current, in excess of 5 nA at a source-drain bias of 0.1 V.

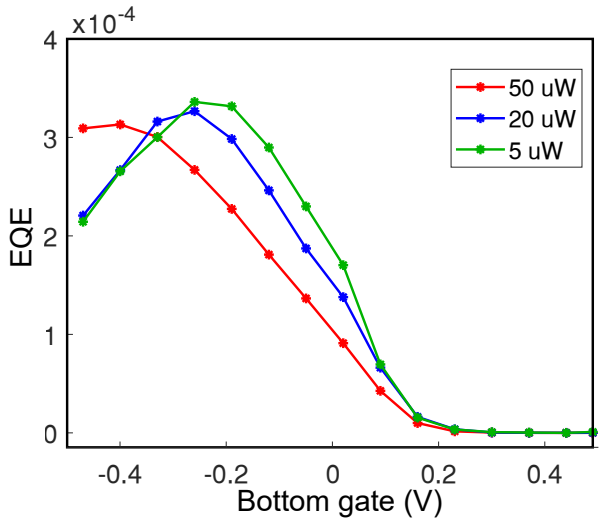


Figure B.9: Signatures of inadequate hole replenishment Data taken from a bottom gated $MoSe_2$ device (device C) with 50 μW 660 nm excitation at the gate edge for dissociation doping, and exciton-resonant 757 nm excitation of varying power over the gated region. Due to the shift in resonance with doping, the EQE peaks at a certain doping level. For increasing center excitation power, the photocurrent generation exceeds the rate of hole-doping via dissociation, resulting in lower hole-doping for a given local gate voltage. This manifests quite directly as a shift of the efficiency peak vs gate voltage, though the peak amplitude is not substantially affected as the optimal carrier density is still achieved.

can be seen to peak at a particular doping as shown in Fig. B.9. When photocurrent rate approaches the rate of dissociation doping a shift is observed corresponding to a change in doping conditions vs gate voltage due to inadequate hole replenishment rate. For $MoSe_2$ data discussed in the main text, care is taken to verify that no significant shift is observed with varying optical power such that the results are not confounded by inadequate hole replenishment.

C

Supporting Material for Chapter 3

C.1 Signal corrections and hBN background subtraction

When imaging thin materials on an SiO_2 substrate for a prolonged period of time, a noticeable degree of charging can be seen in the substrate, gradually altering the level of secondary emission. This charging is compensated for in our data by dividing out the yield from an uncovered region of substrate. For systems with natural contrast, such as AB/BA domains in graphene or twisted WSe_2, it is further helpful to normalize to the mean of the two regions so as to eliminate drift due to charging effects and reduce the impact of

angle-dependent yield variation due to channeling in the encapsulation layer or substrate. When collecting an azimuthal dependence for materials without domain contrast, such as AA' stacked natural WSe_2 bilayers, it is necessary to compensate for channeling effects in surrounding layers carefully. Fig. C.1 shows the azimuthal dependence for the bilayer part of the device discussed in Fig. 3.6, before and after compensating for channeling in the top encapsulation. Note that for thick hBN encapsulation, the modulation due to channeling in the hBN far exceeds that of the underlying TMD, making this process exceedingly challenging for increased hBN thickness.

C.2 Computation modelling of SEM signal

To compute primary electron transmission, atomic nuclei for the 2D material of interest are represented as points in 3D. Owing to the translational symmetry of the lattice, we consider incoming electrons across a hexagonal region corresponding to one lattice cell. A set of 10,000 to 250,000 coordinates within the hexagon is selected as entry points for the electron beams into the material, either at random with uniform probability or via a uniform grid. For each value of polar and azimuthal angle, a line through each point is considered, and the distance between the line and every lattice atom (i.e., the impact parameter, b is calculated. A transmission probability of the form $1 - \frac{A}{1+(\frac{b}{B})^2}$ is then taken, with the product over all lattice atoms giving the overall transmission probability for the line in question. Averaging over all lines then gives the overall transmission at

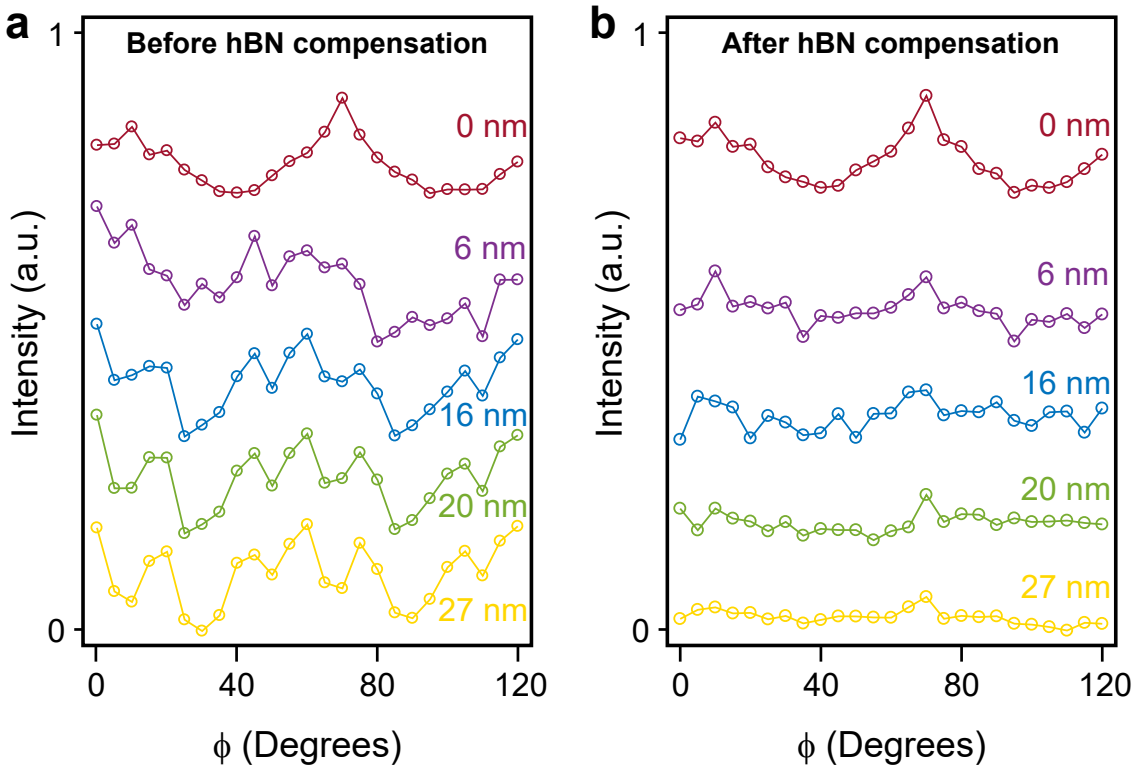


Figure C.1: Compensation for channeling effects through top hBN a-b) Azimuthal dependence of SEM signal from bi-layer TMD under hBN of varying thickness, before (**a**) and after (**b**) compensation for channeling effects in the hBN. We note that (**b**) is also shown in Fig. 3.6c in the main text.

the given θ and ϕ. Notably, though we only consider transmission across one lattice cell, the tails of the scattering probability mean that we must consider atoms outside of a one-cell-wide path. Typically, calculations were done considering atoms up to 4 inter-atomic distances away from the electron beam.

Transmission for the above figures was calculated using empirical values of $A = 0.1$ and $B = 0.18$Å. Computations for ABA/ABC graphene in Fig. 3.4 were performed for 5 layers stacked in ABCAB or ABABA orderings, using 100,000 lines within the lattice cell, with Monte Carlo coordinates. WSe_2 AB/BA computations were performed with 100,000 lines arranged on a grid, and verified with an equivalent model using 250,000 Monte Carlo generated lines. To represent the difference in atomic number in the WSe_2 lattice, an approximation is made whereby the tungsten atoms are modelled as two overlapping selenium atoms. Notably, the computed output that most closely resembles the data is at a polar angle of 43° rather than 40° at which the data was taken. This is most likely due to differences in interlayer spacing in AB/BA stacked TMD compared to the natural AA' stacking lattice constants used for the computation. The $MoSe_2$ computation in Fig. 3.12 is performed with a grid of 100,000 lines, at a polar angle of 27.5° and reproduces the periodicity but differs in some features. The difference could be attributed to the simplification of the multilayer to a model of only the top two layers, and also potential differences in secondary yield between molybdenum and selenium, along with effects of the 10nm gold encapsulation in attenuating secondary electron emission.

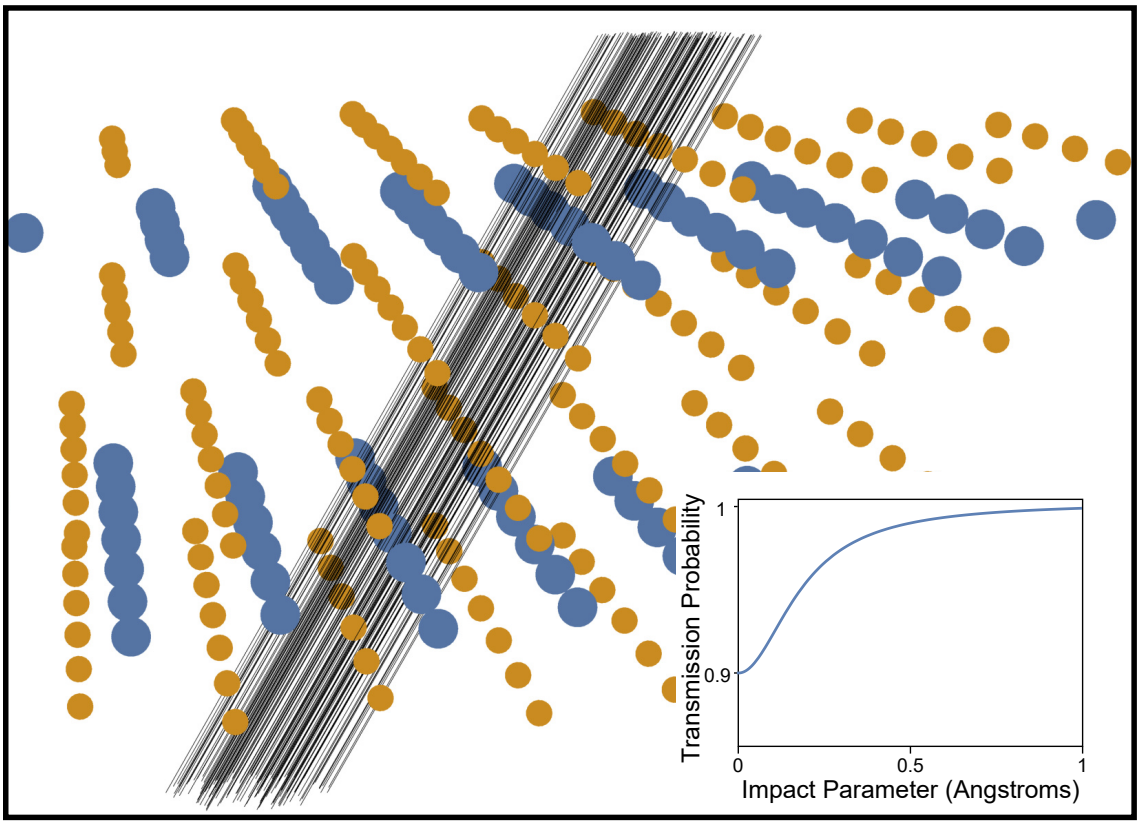


Figure C.2: Computational modelling of SEM imaging Schematic of computational method: Parallel primary beams (black lines) are positioned at Monte Carlo generated positions within an area corresponding to one unit cell, and their transmission probability through the lattice is calculated using a Lorentzian shaped scattering potential (inset) at each atom site.

C.3 Comparison of PL and absorption spectroscopy

We conduct gate-dependent absorption spectroscopy of another device D3, shown as the derivative of differential reflection in Figure C.3a (PL spectra are shown in Figure C.3b for comparison). While interlayer exciton absorption is too weak to be observed, we observe strong absorption features from the intralayer excitons[50,70]. This is consistent with our assignment of the intralayer excitons to the momentum direct K-K transition. The doping dependence observed in absorption measurements is also consistent with PL. While the type I exciton exhibits much stronger doping effects (blue-shift and weakening of neutral state) than the type II exciton at the onset of the p-doped regime, the type II exciton exhibits stronger doping effects at the onset of the n-doped regime. In the n-doped regime, the type I exciton also shows clear signs of doping, as expected from the fact that the electrons are more delocalized than the holes. The absorption spectra also show the red-shifted charged exciton states that were observed in PL.

C.4 Lateral exciton motion model

Assuming a thermalized ensemble of excitons, we estimate the distance that an exciton moves before recombining as $l = \sqrt{k_B T/M_X} \cdot \tau_X \sim 10 - 100$ nm, where k_B is the Boltzmann constant, $M_X \sim 0.8 m_e$[76] is the exciton translational mass, and T=4 K is the exciton temperature. Since the intralayer excitons are short-lived ($\tau_X \sim 1 - 10$ ps)[43,67], the lifetime is expected to be comparable to the mean free scattering time, τ_{mfp}. Their

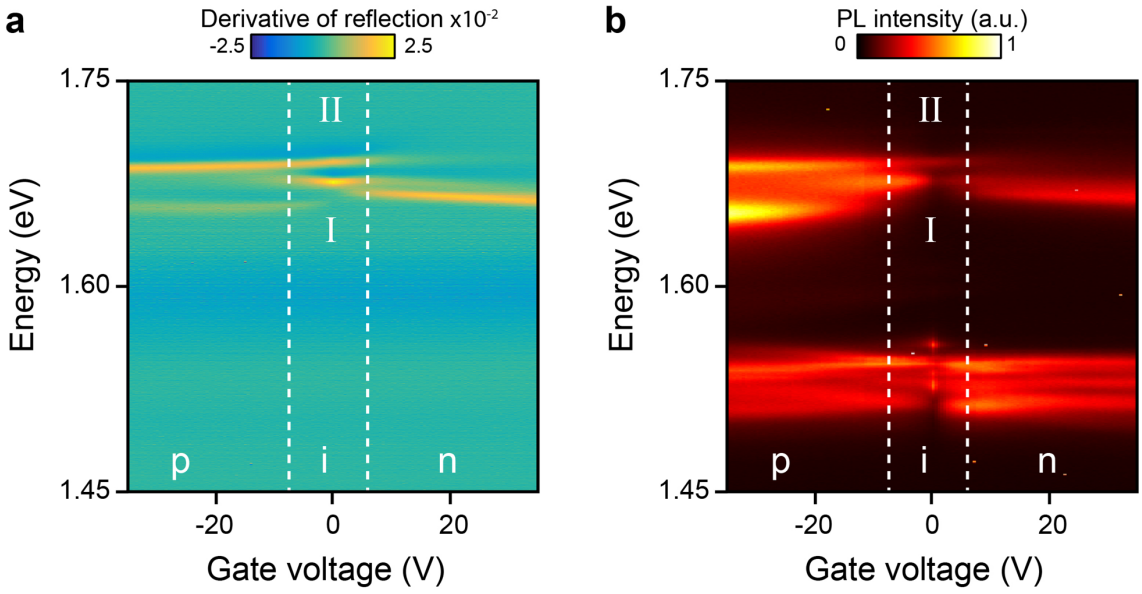


Figure C.3: Comparison of absorption and photoluminescence spectra. a) Derivative of differential reflectance vs. gate voltage in device D3, showing strong intralayer exciton absorption, consistent with the momentum direct K-K transition. **b**) Corresponding gate-dependent photoluminescence spectra from device D3.

motion should therefore be between the diffusive ($l \propto \sqrt{\tau_X \tau_{\mathrm{mfp}}}$) and ballistic ($l \propto \tau_X$) regimes, and the two pictures give similar estimates ($\sqrt{(\tau_X \tau_{\mathrm{mfp}}} \sim \tau_X$). We also note that the exciton temperature can be slightly elevated due to laser heating. Nevertheless, since we use a low-power continuous wave laser and have not observed any heating-induced exciton peak shifts, we expect that the exciton temperature remains below 10 K, thus not impacting the conclusions in the main text.

C.5 Experimental Methods

C.5.1 Device fabrication

Flakes of hBN, graphene and WSe_2 were first mechanically exfoliated from bulk crystals onto clean Si/SiO_2 wafers (Si substrates with 285 nm thermally grown SiO_2). Few-layer graphene and monolayer WSe_2 were identified optically, while the thickness of hBN flakes was determined with atomic force microscopy. Next, the heterostructures were assembled with the dry-transfer method, using the tear-and-stack technique[40] to form twisted bilayer WSe_2. Electrical contacts to both the WSe_2 and the graphite gates were defined with e-beam lithography and deposited through thermal evaporation (10 nm Cr + 90 nm Au).

C.5.2 Measurements

Photoluminescence measurements were conducted in a 4 K cryostat (Montana Instruments), using a custom-built 4f confocal setup with a 0.75 NA objective and a 660 nm Thorlabs diode laser. Two galvo mirrors were used to control the excitation and collection positions on the sample, and electrostatic gating was performed with Keithley multimeters. The DOLP was measured with polarizers in the excitation and collection paths. To eliminate any polarization-dependent system response, all DOLP measurements included excitation with (and collection of) both vertically and horizontally polarized light. The DOLP was then calculated from:

$$\mathrm{DOLP} = \frac{r-1}{r+1}, r = \frac{\sqrt{I_{\mathrm{hh}} \cdot I_{\mathrm{vv}}}}{\sqrt{I_{\mathrm{vh}} \cdot I_{\mathrm{hv}}}}$$

where the subscripts indicate the polarization of the excitation and collection, respectively (h: horizontal, v: vertical). SEM imaging of the reconstructed moiré pattern was done with a Zeiss Field Emission Scanning Electron Microscope Ultra Plus at 30 µm aperture, with a 300 V bias on the E-T detector.

References

[1] Alexeev, E. M., Ruiz-Tijerina, D. A., et al. (2019). Resonantly hybridized excitons in moiré superlattices in van der Waals heterostructures. *Nature*, 567, 81–86.

[2] Ashida, K., Kajino, T., et al. (2015). Crystallographic orientation dependence of SEM contrast revealed by SiC polytypes. *Journal of Vacuum Science and Technology B*, 33, 04E104.

[3] Bekenstein, R., Pikovski, I., Pichler, H., Shahmoon, E., Yelin, S. F., & Lukin, M. D. (2020). Quantum metasurfaces with atom arrays. *Nature Physics*, 16(6), 676–681.

[4] Björk, G., Pau, S., Jacobson, J., & Yamamoto, Y. (1994). Wannier exciton superradiance in a quantum-well microcavity. *Phys. Rev. B*, 50, 17336–17348.

[5] Blumoff, J. Z., Pan, A. S., Keating, T. E., Andrews, R. W., Barnes, D. W., Brecht, T. L., Croke, E. T., Euliss, L. E., Fast, J. A., Jackson, C. A., et al. (2022). Fast and high-fidelity state preparation and measurement in triple-quantum-dot spin qubits. *PRX Quantum*, 3(1), 010352.

[6] Brem, S., Lin, K.-Q., Gillen, R., Bauer, J. M., Maultzsch, J., Lupton, J. M., & Malic, E. (2020). Hybridized intervalley moiré excitons and flat bands in twisted wse 2 bilayers. *Nanoscale*, 12(20), 11088–11094.

[7] Cadiz, F., Robert, C., Courtade, E., Manca, M., Martinelli, L., Taniguchi, T., Watanabe, K., Amand, T., Rowe, A., Paget, D., et al. (2018). Exciton diffusion in wse2 monolayers embedded in a van der waals heterostructure. *Applied Physics Letters*, 112(15), 152106.

[8] Cao, Y., Fatemi, V., et al. (2018a). Correlated insulator behaviour at half-filling in magic-angle graphene superlattices. *Nature*, 556, 80–84.

[9] Cao, Y., Fatemi, V., et al. (2018b). Unconventional superconductivity in magic-angle graphene superlattices. *Nature*, 556, 43–50.

[10] Cappelluti, E., Roldán, R., Silva-Guillén, J., Ordejón, P., & Guinea, F. (2013). Tight-binding model and direct-gap/indirect-gap transition in single-layer and multilayer mos 2. *Physical Review B*, 88(7), 075409.

[11] Carr, S., Massatt, D., Torrisi, S. B., Cazeaux, P., Luskin, M., & Kaxiras, E. (2018). Relaxation and domain formation in incommensurate two-dimensional heterostructures. *Physical Review B*, 98(22), 224102.

[12] Cassabois, G., Valvin, P., & Gil, B. (2016). Hexagonal boron nitride is an indirect bandgap semiconductor. *Nature Photonics*, 10(4), 262–266.

[13] Cazaux, J. (2005). Recent developments and new strategies in scanning electron microscopy. *Journal of microscopy*, 217(1), 16–35.

[14] Chen, G., Jiang, L., Wu, S., et al. (2019a). Evidence of a gate-tunable Mott insulator in a trilayer graphene moiré superlattice. *Nature Physics*, 15, 237–241.

[15] Chen, G., Sharpe, A. L., Gallagher, P., et al. (2019b). Signatures of tunable superconductivity in a trilayer graphene moiré superlattice. *Nature*, 572, 215–219.

[16] Chernikov, A., Berkelbach, T. C., Hill, H. M., Rigosi, A., Li, Y., Aslan, O. B., Reichman, D. R., Hybertsen, M. S., & Heinz, T. F. (2014). Exciton binding energy and nonhydrogenic rydberg series in monolayer ws_2. *Physical Review Letters*, 113, 076802.

[17] Chow, C. M. E., Yu, H., Schaibley, J. R., Rivera, P., Finney, J., Yan, J., Mandrus, D., Taniguchi, T., Watanabe, K., Yao, W., et al. (2020). Monolayer semiconductor auger detector. *Nano Letters*.

[18] Coates, D. (1967). Kikuchi-like reflection patterns obtained with the scanning electron microscope. *The Philosophical Magazine: A Journal of Theoretical Experimental and Applied Physics*, 16(144), 1179–1184.

[19] Collett, B. M. (1970). Scanning electron microscopy: A review and report of research in wood science. *Wood and Fiber Science*, (pp. 113–133).

[20] Courtade, E., Semina, M., Manca, M., Glazov, M., Robert, C., Cadiz, F., Wang, G., Taniguchi, T., Watanabe, K., Pierre, M., et al. (2017). Charged excitons in monolayer wse 2: experiment and theory. *Physical Review B*, 96(8), 085302.

[21] Dean, C. R., Young, A. F., Meric, I., Lee, C., Wang, L., Sorgenfrei, S., Watanabe, K., Taniguchi, T., Kim, P., Shepard, K. L., & Hone, J. (2010). Boron nitride

substrates for high-quality graphene electronics. *Nature Nanotechnology*, 5, 772–776.

[22] Delteil, A., Sun, Z., Gao, W.-b., Togan, E., Faelt, S., & Imamoğlu, A. (2016). Generation of heralded entanglement between distant hole spins. *Nature Physics*, 12(3), 218–223.

[23] Dibos, A. M., Zhou, Y., Jauregui, L. A., Scuri, G., Wild, D. S., High, A. A., Taniguchi, T., Watanabe, K., Lukin, M. D., Kim, P., et al. (2019). Electrically tunable exciton–plasmon coupling in a wse2 monolayer embedded in a plasmonic crystal cavity. *Nano letters*, 19(6), 3543–3547.

[24] Everhart, T. E. & Thornley, R. (1960). Wide-band detector for micro-microampere low-energy electron currents. *Journal of scientific instruments*, 37(7), 246.

[25] Gabor, N. M., Song, J. C. W., Ma, Q., Nair, N. L., Taychatanapat, T., Watanabe, K., Taniguchi, T., Levitov, L., & P., J.-H. (2011). Hot carrier–assisted intrinsic photoresponse in graphene. 334, 648–652.

[26] Geim, A. K. & Grigorieva, I. V. (2013). Van der waals heterostructures. *Nature*, 499, 419–425.

[27] Grimme, S., Antony, J., Ehrlich, S., & Krieg, H. (2010). A consistent and accurate ab initio parametrization of density functional dispersion correction (dft-d) for the 94 elements h-pu. *The Journal of chemical physics*, 132(15), 154104.

[28] Han, B., Robert, C., Courtade, E., Manca, M., Shree, S., Amand, T., Renucci, P., Taniguchi, T., Watanabe, K., Marie, X., et al. (2018). Exciton states in monolayer mose 2 and mote 2 probed by upconversion spectroscopy. *Physical Review X*, 8(3), 031073.

[29] Hao, K., Moody, G., Wu, F., Dass, C. K., Xu, L., Chen, C.-H., Sun, L., Li, M.-Y., Li, L.-J., MacDonald, A. H., et al. (2016). Direct measurement of exciton valley coherence in monolayer wse2. *Nature Physics*, 12(7), 677–682.

[30] Hao, K., Xu, L., Wu, F., Nagler, P., Tran, K., Ma, X., Schüller, C., Korn, T., MacDonald, A. H., Moody, G., et al. (2017). Trion valley coherence in monolayer semiconductors. *2D Materials*, 4(2), 025105.

[31] Heyd, J., Scuseria, G. E., & Ernzerhof, M. (2003). Hybrid functionals based on a screened coulomb potential. *The Journal of chemical physics*, 118(18), 8207–8215.

[32] Jiang, Y., Chen, Z., et al. (2019). Electron ptychography of 2D materials to deep sub-Ångstrom resolution. *Nature*, 559, 343–349.

[33] Jin, C., Regan, E. C., Yan, A., Iqbal Bakti Utama, M., Wang, D., Zhao, S., Qin, Y., Yang, S., Zheng, Z., Shi, S., et al. (2019). Observation of moiré excitons in wse2/ws2 heterostructure superlattices. *Nature*, 567(7746), 76–80.

[34] Jones, A. M., Yu, H., Ross, J. S., Klement, P., Ghimire, N. J., Yan, J., Mandrus, D. G., Yao, W., & Xu, X. (2014). Spin–layer locking effects in optical orientation of exciton spin in bilayer wse2. *Nature Physics*, 10(2), 130–134.

[35] Joy, D., Prasad, M., & Meyer III, H. (2004). Experimental secondary electron spectra under SEM conditions. *Journal of microscopy*, 215(1), 77–85.

[36] Joy, D. C., Newbury, D. E., & Davidson, D. L. (1982). Electron channeling patterns in the scanning electron microscope. *Journal of Applied Physics*, 53(8), R81–R122.

[37] Joy, D. C. & Pawley, J. B. (1992). High-resolution scanning electron microscopy. *Ultramicroscopy*, 47(1-3), 80–100.

[38] Ju, L., Shi, Z., Nair, N., et al. (2015). Topological valley transport at bilayer graphene domain walls. 520, 650–655.

[39] Kerelsky, A., Rubio-Verdú, C., Xian, L., Kennes, D. M., Halbertal, D., Finney, N., Song, L., Turkel, S., Wang, L., Watanabe, K., et al. (2019). Moiré-less correlations in abca graphene. *arXiv preprint arXiv:1911.00007*.

[40] Kim, K., Yankowitz, M., Fallahazad, B., Kang, S., Movva, H. C., Huang, S., Larentis, S., Corbet, C. M., Taniguchi, T., Watanabe, K., et al. (2016). van der waals heterostructures with high accuracy rotational alignment. *Nano letters*, 16(3), 1989–1995.

[41] Kormányos, A., Zólyomi, V., Fal'ko, V. I., & Burkard, G. (2018). Tunable berry curvature and valley and spin hall effect in bilayer mos 2. *Physical Review B*, 98(3), 035408.

[42] Kresse, G. & Furthmüller, J. (1996). Efficient iterative schemes for ab initio total-energy calculations using a plane-wave basis set. *Physical review B*, 54(16), 11169.

[43] Kulig, M., Zipfel, J., Nagler, P., Blanter, S., Schüller, C., Korn, T., Paradiso, N., Glazov, M. M., & Chernikov, A. (2018). Exciton diffusion and halo effects in monolayer semiconductors. *Physical review letters*, 120(20), 207401.

[44] Kunstmann, J., Mooshammer, F., Nagler, P., Chaves, A., Stein, F., Paradiso, N., Plechinger, G., Strunk, C., Schüller, C., Seifert, G., et al. (2018). Momentum-space indirect interlayer excitons in transition-metal dichalcogenide van der waals heterostructures. *Nature Physics*, 14(8), 801–805.

[45] Lau, K. W., Gong, Z., Yu, H., Yao, W., et al. (2018). Interface excitons at lateral heterojunctions in monolayer semiconductors. *Physical Review B*, 98(11), 115427.

[46] Linardy, E., Yadav, D., Vella, D., Verzhbitskiy, I. A., Watanabe, K., Taniguchi, T., Pauly, F., Trushin, M., & Eda, G. (2020). Harnessing exciton–exciton annihilation in two-dimensional semiconductors. *Nano letters*, 20(3), 1647–1653.

[47] Liu, G.-B., Xiao, D., Yao, Y., Xu, X., & Yao, W. (2015). Electronic structures and theoretical modelling of two-dimensional group-vib transition metal dichalcogenides. *Chemical Society Reviews*, 44(9), 2643–2663.

[48] Liu, K., Zhang, L., Cao, T., Jin, C., Qiu, D., Zhou, Q., Zettl, A., Yang, P., Louie, S. G., & Wang, F. (2014). Evolution of interlayer coupling in twisted molybdenum disulfide bilayers. *Nature communications*, 5(1), 1–6.

[49] Ma, Q., Andersen, T. I., Nair, N., Gabor, N. M., Massicotte, M., Lui, C. H., Young, A. F., Fang, W., Watanabe, K., Taniguchi, T., Kong, J., Gedik, N., Koppens, F. H. L., & Jarillo-Herrero, P. (2016). Tuning ultrafast electron thermalization pathways in a van der waals heterostructure. *Nature Physics*, 12, 455–459.

[50] Mak, K. F., He, K., Lee, C., Lee, G. H., Hone, J., Heinz, T. F., & Shan, J. (2013). Tightly bound trions in monolayer mos2. *Nature materials*, 12(3), 207–211.

[51] Mak, K. F. & Shan, J. (2016). Photonics and optoelectronics of 2d semiconductor transition metal dichalcogenides. *Nature Photonics*, 10, 216–226.

[52] Mak, K.-F., Shan, J., & Heinz, T. F. (2010). Electronic Structure of Few-Layer Graphene: Experimental Demonstration of Strong Dependence on Stacking Sequence. *Physical Review Letters*, 104, 176404.

[53] Mandyam, S. V., Zhao, M.-Q., Masih Das, P., Zhang, Q., Price, C. C., Gao, Z., Shenoy, V. B., Drndic, M., & Johnson, A. T. C. (2019). Controlled growth of large-area bilayer tungsten diselenides with lateral p–n junctions. *ACS nano*, 13(9), 10490–10498.

[54] Manzeli, S., Ovchinnikov, D., Pasquier, D., Yaziev, O. V., & Kis, A. (2017). 2d transition metal dichalcogenides. *Nature Reviews Materials*, 2, 17033.

[55] Martin, I., Blanter, Y., & Morpurgo, A. (2008). Topological confinement in bilayer graphene. *Physical Review Letters*, 100, 036804.

[56] Massicotte, M., Vialla, F., Schmidt, P., Lundeberg, M. B., Latini, S., Haastrup, S., Danovich, M., Davydovskaya, D., Watanabe, K., Taniguchi, T., Fal'ko, V. I., Thygesen, K. S., Pedersen, T. G., & Koppens, F. H. L. (2018). Dissociation of two-dimensional excitons in monolayer wse_2. *Nature Communications*, 9, 1633.

[57] Morin, P., Pitaval, M., et al. (1979). Electron channelling imaging in scanning electron microscopy. *Philosophical Magazine A*, 40, 511–524.

[58] Nguyen, P. V., Teutsch, N. C., Wilson, N. P., Kahn, J., Xia, X., Graham, A. J., Kandyba, V., Giampietri, A., Barinov, A., Constantinescu, G. C., et al. (2019). Visualizing electrostatic gating effects in two-dimensional heterostructures. *Nature*, 572(7768), 220–223.

[59] Nguyen, T. A., Lee, J.-U., Yoon, D., & Cheong, H. (2014). Excitation energy dependent raman signatures of aba-and abc-stacked few-layer graphene. *Scientific reports*, 4, 4630.

[60] Novoselov, K. S., Geim, A. K., Morozov, S. V., Jiang, D.-e., Zhang, Y., Dubonos, S. V., Grigorieva, I. V., & Firsov, A. A. (2004). Electric field effect in atomically thin carbon films. *science*, 306(5696), 666–669.

[61] Novoselov, K. S., Mishchenko, A., Carvalho, A., & Castro Neto, A. H. (2016). 2D materials and van der Waals heterostructures. 353, aac9439–1–11.

[62] Palacios-Berraquero, C., Kara, D. M., Montblanch, A. R.-P., Barbone, M., Latawiec, P., Yoon, D., Ott, A. K., Loncar, M., Ferrari, A. C., & Atatüre, M. (2017). Large-scale quantum-emitter arrays in atomically thin semiconductors. *Nature communications*, 8(1), 1–6.

[63] Park, J. M., Cao, Y., Watanabe, K., Taniguchi, T., & Jarillo-Herrero, P. (2021). Tunable strongly coupled superconductivity in magic-angle twisted trilayer graphene. *Nature*, 590(7845), 249–255.

[64] Perczel, J., Borregaard, J., Chang, D. E., Pichler, H., Yelin, S. F., Zoller, P., & Lukin, M. D. (2017). Topological quantum optics in two-dimensional atomic arrays. *Physical review letters*, 119(2), 023603.

[65] Pisoni, R., Davatz, T., Watanabe, K., Taniguchi, T., Ihn, T., & Ensslin, K. (2019). Absence of interlayer tunnel coupling of k-valley electrons in bilayer mos 2. *Physical Review Letters*, 123(11), 117702.

[66] Regan, E., Wang, D., Jin, C., et al. (2019). Optical detection of Mott and generalized Wigner crystal states in WSe_2/WS_2 moiré superlattices. *arXiv*, (pp. 1910.09047).

[67] Robert, C., Lagarde, D., Cadiz, F., Wang, G., Lassagne, B., Amand, T., Balocchi, A., Renucci, P., Tongay, S., Urbaszek, B., et al. (2016). Exciton radiative lifetime in transition metal dichalcogenide monolayers. *Physical review B*, 93(20), 205423.

[68] Schwartz, A. J., Kumar, M., Adams, B. L., & Field, D. P. (2009). *Electron backscatter diffraction in materials science*, volume 2. Springer.

[69] Scuri, G., Andersen, T. I., Zhou, Y., Wild, D. S., Sung, J., Gelly, R. J., Bérubé, D., Heo, H., Shao, L., Joe, A. Y., et al. (2020). Electrically tunable valley dynamics in twisted wse 2/wse 2 bilayers. *Physical Review Letters*, 124(21), 217403.

[70] Scuri, G., Zhou, Y., High, A. A., Wild, D. S., Shu, C., De Greve, K., Jauregui, L. A., Taniguchi, T., Watanabe, K., Kim, P., et al. (2018). Large excitonic reflectivity of monolayer mose 2 encapsulated in hexagonal boron nitride. *Physical review letters*, 120(3), 037402.

[71] Seiler, H. (1983). Secondary electron emission in the scanning electron microscope. *Journal of Applied Physics*, 54(11), R1–R18.

[72] Seyler, K. L., Rivera, P., et al. (2019). Signatures of moiré-trapped valley excitons in $MoSe_2/WSe_2$ heterobilayers. *Nature*, 567, 66–70.

[73] Sharpe, A. L., Fox, E. J., Barnard, A. W., et al. (2019). Emergent ferromagnetism near three-quarters filling in twisted bilayer graphene. *Science*, 365, 605–608.

[74] Shree, S., Semina, M., Robert, C., Han, B., Amand, T., Balocchi, A., Manca, M., Courtade, E., Marie, X., Taniguchi, T., et al. (2018). Observation of exciton-phonon coupling in mose 2 monolayers. *Physical Review B*, 98(3), 035302.

[75] Sidler, M., Back, P., Cotlet, O., Srivastava, A., Fink, T., Kroner, M., Demler, E., & Imamoglu, A. (2016). Fermi polaron-polaritons in charge-tunable atomically thin semiconductors. *Nature Physics*, 13, 255–261.

[76] Stier, A. V., Wilson, N. P., Velizhanin, K. A., Kono, J., Xu, X., & Crooker, S. A. (2018). Magnetooptics of exciton rydberg states in a monolayer semiconductor. *Physical review letters*, 120(5), 057405.

[77] Sunku, S. S., Ni, G. X., et al. (2012). Photonic crystals for nano-light in moiré graphene superlattices. 362, 1153–1156.

[78] Takeda, K., Noiri, A., Nakajima, T., Kobayashi, T., & Tarucha, S. (2022). Quantum error correction with silicon spin qubits. *Nature*, 608, 682–686.

[79] Tang, Y., Li, L., Li, T., et al. (2019). WSe_2/WS_2 moiré superlattices: a new Hubbard model simulator. *arXiv*, (pp. 1910.08673).

[80] Tarnapolsky, G., Kruchkov, A. J., & Vishwanath, A. (2019). Origin of magic angles in twisted bilayer graphene. *Physical Review Letters*, 122, 106405.

[81] Tielrooij, K. J., Song, J. C. W., Jensen, S. A., Centeno, A., A., P., Zurutuza Elorza, A., Bonn, M., Levitov, L. S., & Koppens, F. H. L. (2013). Photoexcitation cascade and multiple hot-carrier generation in graphene. *Nature Physics*, 9, 248–252.

[82] Tran, K., Moody, G., Wu, F., Lu, X., Choi, J., Kim, K., Rai, A., Sanchez, D. A., Quan, J., Singh, A., et al. (2019). Evidence for moiré excitons in van der waals heterostructures. *Nature*, 567(7746), 71–75.

[83] Vaezi, A., Liang, Y., et al. (2013). Topological edge states at a tilt boundary in gated multilayer graphene. *Physical Review X*, 3, 021018.

[84] Van Der Zande, A. M., Kunstmann, J., Chernikov, A., Chenet, D. A., You, Y., Zhang, X., Huang, P. Y., Berkelbach, T. C., Wang, L., Zhang, F., et al. (2014). Tailoring the electronic structure in bilayer molybdenum disulfide via interlayer twist. *Nano letters*, 14(7), 3869–3875.

[85] Wang, Y., Wang, Z., Yao, W., Liu, G.-B., & Yu, H. (2017). Interlayer coupling in commensurate and incommensurate bilayer structures of transition-metal dichalcogenides. *Physical Review B*, 95(11), 115429.

[86] Weston, A., Zou, Y., Enaldiev, V., Summerfield, A., Clark, N., Zólyomi, V., Graham, A., Yelgel, C., Magorrian, S., Zhou, M., et al. (2020). Atomic reconstruction in twisted bilayers of transition metal dichalcogenides. *Nature Nanotechnology*, 15(7), 592–597.

[87] Wickramaratne, D., Weston, L., & Van de Walle, C. G. (2018). Monolayer to bulk properties of hexagonal boron nitride. *The Journal of Physical Chemistry C*, 122(44), 25524–25529.

[88] Woods, C., Britnell, L., Eckmann, A., Ma, R., Lu, J., Guo, H., Lin, X., Yu, G., Cao, Y., Gorbachev, R., et al. (2014). Commensurate–incommensurate transition in graphene on hexagonal boron nitride. *Nature physics*, 10(6), 451.

[89] Wu, F., Lovorn, T., & MacDonald, A. H. (2017). Topological exciton bands in moiré heterojunctions. *Physical review letters*, 118(14), 147401.

[90] Wu, F., Lovorn, T., Tutuc, E., Martin, I., & MacDonald, A. (2019). Topological insulators in twisted transition metal dichalcogenide homobilayers. *Physical review letters*, 122(8), 086402.

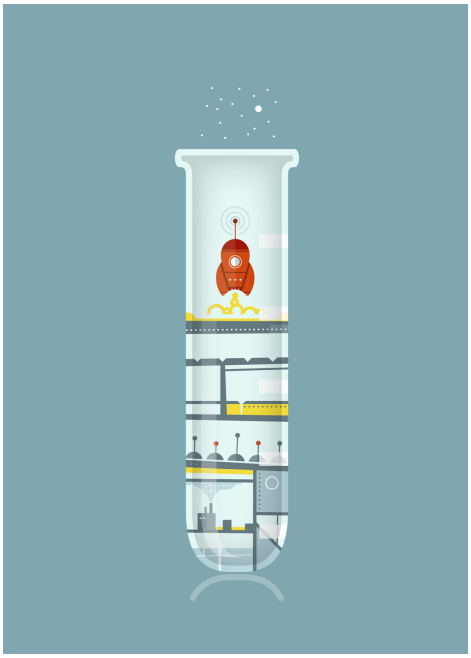
[91] Yankowitz, M., Ma, Q., Jarillo-Herrero, P., & LeRoy, B. J. (2019). van der waals heterostructures combining graphene and hexagonal boron nitride. *Nature Reviews Physics*, 1, 112–125.

[92] Yin, L.-J., Jiang, H., Qiao, J.-B., & He, L. (2016). Direct imaging of topological edge states at a bilayer graphene domain wall. *Nature Communications*, 7, 11760.

[93] Yoo, H., Engelke, R., Carr, S., Fang, S., Zhang, K., Cazeaux, P., Sung, S. H., Hovden, R., Tsen, A. W., Taniguchi, T., et al. (2019). Atomic and electronic

reconstruction at the van der waals interface in twisted bilayer graphene. *Nature materials*, 18(5), 448–453.

[94] Yu, H., Liu, G.-B., Tang, J., Xu, X., & Yao, W. (2017). Moiré excitons: From programmable quantum emitter arrays to spin-orbit–coupled artificial lattices. *Science advances*, 3(11), e1701696.



This thesis was typeset using LaTeX, originally developed by Leslie Lamport and based on Donald Knuth's TeX. The body text is set in 11 point Egenolff-Berner Garamond, a revival of Claude Garamont's humanist typeface. The above illustration, *Science Experiment 02*, was created by Ben Schlitter and released under CC BY-NC-ND 3.0. A template that can be used to format a PhD dissertation with this look & feel has been released under the permissive AGPL license, and can be found online at github.com/suchow/Dissertate or from its lead author, Jordan Suchow, at suchow@post.harvard.edu.